DEM Analysis of a Conveyor Transfer Chute

by

Jeandré Rossow

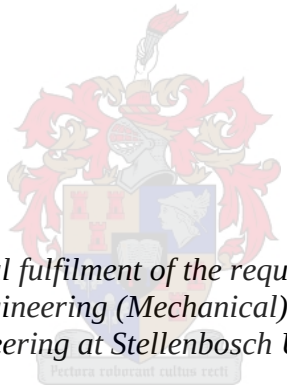

Thesis presented in partial fulfilment of the requirements for the degree of Master of Engineering (Mechanical) in the Faculty of Engineering at Stellenbosch University

Supervisor: Prof. C.J. Coetzee

December 2020

Declaration

By submitting this thesis electronically, I declare that the entirety of the work contained therein is my own, original work, that I am the sole author thereof (save to the extent explicitly otherwise stated), that reproduction and publication thereof by Stellenbosch University will not infringe any third party rights and that I have not previously in its entirety or in part submitted it for obtaining any qualification.

Date: 23 November 2020

Abstract

In the past, conveyor systems were designed and built based on trial-and-error, scale model prototyping, or using fundamental engineering mechanics analyses. However, these approaches can be inaccurate, time-consuming and costly. The analytical models used for the prediction of the flow behaviour of materials has become a widely accepted design tool. However, there are some variables which these models ignore, limiting the accuracy and application of this approach. The discrete element method (DEM), introduced by Peter A. Cundall in 1971, has developed into a popular design tool for the improvement of bulk material handling equipment and processes. DEM can model the complex interaction between discrete particles and particles-and-walls (structures) and designers can use it to quantify the performance of their designs. However, the main concern when using DEM, is the calibration and validation of the material properties. Inaccurate calibration of DEM models can lead to inaccurate results and consequently in inadequate designs.

The purpose of this study was to investigate the capability of, and accuracy with which DEM (PFC3D) can predict the bulk material flow of a cohesionless granular material through conveyor transfer points. The test material used was corn grains, having various non-spherical shapes and sizes. The material properties of the corn grains were determined by implementing several tests. The particle shape was modelled as spheres and clumps (multi-sphere particles) and further calibration tests were performed to obtain an accurate calibrated set of parameter values.

The inclined conveyor belts used in the experimental tests had a chevron pattern to provide more control over the mass flow rate, especially at higher belt speeds. The chevron pattern caused less material to roll back to the feeding zone and its inclusion in the DEM model was first investigated and validated. The different components of a transfer point that were investigated included an impact plate, hood, rock box and a chute. The predicted material flow characteristics (impact forces, velocities and flow patterns) were verified by comparing the results to particle image velocimetry (PIV) analysis of high-speed videos. Simulation strategies such as particle scaling, simplification of the shape model and decreasing the contact stiffness were also investigated to decrease computation time.

DEM accurately predicted the impact force ($|\text{error}| \leq 8.57$ %), velocity ($|\text{error}| \leq 5.31$ %), outflow velocity ($|\text{error}| \leq 19.90$ %) and other investigated flow patterns on a vertical impact plate, as well as the flow patterns in and from a rock box, through a hood and the mass flow rate causing blockage ($|\text{error}| \leq 5.00$ %). The maximum particle scale factor to accurately predict the flow against an impact plate was 7.0, while the particles could only be scaled by a factor 1.6 for the rock

box and chute build-up analyses. The analytical model, however, provided less accurate results in predicting the impact force (|error| ≤ 14.17 %), velocity (|error| ≤ 6.14 %) and outflow velocity (|error| ≤ 19.38 %) on a vertical impact plate. It is therefore concluded that DEM accurately predicted the material flow through a conveyor transfer system and can be used with confidence in industrial applications if an appropriate set of calibrated parameters is used.

Uittreksel

In die verlede is vervoerbandstelsels ontwerp en gebou op grond van proef-en-fout, prototipering van geskaalde modelle, of met behulp van fundamentele ingenieursmeganika ontledings. Hierdie benaderings is egter onakkuraat, tydrowend en duur. Die analitiese modelle wat gebruik word om die vloei van materiale te voorspel, het 'n algemene aanvaarbare ontwerpinstrument geword. Daar is egter 'n aantal veranderlikes wat hierdie modelle ignoreer en daarom die akkuraatheid en toepassing daarvan beperk. Die diskrete element metode (DEM), wat in 1971 deur Peter A. Cundall bekendgestel is, het ontwikkel tot 'n gewilde ontwerpinstrument vir die verbetering van toerusting en prosesse vir grootmaat-materiaalhantering. DEM het die vermoë om die ingewikkelde interaksie tussen diskrete partikels en partikels-en-mure (strukture) te modelleer en ontwerpers kan dit gebruik om die werkverrigting van hul ontwerpe te kwantifiseer. Die grootste probleem met die gebruik van DEM, is egter die kalibrasie en validering van die materiaal eienskappe. Onakkurate kalibrasie van DEM modelle kan lei tot onakkurate resultate en gevolglik tot onvoldoende ontwerpe.

Die doel van hierdie studie was om die vermoë en akkuraatheid waarmee DEM (PFC3D) die vloei van droë materiaal deur vervoeroordragspunte kan voorspel, te ondersoek. Mieliepitte was gebruik as die toetsmateriaal wat verskillende niesferiese vorms en groottes insluit. Die materiaal eienskappe van die mieliepitte is bepaal deur verskillende toetse te implementeer. Die vorm van die partikels is gemodelleer as sfere en multisfere, en verdere kalibrasietoetse is uitgevoer om 'n akkurate stel parameterwaardes te verkry.

Die skuins vervoerbande wat in die eksperimentele toetse gebruik is, het 'n chevron patroon bevat om meer beheer oor die massa vloeitempo te gee, veral by hoër snelhede. Die chevron patroon het veroorsaak dat minder materiaal na die voedingsone terugrol, en die insluiting daarvan in die DEM model is eers ondersoek en gevalideer. Die verskillende komponente van 'n vervoeroordragspunt wat ondersoek was, het 'n impakplaat, oordrag-kap, klipbank en 'n glygeut ingesluit. Die voorspelde materiaalvloei eienskappe (impakskragte, snelhede en vloeipatrone) was geverifieer deur die resultate met die "particle image velocimetry" (PIV) analise van hoë-spoed video's te vergelyk. Simulasie strategieë soos partikel-vergroting, vereenvoudiging van die partikel model en vermindering van die kontakstyfheid was ondersoek om die simulasie tyd te verminder.

DEM het die impakskrag ($|\text{fout}| \leq 8.57$ %), snelheid ($|\text{fout}| \leq 5.31$ %), uitvloeisnelheid ($|\text{fout}| \leq 19.90$ %) en ander ondersoekende vloeipatrone op 'n vertikale impakplaat akkuraat voorspel, asook die vloeipatrone in en vanaf 'n klipbank, deur 'n kap en die massa vloeitempo wat lei tot geutblokkering ($|\text{fout}| \leq 5.00$ %). Die maksimum partikel-skaalfaktor vir die akkurate voorspelling van die vloei teen die impakplaat was 7.0, terwyl die partikels slegs tot 1.6 geskaal kon word vir

die klipbank en geutblokkering. Die analitiese model het egter minder akkurate resultate gelewer in die voorspelling van die impakskrag (|fout| ≤ 14.17 %), snelheid (|fout| ≤ 6.14 %) en die uitvloei-snelheid (|fout| ≤ 19.38 %) op ’n vertikale impakplaat. Die gevolgtrekking is dat DEM akkuraat die materiaalvloei deur ’n vervoeroordragstelsel kan voorspel en met vertroue in industriële toepassings gebruik kan word as ’n gepaste stel gekalibreerde parameters gebruik word.

Acknowledgements

I wish to express my deepest gratitude to my supervisor, Professor Corné Coetzee, for giving me the opportunity to do research and for his invaluable guidance and encouragement throughout the thesis. I'm extremely grateful and privileged to have worked and studied under his guidance.

Thank you to the technical staff of the Mechanical and Mechatronic Engineering Department of Stellenbosch University for the assistance in the laboratory and manufacturing of test equipment. Thanks also go to Mr Otto Scheffler for all his assistance and advice.

Most importantly, thank you to my family for their financial and emotional support. Without you, none of the work done would have been possible.

Table of Contents

List of Figures

List of Tables

Nomenclature

Roman Symbols

A_a	Cross-sectional area of material after impact	m^2
A_p	Cross-sectional area of material before impact	m^2
a	Acceleration	m/s^2
B	Chute width	m
B_0	Initial chute width	m
b_t	Belt thickness	m
b_w	Belt width	m
c_n	Normal damping coefficient	N s/m
c_s	Shear damping coefficient	N s/m
D_{ev}	Equivalent volume diameter	mm
D_p	Pulley diameter	mm
$d_{\max}$	Maximum particle diameter	mm
F^d	Dashpot (damping) component of contact force	N
F^l	Linear (spring) component of contact force	N
F_c	Contact force	N
F_n^d	Damping normal force	N
F_n^l	Linear normal force	N
F_s^d	Damping shear force	N
F_s^l	Linear shear force	N
F_s^μ	Shear strength	N
F_s^*	Initial shear force (assumption)	N
$(F_s^l)_0$	Linear shear force at the start of the timestep	N
f	Frequency	Hz
g	Gravitational acceleration	m/s^2
g_c	Contact gap	m
g_s	Surface gap	m
H	Material stream bed depth (Section 4.3)	m
H	Material build-up height after hitting the impact plate	mm
H_0	Initial stream bed depth	m
H_b	Rock box build-up height	mm
h_b	Material stream thickness	mm
K	Constant of integration	-
K_v	Pressure ratio	-
k	Stiffness	kN/m
k_n	Normal stiffness	kN/m
k_{pp}	Particle-particle stiffness	kN/m
k_{pw}	Particle-wall stiffness	kN/m
k_r	Rolling resistance stiffness	kN/m
k_s	Shear stiffness	kN/m
L	Horizontal distance between load cells	m

m	Element mass	kg
$m^{(1,2)}$	Mass of particles in contact	kg
m_c	Effective inertial mass	kg
m_{particle}	Particle mass	kg
$\dot{m}$	Mass flow rate	kg/s
$\overrightarrow{\text{N}_\text{f}}$	Facet normal vector	-
$\hat{n}_c$	Contact-plane normal direction	-
$\overrightarrow{\text{P}_\text{f}}$	Rotated vector	-
R	Magnitude of impact force	N
R	Hood curvature radius (Sections 4.3 and 9)	m
$\overline{R}$	Contact effective radius	m
$\overline{R}^{(1,2)}$	Radius of contacting particles	m
$\overrightarrow{\text{R}_\text{f}}$	Rotation vector	-
R_n	Normal component of impact force	N
R_p	Head pulley radius	m
R_s	Shear component of impact force	N
R_t	Curvature radius of trajectory stream	m
r_{avg}	Average particle radius	m
S	Distance from the head pulley to impact plate	m
S_0	Distance from the head pulley to point of discharge	m
s	Curvature length of chute	m
$\hat{s}_c$	Vector component in s-axis, parallel to contact-plane	-
T	Period	s
T^*	Torque limit value	N m
T^r	Rolling resistance torque	N m
T^r_s	Rolling resistance torque component in s-axis	N m
T^r_t	Rolling resistance torque component in t-axis	N m
$T_{\text{p, gen}}$	Period at which the particles were released	s
$T_{\text{piled-up}}$	Period of the piled-up material between the chevron pattern	s
$T_{\text{successive}}$	Period of successive chevron patterns	s
t	Time	s
$\hat{t}_c$	Vector component in t-axis, parallel to contact-plane	-
t_{crit}	Critical timestep	s
V	Volume	m^3
$\text{V}_{\text{particle}}$	Particle volume	m^3
V	Mass element velocity through hood	m/s
V_0	Initial material velocity (hood)	m/s
V_1	Velocity of a particle before impact	m/s
V_2	Velocity of a particle after impact	m/s
V_a	After-impact/outflow velocity (impact plate)	m/s
V_b	Conveyor belt speed	m/s
V_d	Discharge velocity from head pulley	m/s
V_i	Impact velocity (rock box)	m/s

V_o	Outflow velocity (rock box)	m/s
V_p	Impact velocity (impact plate)	m/s
V_{pn}	Normal impact velocity component	m/s
V_{px}	x-component of impact velocity	m/s
V_{py}	y-component of impact velocity	m/s
W	Material outflow width after hitting the impact plate	mm
x	Horizontal distance	mm
x_a	Length of piled-up material between the chevron pattern	m
x_c	Contact-plane location	m

Greek Symbols

α_b	Conveyor belt inclination angle	°
α_d	Material discharge angle from head pulley	°
α_{i}	Material impact angle (rock box)	°
α_{o}	Material outflow angle (rock box)	°
α_p	Material impact angle (impact plate)	°
β	Impact plate tilt angle	°
β_n	Normal critical-damping ratio	-
β_s	Shear critical-damping ratio	-
ρ_{a}	Bulk material density after impact	kg/m^3
ρ_{b}	Bulk material density	kg/m^3
$\rho_{\mathrm{b,\ previous}}$	Previous bulk density	kg/m^3
$\rho_{\mathrm{b,\ target}}$	Target bulk density	kg/m^3
ρ_{p}	Particle density	kg/m^3
$\rho_{\mathrm{p,\ new}}$	Updated particle density	kg/m^3
$\rho_{\mathrm{p,\ previous}}$	Previous particle density	kg/m^3
ζ_{pp}	Particle-particle contact damping	N s/m
ζ_{pw}	Particle-wall contact damping	N s/m
θ	Angular position	°
θ_0	Starting angular position	°
θ_{bed}	Material slump angle (rock box)	°
μ	Coefficient of friction	-
μ_e	Equivalent friction coefficient	-
$\mu_{\mathrm{k,\ pw}}$	Kinetic particle-wall friction	-
μ_{pp}	Particle-particle sliding friction	-
μ_{pw}	Particle-wall sliding friction	-
$\mu_{\mathrm{r\ pp}}$	Particle-particle rolling friction	-
$\mu_{\mathrm{r\ pw}}$	Particle-wall rolling friction	-
$\mu_{\mathrm{s,\ pw}}$	Static particle-wall friction	-
μ_{w}	Coefficient of wall friction	-
ϵ_1	Lower stream divergent coefficient (Golka)	-
ϵ_2	Upper stream divergent coefficient (Golka)	-

Δm	Mass of element	kg
ΔV	Change in volume	m^3
$\Delta \delta_n$	Normal relative displacement increment	m
$\Delta \delta_s$	Shear relative displacement increment	m
$\Delta \theta_b$	Relative bend-rotation increment	°
$\dot{\delta}_n$	Relative normal translation velocity	m/s
$\dot{\delta}_s$	Relative shear translation velocity	m/s
λ	Chute width convergence angle	°

Acronyms and Abbreviations

2D	Two-dimensional
3D	Three-dimensional
CAD	Computer-aided design
CDU	Controller/display unit
CF	Compact Flash
COR	Coefficient of restitution
CPU	Central processing unit
DEM	Discrete Element Method
FFT	Fast Fourier transform
fps	Frames per second
HMI	Human machine interface
LCD	Liquid crystal display
LSD	Linear spring dashpot
PFC	Particle Flow Code
PIV	Particle Image Velocimetry
PLC	Programmable logic controller
px	Pixels
rpm	Revolutions per minute

1 Introduction

Conveyor systems are mechanical systems used to move a bulk of material from one point to another with minimal effort, usually using conveyor belts. The main goal is to efficiently control the mass flow of material through the system while minimising transfer issues. These transfer issues include dust generation, chute and belt wear, belt mistracking, particle attrition, excessive noise and spillage caused by the mass flow rate being too high. When the mass flow rate is too low, stagnation zones can develop resulting in spillage or chute blockage. Common bulk solid materials transferred through conveying systems include any aggregate material such as gravel, corn, pellets, coal, iron ore, etc. (Hastie, 2010).

It is of utmost importance that a conveyor system is well designed since it can become extremely costly, especially for the mining industry which has continuous production, if the conveyor system does not perform according to its specifications. The efficiency of a conveyor system solely depends on the design of the transfer chutes since it is frequently the cause of production delays through promoting transfer issues. A well-designed transfer chute does not need regular repair or replacement of the transfer chute or conveyor belt, therefore, necessary attention needs to be considered during the design phase (Donohue et al., 2019). Inadequate design specifications in the early stages of the project have a significant influence on the control and ability to change the final design outcomes, and so to do modifications at a later stage of the project will be expensive. Therefore, performance-based designs should be considered as early as possible (Ilic, 2019). There are numerous analytical models to predict the motion of the particles through transfer chutes, but the biggest issue with the models is that they don't take all the variables into consideration, i.e. particle properties. The material flow deviates from the characteristics of idealised free-flowing material since the bulk of the material consists of a large number of particles which induce forces on each other, affecting the flow of the material. It is therefore becoming vastly complex to apply the theory of dynamics to the trajectory of a stream of particles (Hastie, 2010).

The discrete element method (DEM) has become popular since it is a numerical modelling technique which distinctively models the interaction between the individual particles and between the particles and a structure such as a transfer chute. The internal forces, moments, velocities, rotations and displacements are calculated for every particle at each time step (Donohue et al., 2019). Engineers use DEM to assist in their chute designs since it eliminates the need to build expensive test chutes for testing different designs. Since DEM modelling has only recently become popular, its accuracy in predicting material flow through transfer chutes should still be carefully and scientifically determined. Another concern in DEM is the computational time needed to complete a numerical simulation, which depends heavily on the modelled particle shape and size. In the

industry, many companies scale the particles in order to get faster computational times, but little is known on how much scaling influences the results (Hastie, 2010).

The focus of this study was to investigate and validate the accuracy of DEM in predicting the flow of cohesionless granular material (corn grains) through various transfer points, i.e. impact plate, hood, rock box and chute. PFC3D (2019) was used throughout for the DEM analyses. An existing conveyor system in the Granular Materials Research Group's laboratory was used for all physical experiments. After the material properties of corn grains were successfully determined, calibration tests were performed to obtain a set of modelling parameters for DEM. To validate the DEM simulations the results were compared to results of analytical (continuum) models and high-speed footage of the material flow, which was analysed using particle image velocimetry (PIV). Ball and multi-sphere particle shape models were investigated to determine whether a simplified shape model could still yield accurate results. Furthermore, it was found by numerous researchers that the particles could be successfully scaled to a certain point, depending on the nature and application of the DEM model (Coetzee, 2019). Hence, the maximum scaling factor was investigated for the impact plate, rock box and chute, to identify a scaling factor for typical conveyor applications.

2 Objectives

As mentioned above, the aim of this project was to determine how accurate discrete element modelling can predict particle flow through a conveyor transfer system. Therefore, the objectives of the project were:

1. Determine the DEM parameters for the ball and multi-sphere (clumps) particle shape models.
2. Determine the accuracy with which DEM can predict the flow of bulk material through a conveyor transfer chute. Measures to be analysed include the following:
   (a) Flow trajectory from the feeding conveyor into the chute.
   (b) Impact velocity, angle, force and any flow behaviour on an impact plate.
   (c) Impact position, velocity profile and any flow behaviour on a hood.
   (d) Impact velocity, angle, build-up in, and flow from a rock box.
   (e) Mass flow rate into and out of the chute, and any build-up.
3. Determine the most accurate and efficient DEM model for the particle shape and scale for this application.

The research hypotheses for this project is that DEM can accurately predict bulk material flow through a given conveyor transfer system and identify possible design flaws.

3 Motivation

The use of discrete element modelling in industry has increased over the years, yet no way has been found to fully establish the dynamic behaviour of bulk material flow through a conveyor transfer system. For many years, the design of conveyor transfer systems has been based on trial-and-error or past experience. There are numerous analytical models derived from trajectory theory, but these models have to make certain assumptions in order to be useful. Although DEM can eliminate most of these assumptions, the accuracy with which it can predict the flow behaviour of material through a transfer system has not yet been scientifically determined. With a validated DEM modelling approach the industry can save money and time during the design process but also and more importantly, during operation and maintenance of the transfer system. This will maximise production and reduce environmental pollution such as dust and spillage.

Roy Hill is an iron ore mine located in Western Australia's Pilbara region, which produces 60 million tonnes of iron ore per annum (Operations Overview | Roy Hill, 2020). It was found that the mine experienced unscheduled downtime due to inefficient transfer chute designs. As a result, ore build-up in the chutes was identified, as well as adverse loading conditions causing idler failure on the receiving conveyors. Donohue et al. (2019) successfully identified the problems using DEM, consequently, improving the transfer chutes. After implementing the new designs, Roy Hill mine's downtime per week decreased from 7 - 30 hours to 0 - 5 hours.

Ilic (2019) presented a DEM modelling case study by investigating the sensitivity of transfer chute design geometries to the resulting chute and belt wear life. The initial design was first investigated, followed by three alternative designs. Ilic (2019) successfully identified, for all four designs, the location and magnitude of wear on the chute and belt, as well as the design faults causing an increase in wear. It was concluded that the chute and belt service life could be increased by approximately 132 % and 139 %, respectively.

4 Literature Review

In this section, literature regarding different transfer chute designs (transfer hood, rock box and impact plate) in conveyor systems, analytical models to predict the material flow onto an impact plate and through a hood and fundamentals of DEM such as material calibration, DEM contact model and the effect of the

particle shape and particle scaling are presented.

4.1 Transfer Chute Designs

Transfer chutes are an important part of conveyor systems since it transfers the material or product from conveyor A to conveyor B. The efficiency of the conveyor system depends solely on the design of the chute since a bad design can cause an undesirable loading mass flow rate and provoke transfer issues. The design of transfer chutes should consider central, uniform and in line with the belt loading as well as minimising the differential velocity between the material and the receiving belt speed, and at the same time prevent chute and belt wear, dust emissions, spillage and blockages (Ilic and Donohue, 2015). The chute configuration depends on the material properties of the bulk material or the specific requirements of the system layout (Mascarenhas and Mesquita, 2013). There are various transfer chute configurations used in the industry; however, it depends on the designed performance of the chute. The main components used for transfer chute designs are a transfer hood, spoon, rock box and an impact plate.

4.1.1 Transfer Hood

Transfer hoods are usually used in a hood-spoon configuration, where its main purpose is to change the direction of the flow without significantly decelerating it. As a result, the kinetic energy is not entirely lost and the material do not have to be accelerated once the material loads onto the receiving conveyor belt. Transfer hoods should, however, not be used for abrasive materials since it can lead to significant damage to chute elements. The curvature of the hood is an important aspect of the hood design. It should capture the material stream and redirect it to the following component while minimising spillage and wear (Halpin, 1993). A basic hood design can be seen in Figure 1a.

4.1.2 Rock Box

The main objective of a rock box design is to avoid initial particle-wall contacts from the inflowing granular material, but rather impose particle-particle contacts. Rock boxes are mainly used for abrasive materials such as ore since these materials can cause significant damage to the transfer chutes. Rock boxes should, however, not be used when the differential velocity between the material being loaded and the receiving conveyor belt speed is large since this can cause significant wear to the belt as well as spillage. A solution would be to use the rock box in conjunction with another chute element to speed up the material (Mascarenhas and Mesquita, 2013). A typical rock box design can be seen in Figure 1b.

4.1.3 Impact Plate

An impact plate absorbs the collision of the material stream coming from the head pulley. Impact plates are only used to ensure that there is no heavy contact of the material stream on the structure of the system when no directional variation of the velocity component is necessary. Two impact plate designs are shown in Figure 1c. The design on the left is for high belt speed conditions where the purpose of the impact plate is to eliminate the material's horizontal velocity component and so absorb most of the damage and wear to protect the rest of the chute. The figure on the right is for low belt speed conditions where the impact plate absorbs the vertical velocity component, and consequently protects the receiving conveyor belt from impact wear and provides a uniform flow on the belt. The design objective of an impact plate is to design it with the correct selection of material type and geometry, in order to bear the impact and abrasive wear and as a result to achieve an acceptable lifetime (Scott and Choules, 1993).

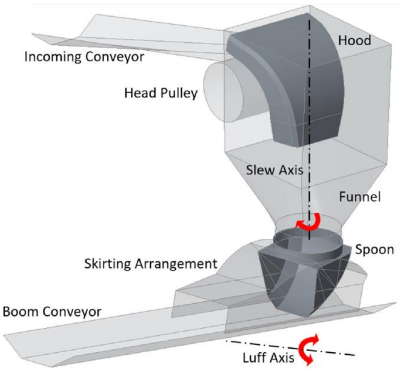

(a) Transfer hood chute (Ilic et al., 2019).

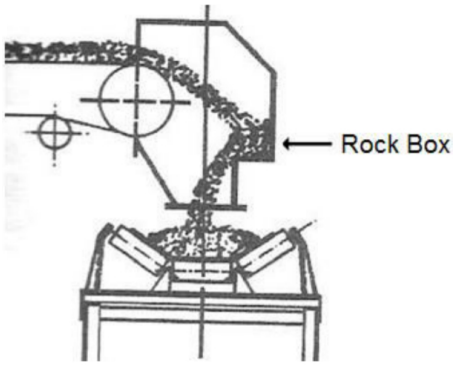

(b) Rock box chute (Chaves et al., 2011).

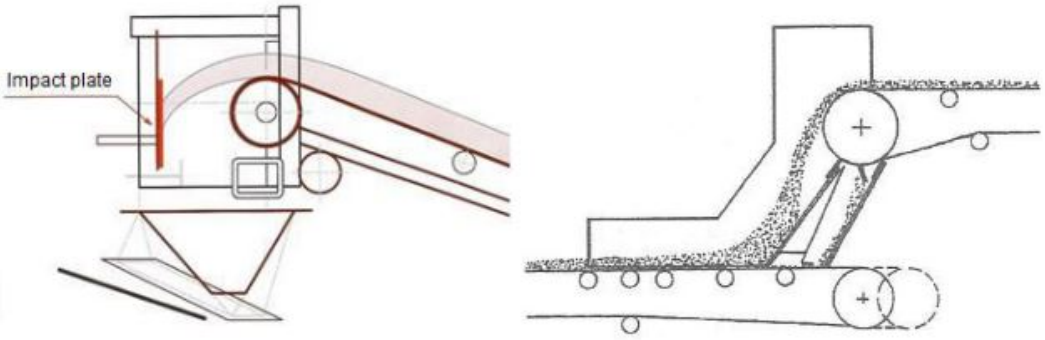

(c) Impact plate (Benjamin et al., 2010; Chaves et al., 2011).

Figure 1: Transfer chute designs.

4.2 Impact Plate Analytical Model

Research has shown that rheological approaches such as impulse-momentum balance and Bernoulli's principle for a specified control volume have provided acceptable results regarding the forces and velocities of bulk materials colliding

on an impact plate (Grima and Wypych, 2010a). Furthermore, Korzen (1988) developed a model which is based on Newton's laws of motion for bulk materials acting as a continuum. The model is simplified by evaluating the flow in only two dimensions. The disadvantage of this model is that material which diverges away from the mainstream, after impact, is not considered in the formulation. Korzen's (1988) model (Figure 2) includes the belt inclination angle α_b which is assumed to be the same as the discharge angle α_d, the discharge velocity V_d which is the same as the belt speed V_b, the angle of the impact plate β and the thickness of the material stream h_b. These assumptions were made since the analysis are done only for high-speed conditions.

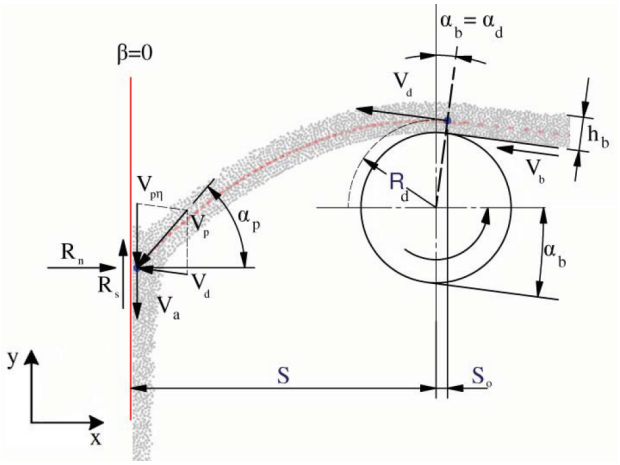

Figure 2: Bulk material flow onto impact plate (Korzen, 1988).

Assuming $\alpha_d = \alpha_b$ and $V_d = V_b$, the impingement angle of the flow onto the impact plate, α_p, is given by,

$$\alpha_p = \tan^{-1}\left[\tan\alpha_d - g\,(S \pm S_0)\,V_d^{-2}\,\cos^{-2}\alpha_d\right] \tag{4–1}$$

where S is the distance from the head pulley to the impact plate and S_0 is the distance between the head pulley and the material discharge point. By means of Newton's laws the incoming velocity onto the impact plate is given by,

$$V_p = \sqrt{V_{pn}^2 + V_d^2 + 2\,V_{pn}\,\cos(90° \pm \alpha_d)} \tag{4–2}$$

where

$$V_{pn} = \frac{g\,(S \pm S_0)}{V_d\,\cos\alpha_d} \tag{4–3}$$

Korzen (1988) incorporated the following relation which must be satisfied to insure that steady flow occurs, i.e. where the velocity of the particles at a particular fixed point on the trajectory stream does not change with time,

$$\alpha_p + \beta > \tan^{-1}\sqrt{\mu_w} \tag{4–4}$$

If this relation is satisfied, the following iterative approach to converge V_a is used to determine the velocity of the stream after impact:

The first step is to determine the initial out-flowing stream area, A_{a1}, and the initial after impact velocity, V_{a1}, using the following equation,

$$V_{a1} = V_p \sqrt{\sin^2(\alpha_p + \beta) - \mu_w \cos^2(\alpha_p + \beta)} \tag{4–5}$$

where

$$A_{a1} = A_p = \frac{\dot{m}}{V_p \rho_b} \tag{4–6}$$

The steps that follow are to determine the next out-flowing area, A_{a2}, and velocity, V_{a2}, in an iterative procedure until the relative error between successive steps is approximately 1 %. The iterative equation is,

$$V_a = V_{a2} = V_p \sqrt{\frac{A_p}{A_{a2}} \left[\sin^2(\alpha_p + \beta) - \mu_w \cos^2(\alpha_p + \beta) \right]} \tag{4–7}$$

where

$$A_a = A_{a2} = A_p = \frac{\dot{m}}{V_{a1} \rho_b} \tag{4–8}$$

However, if steady flow does not occur, the following relation must be satisfied,

$$\alpha_p + \beta > \tan^{-1} \mu_w \tag{4–9}$$

For this case the out-flowing velocity V_a and area A_a are not iteratively determined, but is expressed as:

$$V_a = V_p \left(\sin(\alpha_p + \beta) - \mu_w \cos(\alpha_p + \beta) \right) \tag{4–10}$$

$$A_a = \frac{\dot{m}}{V_a \rho_b} \tag{4–11}$$

The reaction forces on the impact plate are further evaluated by means of the impulse-momentum equation, $\mathrm{d}m(\vec{V_p} - \vec{V_a}) = \vec{R}\,\mathrm{dt}$. From the continuity equation, it is assumed that the bulk density at discharge stays the same after impacting the plate, therefore, $\rho_b = \rho_a$ (Korzen, 1988). By determining the relationship between the incoming stream's velocity and area and the outgoing stream's velocity and area, the normal and shear forces are evaluated as:

$$\begin{aligned} R_n &= V_{px}^2 \rho_b A_p \\ &= \rho_b A_p \left(V_p (\cos \alpha_p + \beta) \right)^2 \\ &= \dot{m} V_p \cos^2(\alpha_p + \beta) \end{aligned} \tag{4–12}$$

$$\begin{aligned} R_s &= \rho_{\mathrm{b}}\ A_p\ V_{py}^2 - \rho_{\mathrm{a}}\ A_a\ V_a^2 \\ &= \rho_{\mathrm{b}}\ A_p\ \left(V_p\ \sin(\alpha_p+\beta)\right)^2 - \rho_{\mathrm{b}}\ A_a\ V_a^2 \\ &= \dot{m}\ V_p\ \sin^2\left(\alpha_p+\beta\right) - \dot{m}\ V_a \end{aligned} \tag{4–13}$$

The shear force from equation 4–13 can also be written i.t.o. the normal force R_n,

$$R_s = R_n\ \mu_{\mathrm{w}} \tag{4–14}$$

which can be used solely to estimate the shear force R_s when the outgoing velocity V_a cannot be accurately approximated by equations 4–7 and 4–10 (Korzen, 1988).

4.3 Hood Trajectory Model

The theory of Roberts (2003, 2004), further derived an equation of motion which predicts the velocity profile of the material stream through a hood, Figure 3a. This theory is only valid when the radius of curvature of the discharge trajectory, R_t, is larger than the pulley radius R_p, i.e. $R_t \geq R_p$. The radius of curvature R_t relation is given by,

$$R_t = \frac{\left[1+\left(\frac{g\ x}{V_b^2\ \cos^2\theta}\right)^2\right]^{1.5}}{\left(\frac{g}{V_b^2\ \cos^2\theta}\right)} \tag{4–15}$$

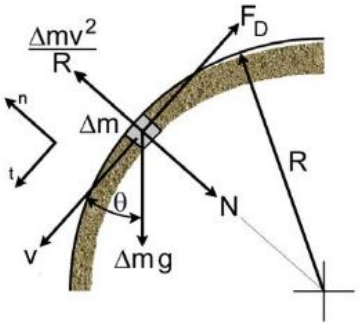

(a) Force diagram for flow through a hood (Hastie, 2010).

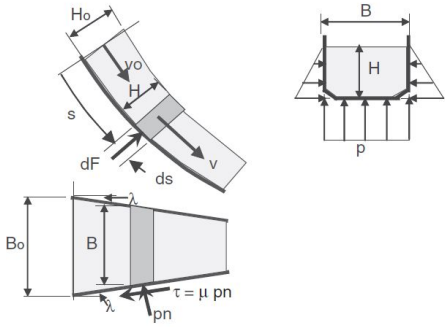

(b) Converging cross-sectional chute (Roberts, 2003).

Figure 3: Transfer hood trajectory model (a) force diagram and (b) chute configurations.

According to Roberts (2003, 2004), the equation of motion for the material stream through a hood is defined by,

$$-\frac{\mathrm{d}V}{\mathrm{d}\theta} + \mu_e\ V = \frac{g\ R}{V}(\cos\theta + \mu_e\ \sin\theta) \quad \text{for} \quad \frac{V^2}{R\ g} \geq \sin\theta \tag{4–16}$$

where R is the radius of curvature of the chute, μ_e is the friction equivalent coefficient and θ is the angular position of the material element measured from the bottom of the hood in a clockwise direction. The equivalent friction coefficient for a hood having a constant rectangular cross-section is determined by,

$$\mu_e = \mu \left[1 + K_v \frac{H}{B}\right] \tag{4–17}$$

and for a chute having a converging rectangular cross-section,

$$\mu_e = \mu \left(1 + \frac{C_2}{V\, B^2}\right) \tag{4–18}$$

where

$$C_2 = K_v\, B_0\, H_0\, V_0 \left(1 + \frac{\tan\lambda}{\mu}\right) \tag{4–19}$$

K_v is the pressure ratio which is normally between 0.4 and 0.6, V_0 the initial velocity, B_0 the initial chute width, H and H_0 the average and initial stream bed depth and λ the chute width convergence angle. The chute width B is defined by,

$$B = B_0 - 2\, s\, \tan\lambda \tag{4–20}$$

where s is the distance down the chute. For a curved chute, s will be equal to the curved length. The converging cross-sectional chute is shown in Figure 3b. By numerically integrating the equation of motion, 4–16, and assuming the friction coefficient μ_e is constant over the surface of the hood, the velocity of the material stream as a function of the curvature angle, θ, is expressed as:

$$V = \sqrt{\frac{2\, g\, R}{4\, \mu_e^2 + 1}\left[\sin\theta\left(2\, \mu_e^2 - 1\right) + 3\, \mu_e\, \cos\theta\right] + K\, \mathrm{e}^{2\, \mu_e\, \theta}} \tag{4–21}$$

Where K is the constant of integration and is solved by substituting the initial conditions, $V = V_0$ and $\theta = \theta_0$, in the following equation,

$$K = \left[V_0^2 - \frac{2\, g\, R}{4\, \mu_e^2 + 1}\left[3\, \mu_e\, \cos\theta_0 + \left(2\, \mu_e^2 - 1\right)\, \sin\theta_0\right]\right] \mathrm{e}^{-2\, \mu_e\, \theta_0} \tag{4–22}$$

4.4 Fundamentals of DEM

The discrete element method (DEM) is a numerical method used to simulate the discontinuous flow of granular materials and improve conveyor system designs and performance. The flow of granular materials during loading, conveying, discharging from the head pulley and flowing through different transfer chutes yields complex flow dynamics and can therefore become very complicated to predict using analytical models. Analytical models only provide a good estimate for the trajectory and velocity of granular materials through a transfer point but

are generally limited to 2-D analysis (Grima and Wypych, 2010a). Moreover, the analytical model considers the material flow as a lumped mass and therefore neglects the particle-particle interactions.

DEM has the ability to simulate the model as a discrete system; therefore, the material flow characteristics of each particle and the interaction between the particles and the rigid body structures can be quantified at any given timestep (Grima and Wypych, 2010a). The discrete element method is very sensitive to certain input parameters, depending on the modelling application. Therefore, caution has to be taken when selecting the parameters. The physical material properties of granular materials can be distinguished between microscopic - and macroscopic properties. The microscopic properties include the particle density, particle shape and size, coefficient of restitution (contact damping), contact friction, and particle stiffness, where at the macroscopic level the material density, porosity, angle of repose, surcharge angle, and the internal friction angle defines the material properties and behaviour of granular materials at bulk level (Coetzee, 2017). The model parameters can only be specified at the microscopic level. According to Coetzee (2017), there are two approaches for selecting the DEM parameters, i.e. the *direct measuring approach* and the *bulk calibration approach*. The calibration of the DEM parameters with the two calibration approaches is further discussed below.

4.4.1 Calibration of DEM Models

It is essential to do calibration to have confidence that the modelled particle physics are sensible and accurate, since bulk materials have random particle shapes and variation in material properties. In industry, DEM models are mostly simplified by using spherical shapes that represent the irregular particle shapes. Another popular tendency is to scale the parameters of the particles to decrease computational time. Calibration of the model parameters and contact models are therefore needed to compensate for these changes (Grima, 2011). The typical trend in DEM is to select large particles with relatively low stiffness to minimize the simulation time. However, this might provide inaccurate results depending on the application.

According to literature, there is a lack of techniques for the calibration of bulk materials in DEM models. This entails obtaining a reference point by doing physical experiments which can be compared to standard benchmark tests. Although, extensive research has been done on techniques to determine the flow characteristics of granular materials. A method to determine the input parameters for the DEM model is by directly measuring the material properties at the particle or contact level, i.e. the *direct measuring approach*. The problem with using this approach is the uncertainty of whether the measured microscopic properties will provide accurate bulk behaviour predictions. Factors like the shape and size of the model particles and contact models which are not accurate representatives of

the specific application, influence the level of accuracy of the results. Most of the granular materials shapes are very difficult to model accurately, due to computational limitations (Coetzee, 2017). Although it is becoming possible to obtain more accurate particle shapes and sizes, the computational time will increase.

The best strategy to obtain accurate bulk material behaviour is to execute calibration tests to provide a link between the true material properties and simulation parameters, i.e. the *bulk calibration approach*. These calibration tests include the angle of repose, internal and wall friction tests where the microscopic simulation parameters are "tuned" to fit the macroscopic behaviour (Grima, 2011). According to Coetzee (2017), the bulk material behaviour of the numerical simulation can be influenced by more than one parameter. As a result, there cannot be a unique solution since multiple combinations of the parameter values can result in the same bulk material behaviour. Coetzee (2017) also added that the calibration test must be different from the application being modelled. If the application and calibration test is the same, the parameter values will only be tuned until the desired material behaviour is obtained. This will not help the user to design a new system where the bulk material behaviour should be predicted.

4.4.2 Contact Force Models

The contact model considered in this study is the linear spring-dashpot (LSD) model which is based on a soft sphere contact model.

4.4.2.1 Linear Spring-Dashpot (LSD) Model

The linear model consists of elastic and damping (viscous) components which act in parallel to one another (see Figure 4a). The contact force F_c is defined by,

$$F_c = F^l + F^d \tag{4–23}$$

where F^l and F^d are the linear (spring) and dashpot (damping) components, respectively (Itasca, 2019).

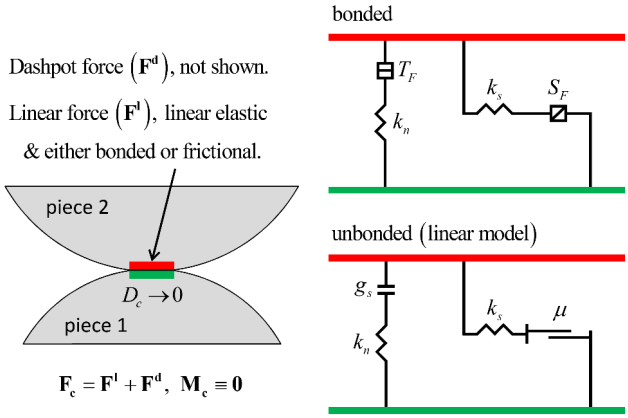

(a) Linear spring-dashpot model.

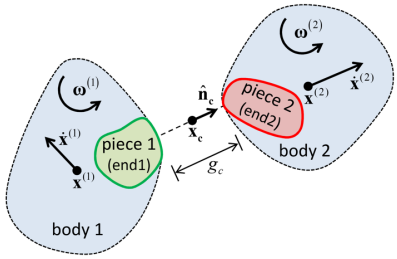

(b) Contact between two bodies.

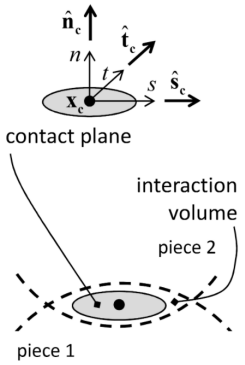

(c) Contact plane coordinate system.

Figure 4: Linear spring-dashpot (LSD) model (Itasca, 2019).

A schematic diagram for the contact between two bodies is shown in Figure 4b with x_c the contact location vector, $\hat{n}_c$ the contact-plane normal direction and g_c the contact gap. Contact between two bodies (or body and wall) is active only when the surface gap g_s is smaller or equal to zero. The relative displacement increment of the bodies is given by $\Delta\delta_n$ and $\Delta\delta_s$ for the normal and shear directions respectively with a timestep Δt. From equation 4–23, the linear and dashpot forces are broken down into normal and shear components,

$$\begin{aligned} F^l &= -F_n^l \, \hat{n}_c + F_s^l \\ F^d &= -F_n^d \, \hat{n}_c + F_s^d \end{aligned} \tag{4–24}$$

where F_n^l and F_n^d are smaller than zero otherwise the contact force is in tension which is not possible since the force-displacement law is based only on normal compression forces. The linear normal force F_n^l is therefore given by,

$$F_n^l = \begin{cases} k_n \, g_s & , \quad g_s < 0 \\ 0 & , \quad \text{otherwise} \end{cases} \tag{4–25}$$

The linear shear force F_s^l depends on whether there is sliding or frictional contact (Itasca, 2019). First the assumption is made that there is slip occurring. The shear

force is then given by,

$$F_s^* = \left(F_s^l\right)_0 - k_s\,\Delta\delta_s \tag{4–26}$$

where $\left(F_s^l\right)_0$ is the linear shear force at the start of the timestep and $\Delta\delta_s$ is the updated relative shear-displacement increment. The shear strength is determined by multiplying the friction coefficient (particle-particle or particle-wall) μ with the linear normal force F_n^l:

$$F_s^\mu = -\mu\,F_n^l \tag{4–27}$$

Depending on the slip condition, the linear shear force is given by,

$$F_s^l = \begin{cases} F_s^* & , \quad ||F_s^*|| \le F_s^\mu \\ F_s^\mu\left(F_s^*/||F_s^*||\right) & , \quad \text{otherwise} \end{cases} \tag{4–28}$$

The dashpot normal and shear force components are defined by,

$$F_n^d = \left(2\,\beta_n\,\sqrt{m_c\,k_n}\right)\dot{\delta}_n = c_n\,\dot{\delta}_n \tag{4–29}$$

and

$$F_s^d = \left(2\,\beta_s\,\sqrt{m_c\,k_s}\right)\dot{\delta}_s = c_s\,\dot{\delta}_s \tag{4–30}$$

with

$$m_c = \begin{cases} \frac{m^{(1)}\,m^{(2)}}{m^{(1)}+m^{(2)}} & , \quad \text{particle-particle} \\ m^{(1)} & , \quad \text{particle-wall} \end{cases} \tag{4–31}$$

where $m^{(1,2)}$ are the masses of the particles in contact, β_n and β_s the normal and shear critical-damping ratios, $\dot{\delta}_n$ and $\dot{\delta}_s$ the relative normal and shear translation velocities, and c_n and c_s the normal and shear damping coefficients (Itasca, 2019).

The rolling resistance mechanism is added by incorporating a torque acting on the two contacting surfaces to counteract the rolling motion. The rolling resistance torque i.t.o. the contact plane coordinate system (Figure 4c) is determined by,

$$T^r = T_s^r\,\hat{s}_c + T_t^r\,\hat{t}_c \tag{4–32}$$

where T_s^r and T_t^r are the torque components in the s- and t-axis, respectively. However, the magnitude of the rolling resistance torque is first checked against a threshold limit,

$$T^r = \begin{cases} T^r & , \quad ||T^r|| \le T^* \\ T^*\,(T^r/||T^r||) & , \quad \text{otherwise} \end{cases} \tag{4–33}$$

where the limiting torque T^* is defined by

$$T^* = \mu_{\mathrm{r\,pp}}\,\overline{R}\,F_n^l \tag{4–34}$$

$\overline{R}$ is the contact effective radius and is given by,

$$\frac{1}{\overline{R}} = \frac{1}{\overline{R}^{(1)}} + \frac{1}{\overline{R}^{(2)}} \tag{4–35}$$

where $\overline{R}^{(1,2)}$ are the radii of the contacting particles. If the particle is in contact with a wall, then $\overline{R}^{(2)} = \infty$. The rolling resistance torque is incrementally updated with,

$$T^r = T^r - k_r\,\Delta\theta_b \tag{4–36}$$

where k_r is the rolling resistance stiffness and $\Delta\theta_b$ the relative bend-rotation increment. The rolling resistance stiffness is determined by multiplying the shear stiffness k_s with the square of the contact effective radius $\overline{R}$,

$$k_r = k_s\,\overline{R}^{(2)} \tag{4–37}$$

The linear spring-dashpot contact model is the most used in industry since the necessary contact stiffness in the model is lower than in other models such as the Hertz-Mindlin contact model. Lower stiffness in DEM simulations decreases the computational time significantly. Research has shown that LSD contact models are the best option when the motion of the particles must be simulated as well as for the collisions with a flat wall (Di Renzo and Di Maio, 2004). If the stress profiles of the particles or boundaries are of interest, microscopic contact analysis will then be the best option (Di Renzo and Di Maio, 2005).

4.4.3 Particle Shape

In DEM modelling, the particle shape is one of the most important parameters to consider. It needs to be accurately captured in order to make accurate material flow predictions. Spherical particles are mostly preferred because of the efficiency with which contacts are detected, however, the only disadvantage is that the bulk (internal) friction is lower compared to the real granular material (Lu et al., 2015). Two ways of eliminating this flaw are by including contact rolling resistance/friction or modelling non-spherical particles. The inclusion of rolling friction applies a resisting moment to the particles, restricting its rotation. Using non-spherical particles have the same rotational resistance by increasing the particle-particle and particle-wall interlocking effect (Saint-Cyr et al., 2011). The particle rotation cannot be neglected since it affects dilation (volume change observed in granular materials when subjected to shear deformation) and the magnitude of the bulk shear strength.

Zhou et al. (2013) compared the use of 2D disc particles with rolling friction versus non-spherical particles without rolling friction. They managed to show that there is an increase in shear strength and dilatancy for both of these methods. However, it was evident that the disc particles with rolling friction could not produce the same level of accuracy as the non-spherical particles. Wensrich and Katterfeld (2012) also proved that the particle shape effects exceed the other effects significantly in practical applications. A drawback in using rolling friction to compensate for particle shape effects is the selection of the parameter value. There is no other way as to *tune* the rolling friction until a realistic bulk material behaviour is obtained.

Non-spherical particles include superquadrics, ellipsoids, clumps and polyhedrons. The most simple non-spherical particle shapes used by researchers are clumps and ellipsoids (Coetzee, 2017). Examples of the four different shapes are shown in Figure 5. The ellipsoid particle is a good representation of granular materials such as wheat and rice. A wide range of particle shapes can be obtained by using superquadrics (Hastie, 2010). It generates particles with smooth surfaces, however, is limited to only symmetric shapes. Therefore, it would be difficult to generate natural granular materials using superquadrics. Polyhedrons can be used to simulate particles with sharp edges and flat surfaces. The disadvantage of polyhedrons is the increase in the number of contacts and hence increasing the computational time. The use of flat surfaces for modelling round and smooth particles can lead to large inaccuracies since more contacts have been made compared to the real material behaviour.

Clumps consist of a collection of particles. By adding two or more spherical particles together, a rigid non-spherical particle model can be generated. The particles can also overlap each other to produce different shapes and sizes. Regardless of the forces exerted on the clumps, the clumps cannot break up (Coetzee, 2017). The advantage of using clumps is that the same level of efficiency for contact detection is obtained as for using spherical particles. However, the disadvantage is the lack of knowledge of the number and relative position of the spherical particles to be used in order to accurately approximate the real particle shape (Kacianauskas and Markauskas, 2011).

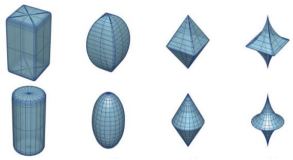

(a) Superquadrics (Portal et al., 2010).

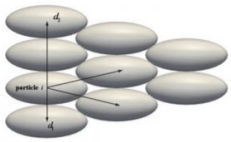

(b) Ellipsoids (Zhou et al., 2013).

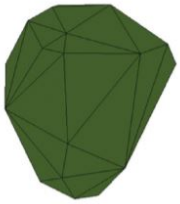

(c) Polyhedrons (Ji et al., 2016).

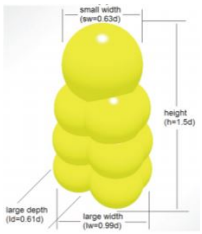

(d) Clumps (Mousaviraad et al., 2016).

Figure 5: Particle shapes available in DEM.

4.5 Particle Scaling

The use of a large number of particles and relatively small-sized particles make it inefficient to use DEM for industry scale applications since these factors have a significant influence on computation time. To overcome these problems, the particles are usually scaled and the particle size is therefore increased to reduce the total number of particles in the model. According to literature, scaling the particles influences the results, but to a certain extent, depending on the scaling factor and the specific application.

Coetzee (2019) showed that the particles (corn grains) could be scaled up by a factor of 4 in a large rotating drum without any significant effects on the dynamic angle of repose. For scaling factors larger than 4, inconsistent results were obtained. Grima and Wypych (2010b) analysed the material flow on a conveyor belt and the impact force caused by the discharge material on an impact plate. The results were relatively accurate for particles scaled up by 23 %, but for scaling factors of 2 to 3, inaccurate results were obtained. Xie et al. (2016) analysed the wear in a transfer chute and the results were accurate for scaling factors up to 2, obtaining a realistic material flow stream. However, larger scaling factors, resulted in particles diverging from the mean flow stream.

There are different approaches to scale the particle size, i.e. exact-scaling, coarse-graining and scalping. The method of exact-scaling is defined where the particle size and geometry are both scaled by the same factor. As a result, the total number of particles in the model remains the same, Figure 6a (Roessler, 2017). The second method known as coarse-graining is defined where the particles are scaled while the geometry stays the same. The number of particles in the model is decreased for this method, (see Figure 6b). The use of coarse-graining depends on the application, geometry and also the required output parameters, i.e. the

flow, forces, wear etc. The problem with this method is that it is not possible to use the mechanical properties of the small particles for the coarse particles since the number of contacts decreases. As a result, the material properties should be adjusted by repeating the calibration tests for the scaled particles (Roessler, 2017). The last method, scalping, is mostly used when a large particle size distribution is present. The smaller particles are scaled to fit the rest of the particle sizes or totally ignored (removed from the model) while the geometry stays the same. A good estimate for the scaled particle size should be between 0.8 $d_{\max}$ and $d_{\max}$, according to DIN-ISO 3435 (1979). This method also introduces a reduction in the number of particles since the domain is the same after the particles were scaled, Figure 6c (Roessler, 2017).

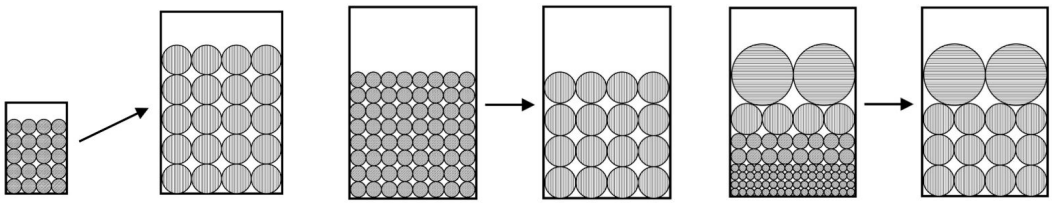

(a) Exact-scaling. (b) Coarse-graining. (c) Scalping.

Figure 6: Scaling methods (Roessler, 2017).

5 Belt Conveyor Test Facility

The belt conveyor test facility is situated in the Granular Materials Research Group (GMRG) laboratory in the Mechanical and Mechatronic Engineering building of the University of Stellenbosch. The facility and conveyor system was used for numerous undergraduate and postgraduate projects. The conveyor system consists of three conveyor belts inclined at 23°, two 2.2 kW and one 1.5 kW AC motor, a large and small hopper, three feeders, two transfer hoods, two rock boxes, a chute, an impact plate and a control unit. The whole belt conveyor test facility is shown in Figure 7. The facility also has high-speed cameras placed around the conveyor system which were used for particle image velocimetry (PIV). The key features of this facility are that the belt speed of all three conveyors are controlled using a programmable logic controller (PLC), the total conveyed mass is controlled by hand controlled valves, live mass flow rate readings of conveyor 1 and 3 are visible during testing and slow-motion videos of the material flow are captured for post-analysis. The mass flow rate of conveyor 1 and 3 was determined using two different load cell configurations which are further reported in Appendix A.1, and the calibration of the conveyor speed is reported in Appendix A.2.

The material circulation starts at the large hopper (see Figure 7). When the hand-controlled valve is opened, the material discharges onto conveyor 1 while the

material stream is being controlled by a feeder to avoid spillage at the loading-zone. The feeder also has adjustable side skirts to contribute to the controlled flow of conveyor 1. The pulley-to-pulley distance of conveyor 1 is 6 m in length. At the head pulley of conveyor 1, the material discharges into a transfer chute. This transfer chute can be adjusted between the options of a transfer hood, an impact plate or a rock box. After the material is redirected down the chute, it loads onto conveyor 2, while being controlled by another feeder. Conveyor 2 is the shortest conveyor belt in the system, having a pulley-to-pulley distance of 3.5 m. At the head pulley of conveyor 2, the material discharges in another rock box and then loads onto conveyor 3. Conveyor 3 is the longest conveyor belt, having a length of 6.5 m between the two head pulleys. The material discharges from conveyor 3 via a transfer hood and finally free-falls back into the large hopper.

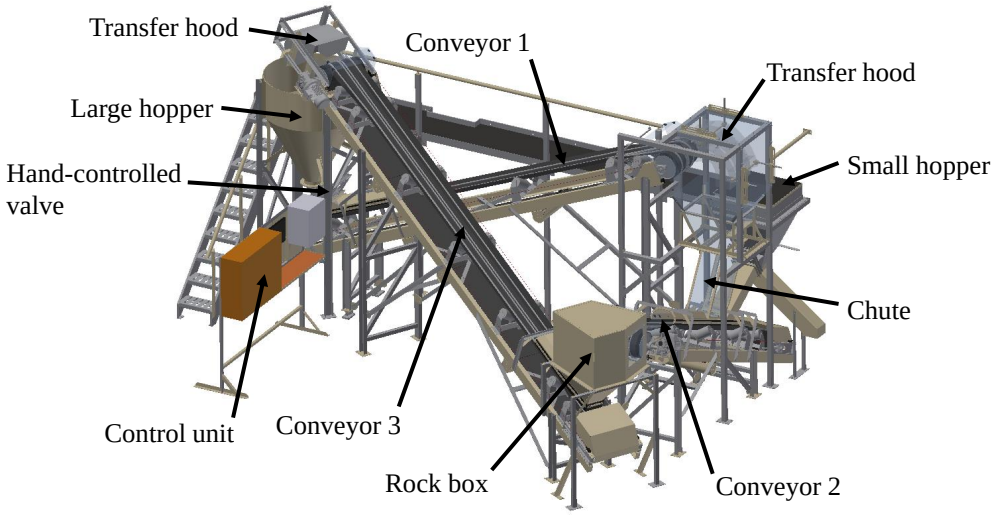

Figure 7: Belt conveyor test facility (CAD model).

5.1 Conveyor Belt

Since the belts were inclined, a chevron pattern was used to prevent the bulk material from sliding and rolling backwards and to provide more control over the mass flow rate, especially at higher belt speeds. The chevron pattern has a V-type shape (see Figure 8a) with the distance between successive patterns 330 mm and the "V" having a width of 255 mm, and the bottom opening a width of 20 mm. The total belt width is 450 mm.

The conveyor belts are supported with idler roller sets with a 30° troughing angle, Figure 8b. The idler rollers are spaced along the length of the belt, having the last set at 800 mm from the head pulley at both ends. Another set of idler rollers is placed near the last set to ensure that the material profile takes the correct shape before moving in the transition-zone. In the transition-zone, the material profile changes from a troughed belt profile to a semi-circle segment.

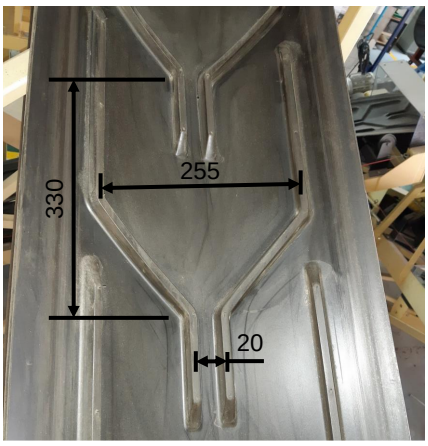

(a) Chevron pattern, dimensions in mm.

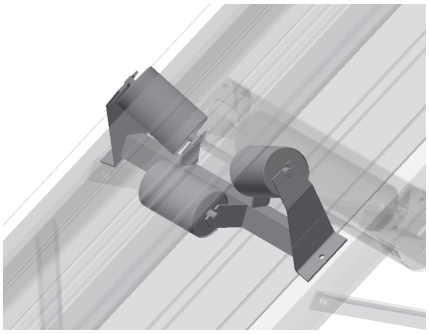

(b) Idler rollers (CAD model).

Figure 8: Conveyor belt.

5.2 Control Unit

The purpose of the control unit is to provide the user control over the three conveyors, activation of the safety switches, live data measurements as well as storing of the data. The main component is the Siemens S7-1200 PLC controller which has a 1214C DC/DC/DC CPU. All the hardware components are connected to this controller for the automation of the conveyor system's functionality.

The graphical control panel is shown in Figure 9. The main buttons are the start, stop, emergency stop and camera trigger button. A trigger cable is directly connected to the PLC and when the trigger button is pressed, the PLC sends a voltage spike which triggers the camera and starts the recording of the video. The setup and configuration of the high-speed camera are further reported in Appendix A.3. The user can vary all three belt speeds between 0 m/s and 5 m/s using the graphical analogue sliders and live readings of the mass flow rate is also shown.

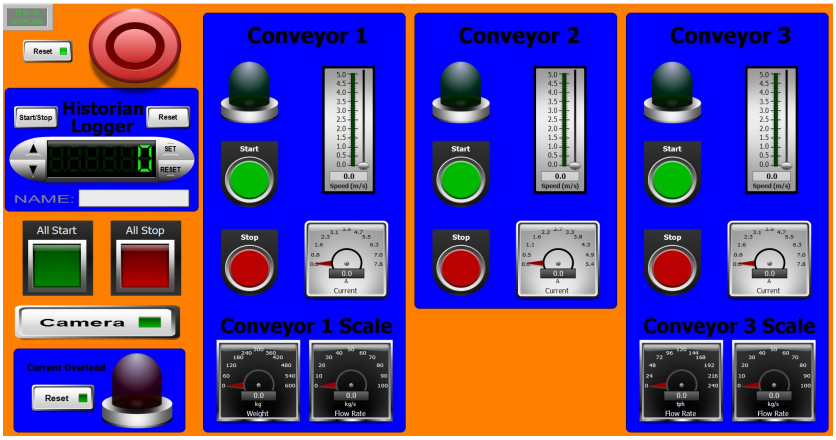

Figure 9: Graphical control panel.

5.3 Impact Plate Design and Experimental Setup

An impact plate was originally designed by Oosthuizen (2018), but it was found that the design lacked accuracy when measuring the reaction forces, especially in the shear direction. This was due to excessive friction between the components of the assembly as well as the design being too heavy. The redesign of the impact plate is shown in Figure 10, and consists of two main assemblies with one fixed to the transfer chute (Figure 10a) and the other free to move (Figure 10b), as well as two load cells to measure the impact force in two directions. The moveable assembly has two degrees-of-freedom, one perpendicular to the impact plate and the other tangential, provided by two sets of linear bearings.

The impact plate is an aluminium 6082 T6 sheet metal with polycarbonate panels mounted on both sides to ensure clear visibility of the material flow. Two precision rods were mounted onto the aluminium plate and aligned by four linear bearings. The linear bearings ensured that the forces exerted on the impact plate were successfully transferred to the load cell, by minimising the frictional losses. The normal load cell (S2M 500 N HBM) was placed in the centre of the aluminium plate. The same principle was utilised for measuring the shear force where the load cell (S2M 200 N HBM) was mounted between the fixed assembly and the moveable assembly. The moveable assembly was free to move vertically using two precision rods which were guided by another set of four linear bearings. The angle of the impact plate can be varied between 0° and 45° by sliding between the slots of the tilting bracket.

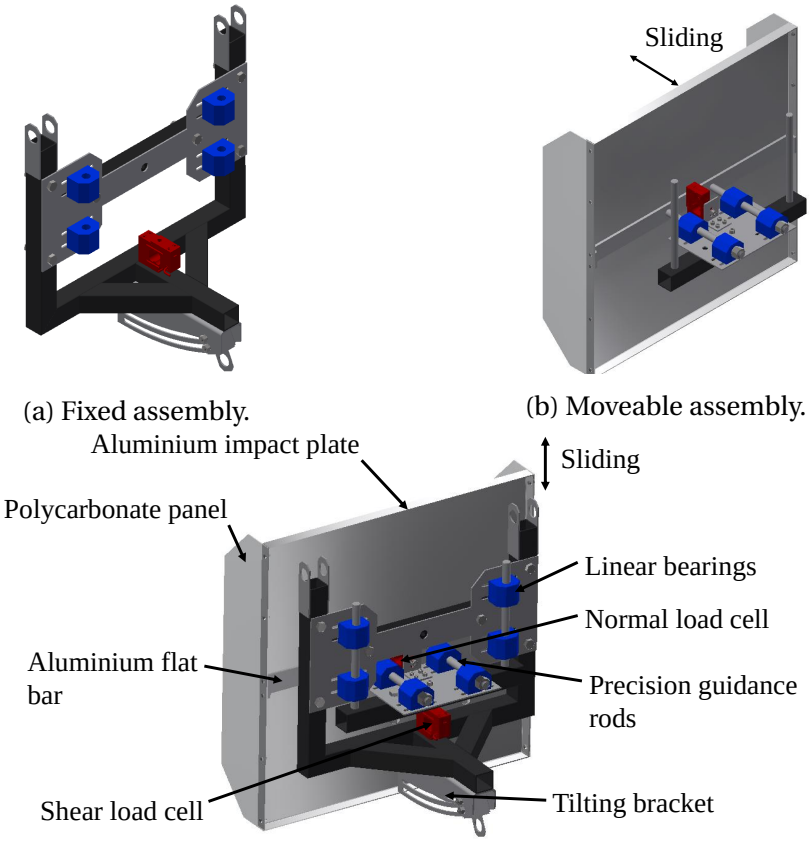

(a) Fixed assembly.

(b) Moveable assembly.

(c) Full assembly.

Figure 10: Impact plate design and assembly (CAD model).

A HBM Quantum X MX840B data acquisition system with Catman Easy (2018) software was used to record the load cell data. The calibration of load cells is an essential step for accurate measurements. A preferred guideline to follow for load cell calibration is to calibrate the load cell in a similar or same setup as in the experimental tests. The calibration procedure of the load cells is further reported in Appendix A.4.

An important characteristic to capture was the force frequency content or "spike" due to the chevron pattern. It was further used as a validation whether DEM could predict these "spikes". The experimental tests were conducted for belt speeds of 3 m/s and 4 m/s. Using the distance between successive patterns (see Figure 8a), the highest frequency (4 m/s) was expected to be,

$$f = \frac{1}{T} = \frac{1}{\frac{0.33}{4}} = 12.12 \text{ Hz} \tag{5–38}$$

The sampling frequency was therefore set to 500 Hz to ensure that the frequency content was adequately captured. The highest frequency (Nyquist frequency) which can be captured at this sampling rate was 250 Hz.

6 Material Characterisation

Corn grains were used as the bulk material for all the conveyor analyses. The reasons therefore were the relatively irregular shape and size of the particles and ease to experiment with. The material properties that could be measured are presented, followed by a DEM calibration process to obtain a final set of parameter values for spherical and non-spherical particles respectively.

6.1 Measured Properties

6.1.1 Equivalent Volume Diameter

The equivalent volume diameter D_{ev} of the corn grains was determined by scanning the grains with a 3D laser scanner and measuring the volume of the meshed STL models. Using a sphere's volume equation, the calculated diameter varied between 7.5 mm and 9.6 mm.

6.1.2 Damping

A drop test was utilised to determine the coefficient of restitution (COR) between corn grains and the identified surface materials on the conveyor system, i.e. aluminium and polycarbonate. After the COR was measured, the following relation was used to determine the particle-wall critical damping ratio's ζ_{pw} (Itasca, 2019),

$$\text{COR} = \exp \frac{-\zeta_{\text{pw}}\,\pi}{\sqrt{1-\zeta_{\text{pw}}^2}} \tag{6–39}$$

A number (10) of corn particles were dropped onto the surface material and the initial (V_1) and after impact (V_2) velocities were measured using a Olympus i-Speed 3 high-speed camera and post-processing software, Tracker (2020). According to Hastie (2013), it is difficult to determine the coefficient of restitution of non-spherical particles since the impact angle and rotation after impact should also be taken into account. Therefore, only tests where the particle rebound vertically was considered and the tests were repeated for different starting heights. The average coefficients of restitution and contact damping ratio's ζ_{pw} are summarised in Table 1. The results showed that there were no significant difference between the particle-wall damping of aluminium and polycarbonate. Wang et al. (2018) measured the COR of corn grains on a zincified plate to be between 0.635 and 0.613 which also agrees very well to the results on the aluminium and polycarbonate surfaces. Furthermore, it was assumed that the particle-particle damping ζ_{pp} is the same as the particle-wall damping, i.e. $\zeta_{\text{pp}} = \zeta_{\text{pw}}$ (Coetzee, 2019).

Table 1: Measured contact damping from the drop tests.

	COR	ζ_{pw}	Std Dev
Corn - Aluminium	0.64	0.14	0.03
Corn - Polycarbonate	0.66	0.13	0.04

6.1.3 Particle-Wall Friction

The particle-wall sliding friction μ_{pw} between corn grains and the surface materials of the conveyor system (aluminium, P40 sandpaper, polycarbonate and rubber) were measured using four methods. There is a distinction between static and dynamic friction with static friction occurring at the point of slip and dynamic friction caused by the continuous friction occurring during the relative translation between two bodies in contact. The four methods can be divided into two groups which yield two different experimental setups. The first setup is an inclined tester, depicted in Figure 11a. Individual (method 1) and a cluster (method 2) of corn grains were placed on an inclined plane where the plane was tilted until slippage started to occur. The plane's inclination angle was gradually increased ($\pm$ 0.1°/s) using a DC motor to rotate a threaded rod where a moment arm was connected between the threaded rod and the plane. At the point when the corn grains started to slip, the inclination angle was measured using a digital protractor. The cluster of corn grains was implemented by glueing the corn grains to a wooden board. For method 1 and 2, only the static friction could be measured.

The second set of experimental test setups for methods 3 and 4 are depicted in Figures 11b and 11c, respectively. The principle of these methods was based on the measurement of the shear force between the corn grains and a translated surface material while applying a known normal load to the grains. The translation was achieved by placing the test material on a rotating surface which could rotate at speeds between 1 rpm and 5 rpm resulting in shear velocities of 10.5 mm/s to 52.4 mm/s. The shear force was measured using an S2M 50 N HBM load cell and the calibration is further discussed in Appendix A.5. The third (3) method consisted of a rod with a hook connected to a plate sample with glued-on corn grains. Method 4 was very similar to method 3; however, it included an aluminium cylinder (70 mm diameter) with loose poured corn grains inside to a height of approximately twice the size of the corn grains. An aluminium lid was placed on top of the grains (inside the cylinder) and known weights added to increase the normal load. A Teflon sheet (2 mm thick) was glued underneath the cylinder to minimise the friction between it and the test material. The friction force between the empty cylinder and test material was measured as 0.14 N and considered insignificant compared to the corn-material friction force. The static and dynamic friction coefficients were obtained using methods 3 and 4.

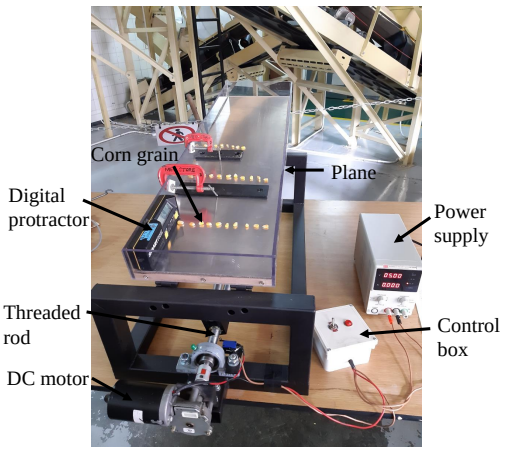

(a) Inclined tester test (methods 1 and 2).

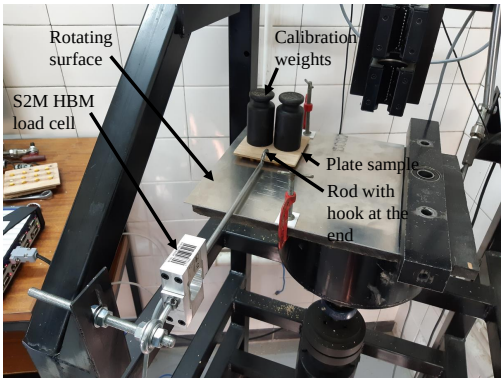

(b) Rotating surface test with plate samples (method 3).

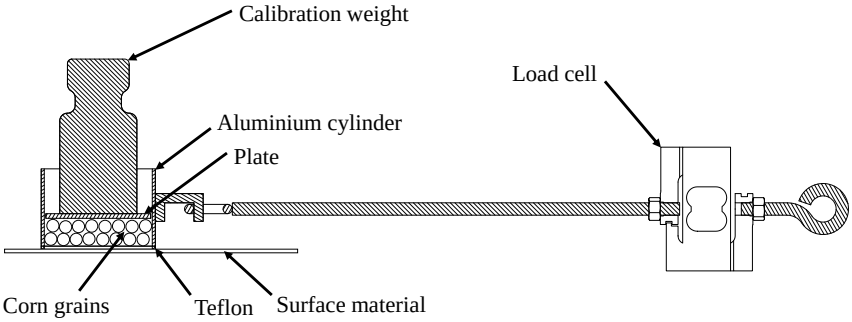

(c) Schematic drawing of cylindrical container test (method 4).

Figure 11: Particle-wall friction test setups.

The measured particle-wall friction coefficients μ_{pw} for the four methods are summarised in Table 2. For the aluminium surface, the inclined tester measured a $\mu_{s,\,pw}$ of 0.34 with a standard deviation of 0.06 and a $\mu_{s,\,pw}$ of 0.29 with a standard deviation of 0.05 for the single grain and plate sample tests, respectively. These results showed a relatively good correlation between the two methods. However, there was a large discrepancy in the results between the two inclined tester methods for the P40 sandpaper surface, i.e. 0.47 for the single grain and 0.72 for the plate sample. According to Feynman et al. (1963), the extent of friction between two materials does not depend on the type of material, eg. steel-on-steel, but rather the degree of smoothness and hardness of the surface. Moreover, the friction is defined by the impurities between the two materials, clinging to each other. With regards to the findings of Feynman et al. (1963), for the single grain tests, the friction was induced due to the cavities of the corn grains. However, the friction for the plate samples was induced merely because of the surface contact. By glueing the particles side-by-side, the cavities of the corn grains did not come in contact with the surface material, but only at single locations on each corn grain. As a result, the single grain tests produced larger friction than the plate sample tests. However, different results were obtained with the P40 sandpaper surface. Compared to the aluminium surface, an increase in $\mu_{s,\,pw}$ was observed

for the single grain tests, but a greater increase was obtained by the plate sample tests. This was due to the larger surface contact between the corn grains and coarse P40 sandpaper, consequently having a greater effect than the impurities from the single grain tests.

An example of the shear force measured for the rotating surface tests is shown in Figure 12. It is clear that the shear force reached a peak directly after the surface started to rotate. This peak force was due to static friction, after which the force maintained a steady value due to the kinetic friction. Different rotation speeds and applied normal loads were considered, but no significant effects on the results were observed. Therefore, the rotation speed was set to 1 rpm and the applied load to 2 kg for no specific reason. The measured friction results for methods 3 and 4 showed that there was no significant difference between the measured static and dynamic friction (see Table 2). However, the cylindrical container tests (method 4) measured a slightly larger friction value, $\mu_{pw} = 0.24$, compared to the plate sample tests (method 3), $\mu_{pw} = 0.20$. This could be due to the larger surface contact as well as the interactions between the individual corn grains. Unfortunately, it was not possible to measure the friction on the P40 sandpaper using the cylindrical container tests due to the large friction forces. However, the plate sample tests for the rotating surface (method 3) measured a static and dynamic friction of 0.65 and 0.61, respectively.

In conclusion, the measured friction varied significantly for the various methods; therefore, further research should be done on how to successfully determine the friction of non-spherical particles. However, the results obtained were merely used as a reference point. All four methods were not repeated for the polycarbonate and rubber materials since large deviations were found. Thus, only the plate sample tests for the inclined tester were used, where a μ_{pw} of 0.26 was measured with a standard deviation of 0.05 for the polycarbonate surface. For the rubber surface, plane angles greater than 45° were found. Therefore, it was assumed that the friction coefficient for rubber surfaces is 1.

Table 2: Summary of the measured particle-wall friction coefficients μ_{pw} for the four methods.

Material	**Friction type**	**Inclined tester**				**Rotating surface**			
		Single grain (1)		**Plate samples (2)**		**Plate samples (3)**		**Cylindrical container (4)**	
		Mean	**Std Dev**	**Mean**	**Std Dev**	**Mean**	**Std Dev**	**Mean**	**Std Dev**
Aluminium	Static, $\mu_{s,\,pw}$	0.34	0.06	0.29	0.05	0.20	0.04	0.24	0.05
	Dynamic, $\mu_{k,\,pw}$	-	-	-	-	0.20	0.04	0.24	0.04
P40 sandpaper	Static, $\mu_{s,\,pw}$	0.47	0.09	0.72	0.12	0.65	0.13	-	-
	Dynamic, $\mu_{k,\,pw}$	-	-	-	-	0.61	0.04	-	-

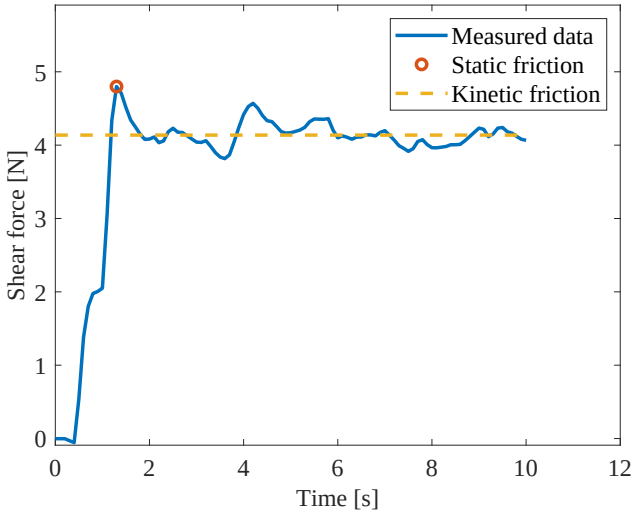

Figure 12: Shear force example for rotating surface friction test.

6.1.4 Bulk Density

The bulk density ρ_b was determined by loosely pouring corn grains into a glass cylinder and measuring the mass and fill height of the particles. Knowing the cross-sectional area of the cylinder, the volume of the packed corn grains was determined, and so, by dividing the mass of the material by its volume, $\rho_b = m/V$, the bulk density was obtained. The test was repeated five times to obtain an average bulk density of 824.73 kg/m^3. Similar values were found by Coetzee (2020) and González-Montellano et al. (2012), i.e. 810.0 kg/m^3 and 866.7 kg/m^3, respectively.

6.1.5 Particle Density

The particle density ρ_p was determined using a Borosilicate glass cylinder with a volume scale. A known mass of corn grains was poured into a known volume of water. Measuring the change in volume of the displaced water using the (1) indicated volume markings and (2) measuring the change in height with a vernier calliper, the particle density was determined for both methods by dividing the particles' mass by the water's change in volume, $\rho_p = m/\Delta V$. The average particle density for the measured height and the volume strategies was 1212.84 kg/m^3 and 1249.95 kg/m^3, respectively. The average between these methods was determined as 1231.39 kg/m^3. Coetzee (2020) and González-Montellano et al. (2012) reported similar values for the particle density of corn grains, i.e. 1245.9 kg/m^3 and 1163.3 kg/m^3, respectively.

6.2 DEM Calibration

6.2.1 Particle Shape Model

The Granular Materials Research Group has done extensive research on the modelling and calibration of corn grains. The most efficient particle shape model consists of spheres because of its efficient contact detection algorithms. Furthermore, corn grains have several different shapes and sizes, making it difficult to obtain accurate simulation results when using a single corn grain shape model. Therefore, four corn grains were randomly selected and scanned with a 3D laser scanner (Figure 13a). The stereolithographic (STL) models were then imported into ASG3D software (www.cogency.co.za) which was used to fit 3 (Figure 13b), 5 (Figure 13c) and 10 (Figure 13d) spheres to the STL models in an optimised manner. Thus, creating the 3-, 5- and 10-clump particle shape models. The largest emphasis throughout the DEM analyses was on the simulation of the 3-clump particles, where the 5- and 10-clump particles were investigated to a lesser extent since these models consist of more spheres, increasing the computation time. Spherical balls were also used because of the reduced computing time needed to simulate. However, while the clumps could provide accurate results using sliding friction only, the spherical balls had to be modelled with the inclusion of sliding and rolling friction to account for the non-spherical shape of the physical particles. The balls were created in PFC3D (2019) having a diameter equal to the equivalent volume diameter of the corn grains presented in Section 6.1.1.

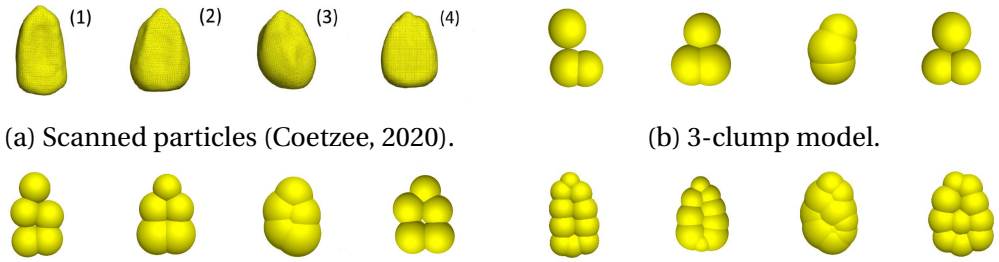

(a) Scanned particles (Coetzee, 2020).

(b) 3-clump model.

(c) 5-clump model.

(d) 10-clump model.

Figure 13: Particle shape models of four selected corn grains (the spherical ball model is not shown).

6.2.2 Calibration of Particle Density For Scaling

The scaling method of coarse-graining was used throughout the study, i.e. only the particles were scaled. The size (radius) of the particles was scaled, decreasing the total number of particles in the model while the geometry and domain stayed the same. By scaling the radius, the volume of the particles increased to the power of 3. An important aspect to investigate was the effect of particle scaling on the bulk density; otherwise, the mass flow rate through the conveyor system would not be accurately modelled.

The calibration method was based on an iterative approach by setting a target bulk density and iterating the particle density until a 1 % error was obtained. A cylindrical container was filled with particles (3-clump) and the particles allowed to reach a state of static equilibrium. The initial particle density was set to the measured value (Section 6.1.5). An iterative approach was then utilised by calculating the bulk density of the particles in the cylinder. If the error between the target bulk density and the calculated bulk density was larger than 1 %, a new particle density $\rho_{\text{p, new}}$ was assigned to the particles and left to settle again. According to Coetzee and Els (2009), there is a linear relationship between the particle and bulk density. The updated particle density $\rho_{\text{p, new}}$ was therefore determined by multiplying the previous particle density $\rho_{\text{p, previous}}$ by the ratio of the target bulk density $\rho_{\text{b, target}}$ and the calculated bulk density $\rho_{\text{b, previous}}$,

$$\rho_{\text{p, new}} = \rho_{\text{p, previous}} \times \frac{\rho_{\text{b, target}}}{\rho_{\text{b, previous}}} \tag{6–40}$$

The particle density was continuously updated until convergence of $\rho_{\text{p, new}}$ was reached. This calibration process was based on exact-scaling, where both the particles and geometry were scaled. Coarse-graining was not possible since it would have provided unrealistic results when the particles did not fit in the container. The DEM parameters used for the density calibration are shown in Table 3.

Table 3: Particle density calibration DEM parameters.

Parameter	**Value**	**Unit**
$\rho_{\text{b, target}}$	824.73	kg/m^3
$\rho_{\text{p, initial}}$	1231.39	kg/m^3
k_{pp}	100	kN/m
k_{pw}	200	kN/m
μ_{pp}	0.15	-
μ_{pw}	0.55	-
ζ_{pp}	0.5	-
ζ_{pw}	0.5	-

The calibration was done for scaling factors up to 8. The results showed that for a 1:1 scale factor, the calibrated particle density was $\rho_{\text{p}} = 1366.63$ kg/m^3 in order to accurately model the bulk density of $\rho_{\text{b}} = 824.73$ kg/m^3. This particle density is slightly higher than the measured density of 1231.39 kg/m^3. This difference can be attributed to the difference in shape of the physical and modelled particles. Using a scale factor of 8, the calibrated particle density decreased slightly to a value of 1273.80 kg/m^3. This decrease could be attributed to an increase in particle overlap due to the increase in bed height. However, in all subsequent models, a particle density of $\rho_{\text{p}} = 1366.63$ kg/m^3 was used for all particle scales.

6.2.3 Calibration of Sliding - and Rolling Friction

Coetzee (2020) used the exact same corn grains and implemented a draw down test to obtain a feasible region for parameters μ_{pp} and $\mu_{\mathrm{r\,pp}}$ that would satisfy four bulk measures, i.e. shear angle, mass flow rate, mass discharged and angle of repose. The draw down test was simulated for spherical particles (balls) and clumps (3-subspheres). Only a single feasible region was found for the ball particles (see Figure 14a). However, two were found for the 3-clump particles, i.e. a large region at a low μ_{pp} and high $\mu_{\mathrm{r\,pp}}$ and a very small region region at $\mu_{\mathrm{pp}} = 0.17$ and $\mu_{\mathrm{r\,pp}} = 0$ (see Figure 14b). Coetzee (2020) further found that the draw down test results were insensitive to contact stiffness. However, the same results were not found for the ring shear tests since the material was more confined during the test. The bulk friction angle was successfully predicted for a $\mu_{\mathrm{pp}} = 0.15$ from the ring shear tests. From these findings by Coetzee (2020), as a starting point, the spherical particles inter-particle sliding μ_{pp} and rolling friction $\mu_{\mathrm{r\,pp}}$ were taken as 0.20 and 0.125, respectively, which was in the centre of the feasible region in Figure 14a. As for the clumps (3-, 5- and 10-clump models), the particle sliding friction μ_{pp} was set to 0.15 and particle rolling friction $\mu_{\mathrm{r\,pp}}$ to 0. More combinations of the friction parameters were further investigated in various section as indicated in Table 4.

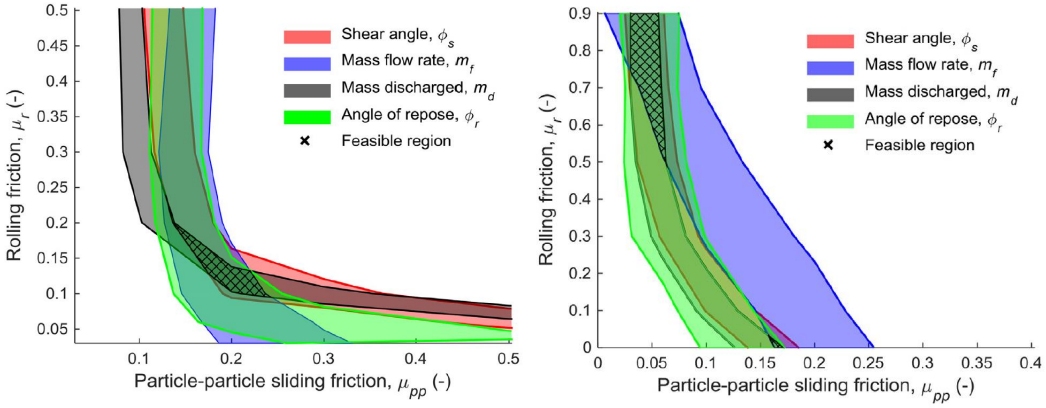

(a) Ball particle with $k_{\mathrm{pp}} = 20$ kN/m.

(b) 3-clump with $k_{\mathrm{pp}} = 10$ kN/m.

Figure 14: Isolines to define a feasible region from draw down tests (Coetzee, 2020).

The particle-wall sliding friction for aluminium, P40 sandpaper and polycarbonate was measured in Section 6.1.3. However, a sensitivity study was performed by varying μ_{pw} to quantify the model sensitivity to this parameter. The related sections for the sensitivity studies are indicated in Table 4.

6.2.4 Stiffness Calibration

Coetzee (2020) conducted calibration tests to determine a combination of μ_{pp} and $\mu_{\mathrm{r\,pp}}$ for spherical particles and clumps using the ring shear and draw down

tests. It was found that the contact stiffness in the ring shear test could be scaled down by a factor of 10 (with full stiffness at 100 kN/m), but for the draw down test, the results were insensitive to the contact stiffness. A low contact particle stiffness of 1 kN/m was used by Coetzee (2020) to reduce computational time. The critical timestep is proportional to the square root of the particle mass divided by the stiffness,

$$t_{\text{crit}} = \sqrt{\frac{m}{k}} \tag{6–41}$$

Hence, larger contact stiffness or lower particle mass (smaller particles) will decrease the timestep and as a result, increase the number of cycles to be completed. Lowering the contact stiffness is a method often employed by researchers (Gröger and Katterfeld, 2006), yet for certain applications the model can be very sensitive to the contact stiffness.

It is difficult to measure the k_{pp} because of corn grains irregular shape and small size. In this study, a value of $k_{\text{pp}} = 1$ kN/m was used based on the findings of Coetzee (2020) for the exact same corn grains. The contact stiffness between the particles and walls, k_{pw}, was taken as 2 kN/m, hence, $k_{\text{pp}} = 1$ kN/m. A low stiffness was appropriate since there was relatively low levels of confining stress during the conveying of the material. However, the effect of contact stiffness was investigated for conveyor applications by examining whether an increase in stiffness would yield different results for the impact force on an impact plate (see Section 8.2.3.2).

6.3 Summary of Material Characteristics

A summary of the DEM parameters for the linear spring-dashpot (LSD) contact model is given in Table 4 with reference to the sections where the parameters were calibrated.

Table 4: Summary of DEM parameters for corn grains.

Parameter	Comment	Section(s)	Value	Unit
ρ_b	Bulk density	6.1.4 and 6.2.2	824.73	kg/m^3
ρ_p	Particle density	6.1.5 and 6.2.2	1366.63	kg/m^3
D_{ev}	Equivalent volume diameter upper limit	6.1.1	9.60	mm
	Equivalent volume diameter lower limit	6.1.1	7.50	mm
k_{pw}	Stiffness particle - aluminium	6.2.4 and 8.2.3.2	2* - 200	kN/m
	Stiffness particle - polycarbonate	6.2.4	2	kN/m
	Stiffness particle - rubber	6.2.4	1	kN/m
k_{pp}	Stiffness particle - particle	6.2.4 and 8.2.3.2	1* - 100	kN/m
ζ_{pw}	Damping particle - wall	6.1.2 and 8.2.3.1	0.05 - 0.14* - 1.00	N s/m
ζ_{pp}	Damping particle - particle	6.1.2, 8.2.3.1 and 10.2.1	0.05 - 0.14* - 0.50	N s/m
μ_{pw}	Sliding friction particle - aluminium	6.1.3 and 8.3.1	0.20 - 0.25* - 0.90	-
	Sliding friction particle - polycarbonate	6.1.3 and 9.3.1	0.20 - 0.26* - 0.35	-
	Sliding friction particle - rubber	6.1.3	1	-
	Sliding friction particle - P40 sandpaper	6.1.3 and 8.3.1	0.20 - 0.80* - 0.90	-
$\mu_{r\,pw}$	Rolling friction particle - rubber (balls)	8.2.5.2	0.00 - 0.10* - 0.90	-
μ_{pp}	Sliding friction particle - particle (clumps)	6.2.3, 8.2.3.3, 8.3.2.1 and 10.2.1	0.05 - 0.15* - 0.40	-
	Sliding friction particle - particle (balls)	6.2.3, 8.2.5.2, 8.3.3.2 and 10.2.3.1	0.15 - 0.25* - 0.70	-
$\mu_{r\,pp}$	Rolling friction particle - particle (balls)	6.2.3, 8.2.5.2, 8.3.3.2 and 10.2.3.1	0.125 - 0.50* - 0.80	-

*Calibrated value that delivered the most accurate simulation results.

7 Conveyor Belt Simulation in PFC3D

The simulation of the conveyor system, depicted in Figure 7, was conducted in PFC3D (2019). This entailed the generation of the geometries for the simulations, generating of the particles (Appendix B) and various methods to convey the material, obtaining a faster computing time while maintaining the necessary accuracy.

7.1 Conveyor Belt Geometry and Velocity Vectors

One of the limitations in PFC3D (2019) and most other commercial DEM software packages is the inability to model and assemble complex geometries. Only simple geometric shapes like, spheres, cylinders, cubes and prisms can be generated. Therefore, a CAD package, Inventor (2019) was used to model the conveyor system. Individual parts/geometries were generated in Inventor and assembled. By exporting the individual parts as a STL model and importing it into PFC3D, resulted in an assembled model in the DEM environment.

The belt profile had a significant effect on the mass flow rate; therefore, the belt shape was accurately measured with a vernier calliper. The belt had a troughed profile along its length, shaped by equally spaced idler rollers and flattened out from the last idler set to the head pulley (see Figure 15a). Furthermore, the movement of the chevron pattern had to be considered since it significantly affected the flow (see Section 7.2). PFC3D has the ability to simplify the simulation of a conveyor belt significantly, by avoiding the circulation of the belt, but rather assigning velocity vectors as boundary conditions to the surface of the stationary belt.

A geometry imported in PFC3D is known as a "wall" and consists of triangular "facets". The number of facets depends on the resolution of the geometry. Higher resolution provides more accurate geometry shapes but increases the number of facets, hence, increasing the computational time. A constant velocity vector can be assigned to a conveyor wall in PFC3D, but in this case, it would not be a very good representation of the problem at hand. The velocity vectors are not the same at every location on the belt, caused by the shape and curvatures of the belt. Therefore, each facet on the belt/wall should have an individually assigned velocity vector. This was implemented by defining the "conveyor vector" and "pulley axis" as shown in Figure 15a. The conveyor vector pointed from the centre of the tail pulley to the centre of the head pulley. Taking the cross product between a vector normal to the facet and the conveyor vector, defined a rotation vector for each individual facet (Figure 15b). The facet normal vector ($\vec{N_f}$) was then rotated around the rotation vector ($\vec{R_f}$) by $\pm$ 90°, using Rodrigues' rotation formula (Tomasi, 2013). This resulted in a vector $\vec{P_f}$ parallel to the face of the facet,

$$\begin{aligned}\vec{P_f} &= \vec{N_f}\cos(\pm 90^\circ) + (\vec{R_f} \times \vec{N_f})\sin(\pm 90^\circ) \\ &+ \vec{R_f}(\vec{R_f} \cdot \vec{N_f})(1-\cos(\pm 90^\circ))\end{aligned} \tag{7–42}$$

If the dominant global direction component of the rotation axis vector pointed in the same direction as the pulley axis, the rotation angle used in Rodrigues' rotation formula was negative 90°, otherwise, positive 90°. The rotated vector $\vec{P_f}$ defined the direction of the facet velocity in the global coordinate system. The last step was to multiply the conveyor speed with the unit vector $\vec{P_f}/||\vec{P_f}||$, resulting in the facet velocity vector. This was applied to all conveyor facets, including that of the head pulley.

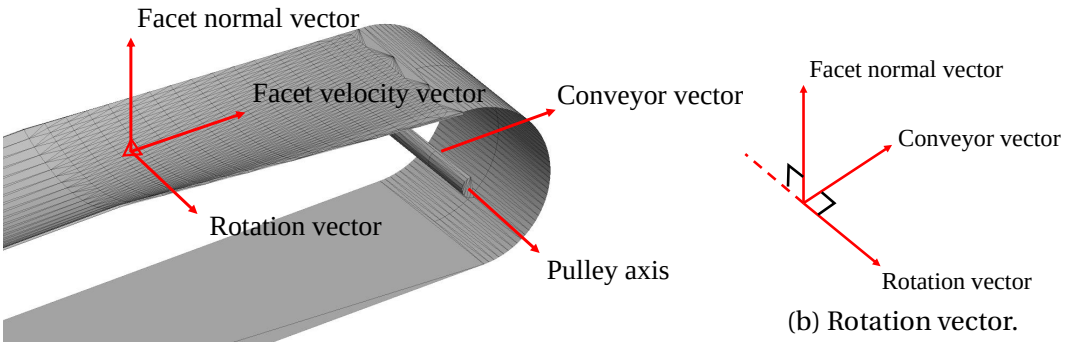

(a) Velocity vectors.

(b) Rotation vector.

Figure 15: Conveyor belt (a) velocity vectors and (b) cross product to determine the rotation vector.

7.2 The Chevron Pattern

No research has been done on whether the inclusion of chevron patterns in conveyor belt simulations will provide more accurate and realistic results. Most researchers use a combination of particle-wall sliding (μ_{pw}) and rolling friction ($\mu_{\mathrm{r\,pw}}$) for the particle-wall contacts to avoid the rolling back of the particles. The rolling of the particles will have a substantial influence on the mass flow, especially at low flow rates.

The implementation of the velocity boundary conditions could not be used for the chevron pattern, i.e. by keeping the geometry stationary and applying velocity vectors to the wall facets. The chevron pattern had to circulate the belt. The geometry of the chevron pattern was also created in Inventor (2019), however, as a solid body, and then sectioned into 10 pieces with an overlap between each piece. The overlap ensured that the successive pieces stayed in contact when the pattern circulated the head pulley, Figure 16a. To minimise computation time, a single pattern set was imported and located below the material loading zone. This pattern set was then duplicated at the same location, and each set released at the appropriate time during the simulation. The timestep for the release of the patterns was determined by measuring the distance between each set and dividing this distance by the conveyor set speed.

The patterns had to follow the curvature of the belt, and this was accomplished by "slaving" the pattern pieces to the belt facets. Each timestep, the belt facet closest to the centre of the pattern piece was found and the velocity vector of that facet, assigned to the pattern piece. In the transition-zone, the belt starts to flatten out towards the head pulley, and the pattern should therefore also open up, following the belt shape. The opening up of the pattern was accomplished by rotating each pattern piece around its global axes with a constant angular velocity. Knowing the starting position of each pattern piece and that each piece flattened out at the head pulley, individual rotation axes and velocities were determined and assigned to each pattern piece as it entered the transition-zone. This ensured that the whole pattern stayed in contact with the surface of the belt. There were a total of 239 facets in the transition-zone. As the pattern pieces reached the head pulley, a constant angular velocity was assigned to them. The overlapping of the pattern pieces ensured that there was no space between successive pieces when the pattern rotated around the head pulley (see Figure 16b). At a certain position around the head pulley, the pattern pieces were deleted since they had no more influence on the flow of material.

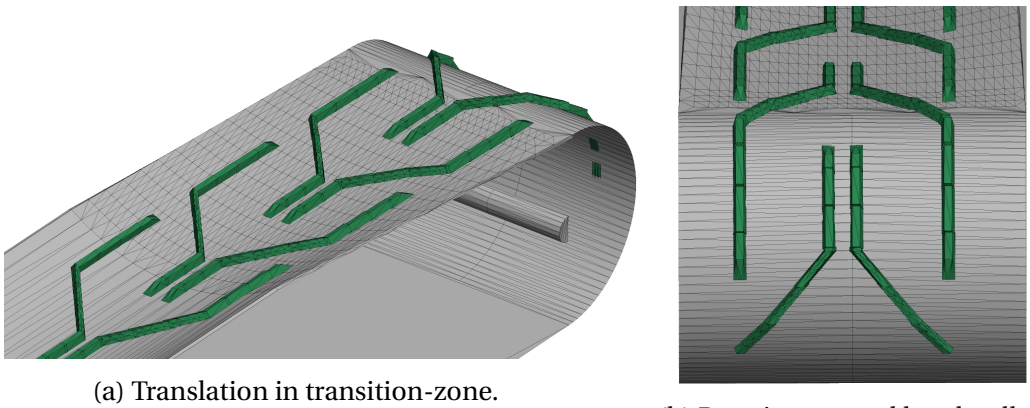

(a) Translation in transition-zone.

(b) Rotation around head pulley.

Figure 16: Chevron pattern (a) translation in the transition-zone and (b) rotation around the head pulley.

7.3 Effect of the Chevron Pattern on Material Flow

The movement of the chevron pattern was validated by evaluating the discharge velocity and trajectory of the material flow between the simulation with and without the pattern. The simulation for a mass flow rate of 4 kg/s with a belt speed of 3 m/s was used as the comparison measure. The generation and insertion process of the particles in all the simulations is reported in Appendix B. The particles' positions, velocities and accelerations were saved every 10 ms throughout the simulation and then analysed in Matlab (2018). Spatial and time averaging were applied to determine the discharge velocity after steady-state flow was reached. For spatial averaging, the trajectory stream was divided into five equal zones, and the average particle speed (velocity magnitude) calculated for each zone. Time averaging was done by averaging the average speed in each zone over the whole duration of the simulation (after steady-state). It is clear that there was a significant difference between the two trajectories where the pattern simulation had a much higher average discharge velocity (2.75 m/s) compared to flat belt simulation (2.45 m/s), Figure 17a. Furthermore, Figure 17b shows that the chevron pattern caused the material to discharge with a certain frequency. The results showed quite a large difference in the material flow for the two models and would have a significant influence on further investigations if the pattern was neglected.

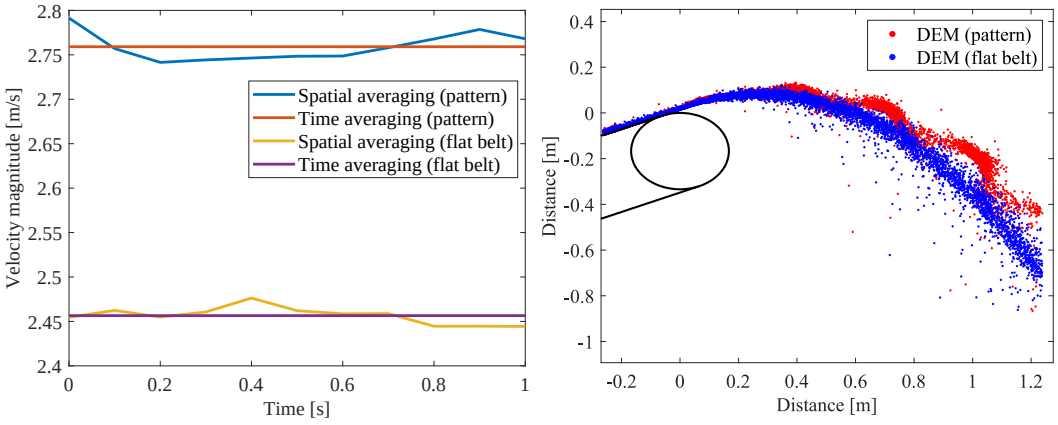

(a) Discharge velocity.

(b) Trajectory.

Figure 17: Material (a) discharge velocity and (b) trajectory comparison between the simulations with and without the pattern ($V_b = 3$ m/s and $\dot{m} = 4$ kg/s).

The reason why two distinct flow patterns were present, was caused by the piled-up material between the chevron patterns, preventing the material to roll back down the belt. The discharge velocity was therefore closer to the belt speed. However, the material between the pattern sets and at the bottom of the "V" (see Figure 8a) rolled back to some degree, and had a slightly lower velocity. As a result, a variation in the material velocity was observed along the trajectory stream. Further validation is done in Section 8.2.1, where the effect of the pattern on the reaction forces on an impact plate was investigated.

7.4 Alternative Simulation Model

It was found that the pattern simulation model was computationally much more expensive compared to the flat belt simulations. Therefore, alternative models were considered to decrease the computation time, but to still procure accurate material flow predictions. The discharge trajectory for the pattern simulations for a belt speed of 4 m/s and a mass flow rate of 4 kg/s, 8 kg/s and 12 kg/s were analysed in Matlab (2018). From the material trajectory stream, depicted in Figure 18a, it is clear that there was a variation in flow between the piled-up and free-stream (material with lower velocity) material. The velocities were then recorded for 5 frames at both of these positions at the point of discharge for the three mass flow rates. The results showed that the piled-up zone's velocity was, on average, approximately 1.075 times higher.

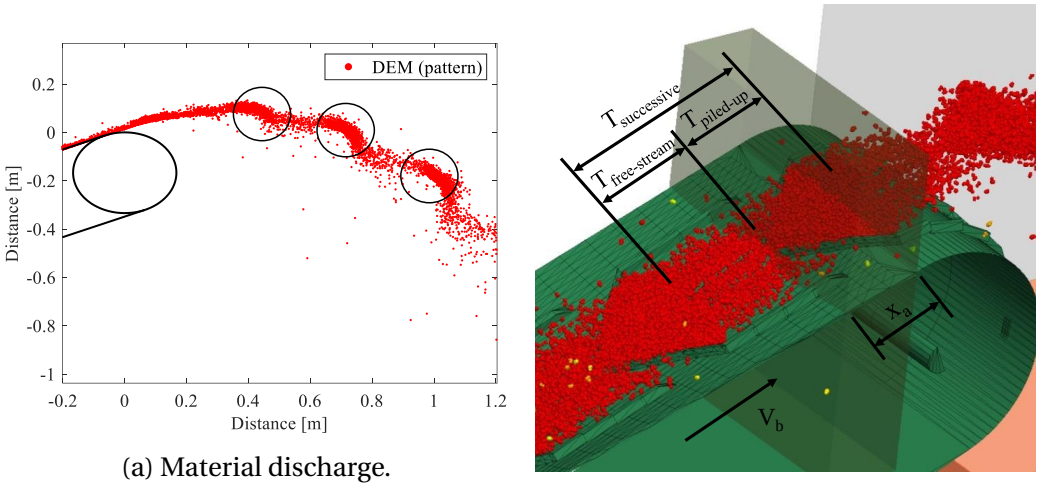

(a) Material discharge.

(b) Material on conveyor belt.

Figure 18: Variation between the piled-up and free-stream material ($V_b = 3$ m/s).

Two alternative simulation methods were considered, i.e. by applying rolling friction to the belt and accelerating the (1) facets or the (2) clumps at the point of discharge. These methods were based on the material in the piled-up region (Figure 18b) being accelerated (by a factor of 1.075) while the material in the free-stream region kept moving at the belt speed. This resulted in the necessary flow frequency between successive patterns. The acceleration zone (for the facets and clumps) is shown in Figure 18b, and the length of this zone was taken as the distance of the material in the piled-up region of the pattern. Knowing the acceleration length x_a and the belt speed V_b, the period of the successive accelerations was determined, $T_{\text{piled-up}} = x_a / V_b$, and that was subtracted from the period for successive patterns $T_{\text{successive}}$, to determine the period of the free-stream material $T_{\text{free-stream}}$.

For the first method, rolling friction was applied and the velocity vectors of the facets (conveyor boundary condition) in the discharge zone were increased by a factor of 1.075. In the second method, rolling friction was also applied, but the velocity of the clumps in the discharge zone was increased by a factor of 1.075. The rolling friction was increased until the necessary trajectory, average discharge velocity and impact force were obtained, and based on these results, a value of $\mu_{\text{r pw}} = 0.90$ was used in all subsequent models. The results for the discharge velocity and trajectory of the two methods are shown in Figure 19. There was a decrease in the discharge velocity with an increase in the mass flow, for both methods; however, the clump acceleration results correlated better with the pattern simulation model, and was used in all subsequent models where the chevron pattern or a smooth belt was not used. The accuracy of the model in predicting the impact frequency and force on a vertical impact plate was also investigated by comparing the results to the results of the pattern model. It was found that the clump acceleration model predicted the exact same impact fre-

quency and the accuracy in predicting the impact forces was within 5.33 %. Furthermore, the discharged mass flow rate of the two models was investigated and reported in Appendix C, and a comparison for the models computation time is reported in Appendix D.

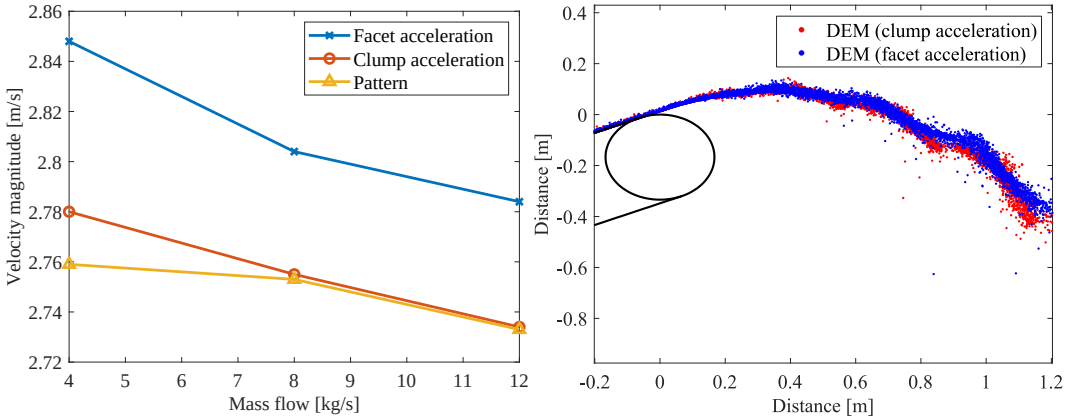

(a) Discharge velocity.

(b) Trajectory.

Figure 19: Material (a) discharge velocity and (b) trajectory comparison between the clump and facet acceleration simulation methods ($V_b = 3$ m/s).

8 Impact Plate Analysis

Research has shown that the analytical models available for predicting the bulk material flow onto an impact plate can provide reasonable approximations, but failed in certain areas for accurate material flow predictions (Grima, 2011). Using a DEM model, the forces exerted on an impact plate can be determined. A well established DEM model can then be used as a design tool to design impact plates with longer service life. This section presents a detailed comparison between the DEM and analytically predicted material flow and reaction forces on a vertical and angled impact plate and experimental measurements.

8.1 DEM Model of the Impact Plate

The DEM model used for the impact plate analysis is shown in Figure 20 with the directions of the normal R_n and shear R_s component of the reaction forces, and the location of the plate relative to the feeding conveyor's head pulley. The measuring of the reaction forces was conducted at a sampling frequency of 1000 Hz while the position, velocity and acceleration of each particle were sampled at a frequency of 10 Hz. The parameter values used are summarised in Table 4. The moving particles' velocities were defined according to a colour scheme, depicted in Figure 21. In other words, the particles displayed as red had the maximum velocity which was equal to the belt speed, and the dark blue particles were stationary having no velocity. Furthermore, the impact plate simulations were

conducted for a simulation time of 4 s. The validation of this time duration is reported in Appendix E.

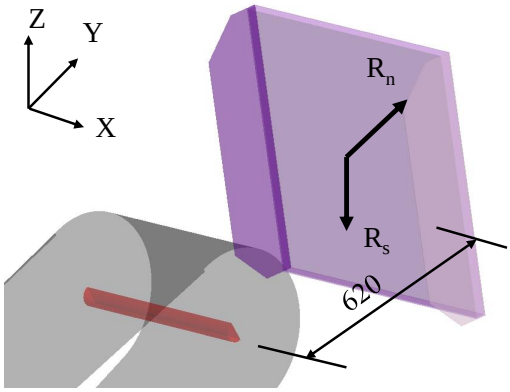

Figure 20: DEM model for impact plate analysis, dimensions in mm.

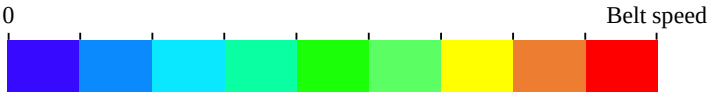

Figure 21: Colour bar indicating the particles' velocities.

8.2 Vertical Impact Plate Results and Discussion

The impact plate analysis was conducted for belt speeds of 3 m/s and 4 m/s with mass flow rates between 4 kg/s and 12 kg/s. To verify the accuracy of the DEM model, the results were compared to load cell measurements and high-speed video analyses. If the percentage error was larger than 10 %, it was assumed to be inaccurate and indicated by showing the result in red. It was found that the equation to determine the material impact angle from Korzen's analytical model (Section 4.2) was incorrect. The corrected model is reported in Appendix F and the parameters used are listed in Table 5.

Table 5: Summary of the impact plate analytical model parameters.

Parameter	Comment	Value	Unit
ρ_b	Bulk density	1366.63	kg/m^3
V_b	Belt speed	3 - 4	m/s
$\dot{m}$	Mass flow rate	4 - 12	kg/s
b_t	Belt thickness	7.20	mm
D_p	Pulley diameter	334	mm
S	Distance from head pulley to impact plate	620	mm
α_b	Belt inclination angle	23	°
β	Impact plate tilt angle	0	°
μ_w	Sliding friction particle - wall	0.25	-

8.2.1 Impact Frequency and Forces (3-Clump Model)

The time signal of the normal and shear force components predicted by DEM (pattern simulation model) for a belt speed of 3 m/s and a mass flow rate of 8 kg/s were compared to the measurements, Figure 22. DEM predicted significantly larger peaks (Figures 22b and 22d) compared to the measurements (Figures 22a and 22c). The measured peak was approximately 50 N and 5 N in the normal and shear directions, respectively, whereas DEM predicted values of approximately 70 N and 10 N, respectively. The reason for this is that the physical impact plate and supporting structures are elastic, resulting in a number of vibration models influencing the force measured by the load cells. On the other hand, the impact plate is considered absolutely rigid in the DEM model and the predicted force purely due to the particle-plate collisions.

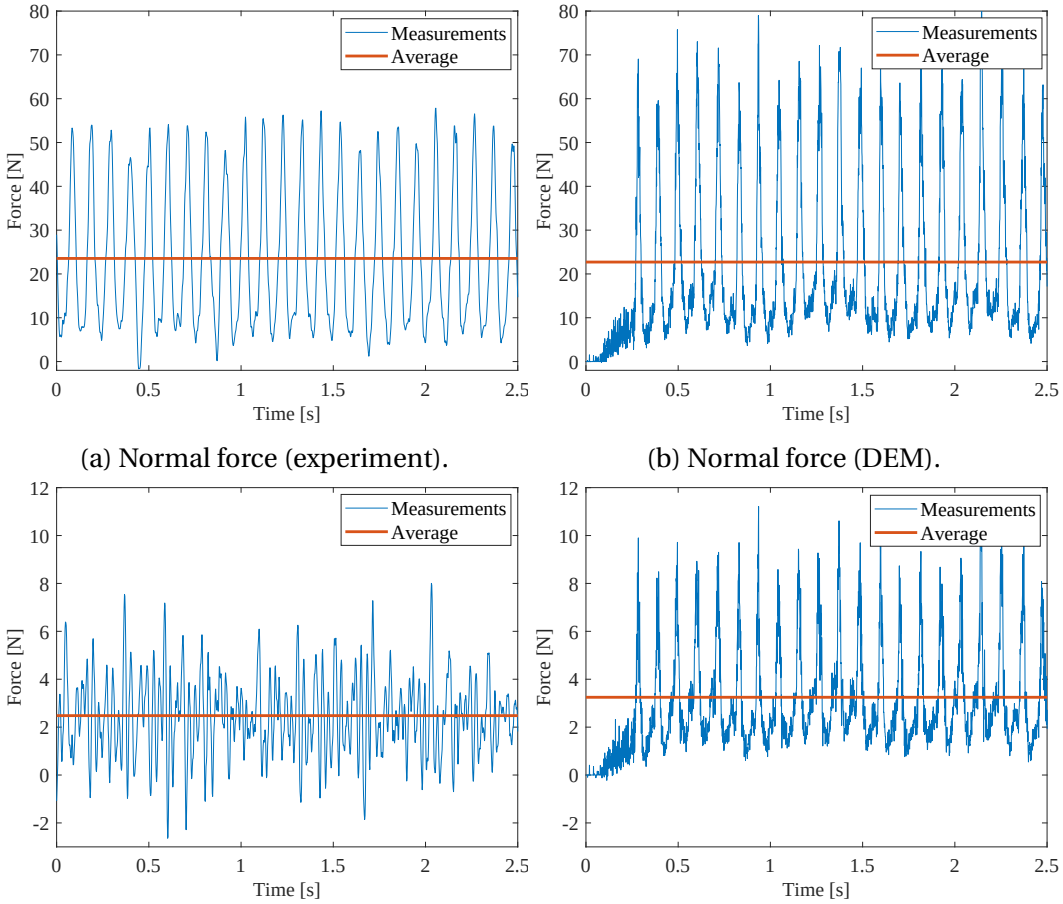

(a) Normal force (experiment).

(b) Normal force (DEM).

(c) Shear force (experiment).

(d) Shear force (DEM).

Figure 22: Force measurements from the (a,c) experimental tests and (b,d) DEM ($V_b = 3$ m/s and $\dot{m} = 8$ kg/s).

Fast Fourier transforms (FFT) were performed on the normal force measurements using the Hanning window function to eliminate the leakage in the continuous signal, see Figure 23. The experimental measurement, Figure 23a, showed

two clear peaks. The first and most dominant peak (9.74 Hz) was caused by the piled-up material between the chevron pattern and the smaller peak (19.35 Hz) was caused by the free-stream material between the pattern sets. The FFT of the DEM data (Figure 23b), showed five peaks with the first peak (1.20 Hz) caused by the method in which particles were generated and introduced into the model (see Appendix B for material overlap). The second peak (9.00 Hz) was the most dominant, i.e. the frequency caused by the chevron pattern. The remaining three peaks were created by the free-stream material with the peak at 18.25 Hz corresponding relatively well to the 19.35 Hz from the measured data.

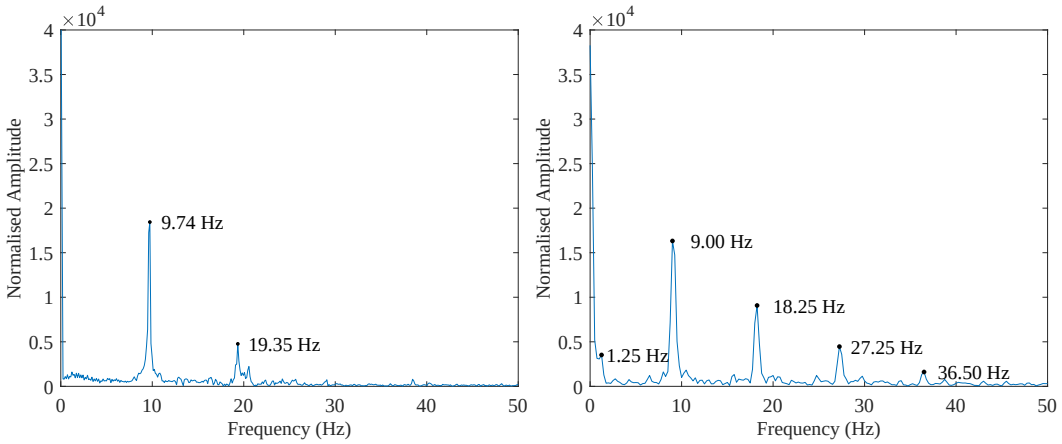

(a) Experimental test.

(b) DEM (pattern simulation model).

Figure 23: FFT of normal force measurements from the (a) experimental tests and (b) DEM model ($V_b = 3$ m/s and $\dot{m} = 8$ kg/s).

The peak created by the chevron pattern was the most important to be investigated. The theoretical frequencies were determined by dividing the belt speed by the pattern-to-pattern distance (330 mm),

$$f_{\text{peak}} = \frac{V_b}{0.33} \tag{8–43}$$

The measured data displayed a slight deviation (error ≤ 7.69 %, Figure 24a) from the theoretical values over a range of belt speeds. DEM, however, showed a good correlation with the theoretical frequencies (-1 % error). It was further observed in Figure 24a that the slope for a linear line through the experimental data points had a slightly larger slope compared to the theoretical line. This was due to the small error between the conveyor belt set speed and the actual speed (see Table 24 in Appendix A.2). When this error was accounted for, the results in Figure 24b were obtained. The error between the measured frequencies after correction and the theoretical results was less than 0.84 %. The theoretical, measured (before and after correction) and DEM frequencies are summarised in Table 6.

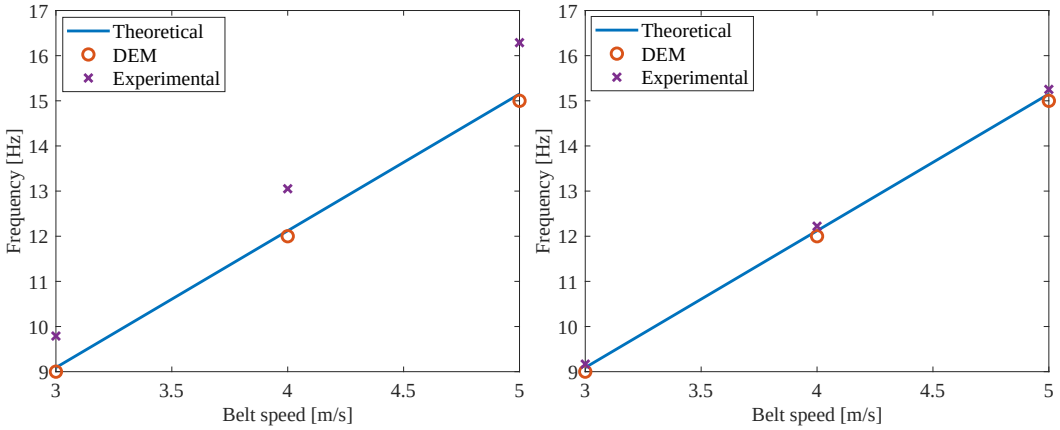

(a) Before correction.

(b) After correction.

Figure 24: Frequency comparison between theoretical, experimental tests and DEM for (a) before and (b) after correction.

Table 6: Determined experimental, theoretical and DEM frequencies from normal force measurements ($\dot{m} = 8$ kg/s).

Belt speed [m/s]	Frequency [Hz]				Error between theoretical and experimental, before correction	Error between theoretical and experimental, after correction	Error between theoretical and DEM
	Theoretical	Experimental		DEM			
		Before correction	After correction				
3	9.09	9.79	9.17	9.00	7.69 %	0.84 %	-1 %
4	12.12	13.05	12.22	12.00	7.68 %	0.83 %	-1 %
5	15.15	16.29	15.25	15.00	7.50 %	0.67 %	-1 %

The time integral averaged (Simpson's and trapezoidal rule) recorded normal and shear forces from the experimental tests, DEM and analytical models for belt speeds of 3 m/s and 4 m/s are shown in Figure 25. There were no significant difference between the results using the Simpson's and trapezoidal rule; however, the results by the Simpson's rule is presented for no specific reason. Furthermore, a summary of the normal, R_n, shear, R_s and magnitude, R, of the forces measured from the pattern and flat belt models are given in Table 7. It is clear from the results that in all four cases the reaction force increased with an increase in belt speed and mass flow rate. It can therefore be stated that the impact force is proportional to the particle momentum, i.e. $R \propto m\,V$. The results further showed that the normal force was accurately predicted by the pattern model but not by the flat belt model. However, both models failed to accurately predict the shear force component. Nonetheless, a good correlation was still found and the error in predicting the total reaction force by the pattern model was less than 8.57 % (see Table 7).

The flat belt simulations failed to accurately predict the reaction forces, estimating a smaller normal force and larger shear force relative to the measurements. As a result, the total force was also inaccurate, obtaining percentage errors larger than 12.26 %. Thus, it is concluded that the effect of the chevron pattern may

not be neglected for the simulation of inclined patterned conveyor belts. It is interesting to note that the pattern and flat belt simulations predicted very similar shear forces at both belt speeds. This could be due to the larger material impact angle for the flat belt simulations; coincidently, countering the effect of the smaller impact velocity (Section 7.3).

The analytical model showed acceptable accuracy in predicting the normal force at belt speeds of 3 m/s and 4 m/s, obtaining errors less than 13.54 % and 7.65 %, respectively. It did, however, failed significantly to predict the shear forces. Predicting a much smaller and larger shear force at $V_b = 3$ m/s and $V_b = 4$ m/s, respectively. The analytical model also failed to satisfy the relation for stationary flow (equation 4–4) at both belt speeds. This did not influence the normal force, however, it had an effect on the outflow velocity V_a; therefore, affecting the shear force. Grima (2011) obtained a similar result for a vertical impact plate where the analytical model failed to accurately predict the shear force due to the unsteady flow condition.

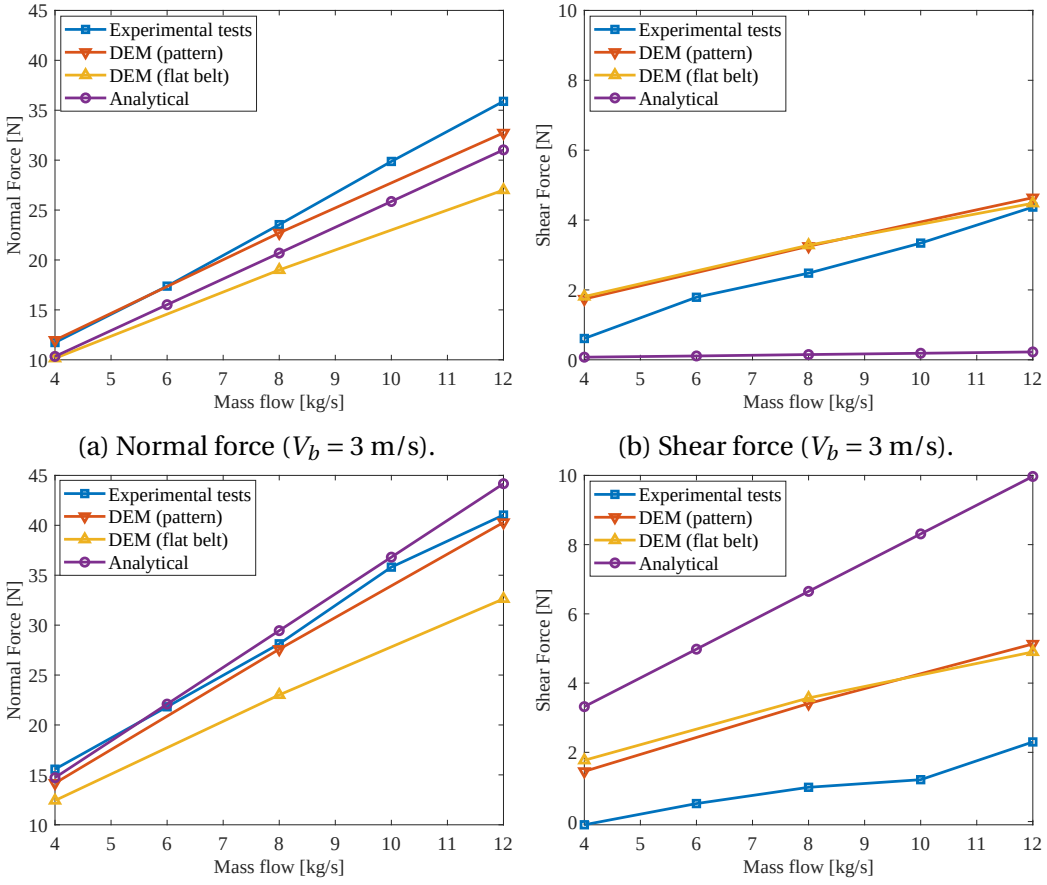

(a) Normal force ($V_b = 3$ m/s).

(b) Shear force ($V_b = 3$ m/s).

(c) Normal force ($V_b = 4$ m/s).

(d) Shear force ($V_b = 4$ m/s).

Figure 25: (a,c) Normal and (b,d) shear forces measured on a vertical impact plate for the experimental tests, pattern simulation model, flat belt simulation model and the analytical model.

Table 7: Normal R_n, shear R_s and total R forces (N) on the impact plate for the pattern and flat belt simulations.

Belt speed	Mass flow	Experimental			Pattern model				Flat belt model			
[m/s]	[kg/s]	R_n	R_s	R	R_n	R_s	R	Error*	R_n	R_s	R	Error*
3	4	11.73	0.61	11.75	11.97	1.74	12.10	2.98 %	10.15	1.81	10.31	-12.26 %
	8	23.54	2.48	23.67	22.71	3.25	22.94	-3.08 %	19.00	3.28	19.28	-18.55 %
	12	35.89	4.37	36.16	32.73	4.64	33.06	-8.57 %	27.00	4.48	27.37	-24.31 %
4	4	15.57	-0.09	15.57	14.17	1.45	14.24	-8.54 %	12.43	1.77	12.56	-19.33 %
	8	28.13	0.99	28.15	27.59	3.41	27.80	-1.24 %	23.01	3.57	23.29	-17.26 %
	12	41.03	2.33	41.10	40.29	5.13	40.62	-1.14 %	32.63	4.90	33.00	-19.69 %

*The percentage error was calculated for R relative to the experimental values.

8.2.2 Material Flow Characteristics (3-Clump Model)

The material flow characteristics comprised of the visualisation and quantification of the material flow before and after impacting the plate. The results from the DEM model and the Korzen analytical model were compared to the PIV results of the high-speed videos. The PIV analysis procedure is reported in Appendix G and the camera settings and setup described in Appendix A.3.

Figure 26 shows a comparison between DEM and a high-speed image for the material flow from the head pulley to the point where the material free-falls after impacting the plate. In this zone, the material impact velocity V_p, impact angle α_p, material build-up height H, outflow velocity V_a and the material outflow stream width W were investigated (see Figure 26a). In the DEM model, wind resistance was ignored, thus the particles could potentially have higher speeds at impact than in reality. However, over such a short distance, this effect was ignored.

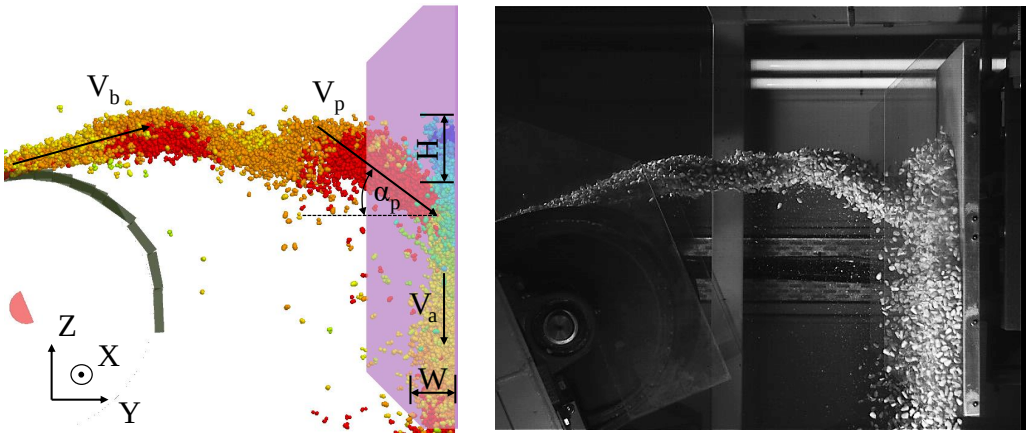

(a) DEM (3-clump particles).

(b) High-speed image.

Figure 26: Vertical impact plate material flow from (a) DEM and (b) high-speed footage ($V_b = 3$ m/s and $\dot{m} = 12$ kg/s).

The impact velocity V_p from PIV and DEM was determined by implementing spatial and time averaging, i.e. across the trajectory stream and over the entire duration of the simulation, where only time averaging was used to determine the rest

of the material flow characteristics. The material outflow velocity V_a was measured at a location 150 mm below the centre of the impact plate. The analytical model was limited to only determining the impact velocity, angle and outflow velocity. The results are summarised in Tables 8, 9 and 10.

In the experiment there was no significant change in the impact velocity with a change in mass flow rate, only in belt speed. The DEM results showed a similar trend and a good agreement for the impact velocity, especially at a belt speed of 3 m/s (|error| ≤ 2.88 %, Table 9). At V_b = 4 m/s, DEM estimated a slightly lower impact velocity with a maximum error of 5.31 %. The analytical model overestimated the impact velocity, but could still serve as an acceptable estimate since the error was less than 6.14 %. DEM accurately predicted the impact angle for V_b = 3 m/s with the largest deviation only 2.25°, slightly overestimating the angle in all cases. The analytical model also overestimated the angle by approximately 4.5°. For V_b = 4 m/s, the measured angle for all mass flows was negative, indicating that the material was still moving upwards at impact. The DEM and analytical models, however, both predicted small positive angles. However, the measured and predicted angles are all relatively small, indicating that the flow was almost horizontal at impact, and the models are still accurate with 4°, and thus acceptable. The DEM simulation model failed to accurately predict the material outflow velocity at V_b = 3 m/s, overestimating the velocity at flow rates of 8 kg/s and 12 kg/s (errors of 12.14 % and 19.90 %, respectively). However, the model showed very accurate results for V_b = 4 m/s (|error| ≤ 5.41 %). The analytical model predicted a very low outflow velocity, obtaining errors between -9.18 % and -19.38 %.

Table 8: Measured and predicted impact velocity V_p, angle α_p and outflow velocity V_a on a vertical plate (experimental, DEM and analytical model).

Belt speed [m/s]	Mass flow rate [kg/s]	Impact						Outflow		
		Velocity, V_p [m/s]			Angle, α_p [°]			Velocity, V_a [m/s]		
		Experimental	DEM	Analytical	Experimental	DEM	Analytical	Experimental	DEM	Analytical
3	4	2.78	2.73	2.94	15.57	16.75	19.89	2.20	2.28	1.78
	8	2.77	2.72	2.94	15.53	16.84	19.89	2.06	2.31	1.78
	12	2.78	2.70	2.94	15.18	17.43	19.89	1.96	2.35	1.78
4	4	3.59	3.43	3.68	-4.88	0.72	1.02	2.27	2.20	1.83
	8	3.58	3.39	3.68	-3.70	1.57	1.02	2.22	2.10	1.83
	12	3.58	3.46	3.68	-4.31	2.09	1.02	2.24	2.20	1.83

Table 9: Error in predicting V_p and V_a by the DEM and analytical models.

Belt speed [m/s]	Mass flow [kg/s]	Impact velocity [%]		Outflow velocity [%]	
		vs DEM	vs Analytical	vs DEM	vs Analytical
3	4	-1.80	5.76	3.64	-19.10
	8	-1.81	6.14	12.14	-13.59
	12	-2.88	5.76	19.90	-9.18
4	4	-4.46	2.51	-3.08	-19.38
	8	-5.31	2.79	-5.41	-17.57
	12	-3.35	2.79	-1.79	-18.30

The material build-up height H was measured as the distance between the upper trajectory stream (at impact) and the highest point of the material splashing upwards (see Figure 26a). Whereas, the width of the material flowing down after impact, W, was measured from the surface of the impact plate to the lower part of the stream, discarding particles which deviated too much away from the mainstream. The results presented in Table 10 showed that the build-up height predicted by DEM compared relatively well with the measurements. However, PIV identified an increase in H with an increase in belt speed. This was expected since the impact angle was slightly upwards for $V_b = 4$ m/s. It is interesting to note, DEM did not identify an increase in build-up height which can be attributed to the impact angle that was just above horizontal and slightly downwards (Table 8). It was found that W increased with an increase in mass flow rate and DEM slightly underestimated the material width. However, it is noted in Figure 26b that the camera perspective may had an influence on the measurements for the true material width in PIV; therefore, if this effect could be avoided, a better correlation would have been found.

Table 10: Measured and predicted material build-up height H and outflow stream width W.

Belt speed [m/s]	**Mass flow [kg/s]**	**Build-up, H [mm]**		**Stream width, W [mm]**	
		PIV	**DEM**	**PIV**	**DEM**
3	4	87	66	53	47
	8	82	94	66	59
	12	86	101	71	61
4	4	110	104	77	51
	8	111	97	79	55
	12	109	99	93	65

The material profile at the point of impact was investigated by taking a video of the material flow using a GoPro Hero 3. The GoPro was mounted on the conveyor structure and orientated in the direction of the belt motion. The position of the particles at impact from the DEM results was plotted on one of the video frames, Figure 27. Qualitatively, the DEM results compared well with the actual flow, showing the same "parabolic" shape.

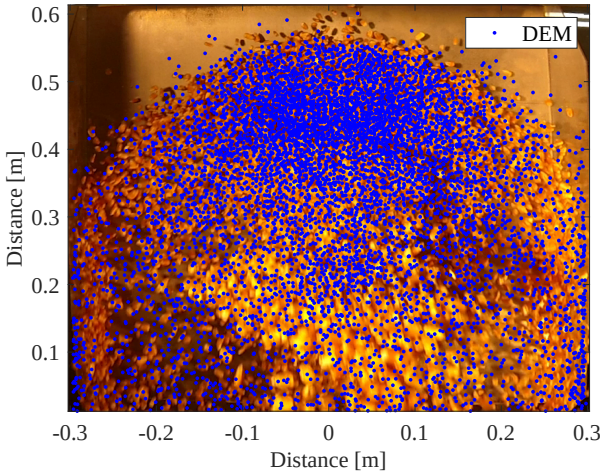

Figure 27: Material profile at impact (experimental and DEM).

8.2.3 Sensitivity to DEM Parameters (3-Clump Model)

8.2.3.1 Contact Damping

The critical damping ratio between the corn grains and aluminium, ζ_{pw}, was determined as 0.14 in Section 6.1.2, by implementing a drop test. It was assumed that the contact damping between the corn grains, ζ_{pp}, was the same as the particle-wall damping. Coetzee (2019) showed that the damping ratio had no significant effect on the angle of repose with the largest deviation angle found as 0.7° when the damping ratio was varied from 0.1 to 0.9. The effect of varying ζ_{pw} and ζ_{pp} was investigated for the vertical impact plate. Figure 28 shows a comparison between the measured impact forces and the DEM predictions for varying ζ_{pw} and ζ_{pp}, and a belt speed of 3 m/s and mass flow rates of 4 kg/s, 8 kg/s and 12 kg/s. The particle-wall damping ζ_{pw} had no significant effect on the results over the whole range of mass flow rates, Figure 28a. However, Figure 28b shows that for a low value of $\zeta_{pp} \approx 0.05$, the magnitude of the impact force was slightly lower and the effect more pronounced for higher mass flow rates. However, for higher values $\zeta_{pp} \geq 0.14$, there was no significant effect.

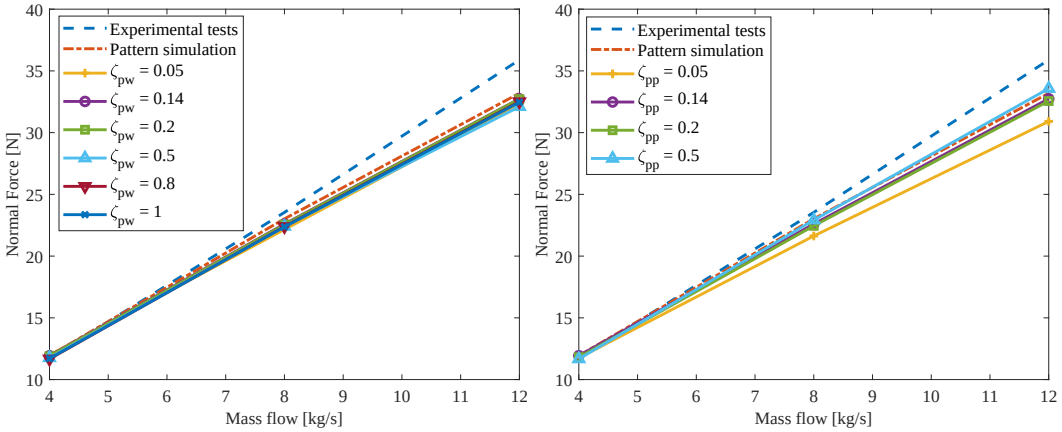

(a) ζ_{pw}. (b) ζ_{pp}.

Figure 28: Effect of (a) ζ_{pw} and (b) ζ_{pp} on the predicted average normal force on a vertical plate.

The effect of damping on the material flow, for various damping values, is shown in Figure 29. Intuitively, one would think that for higher contact damping between the particles and wall, a smaller build-up height H and outflow width W would result, but this was not the case and as shown in Figure 29a, at least qualitatively, the particle-wall damping had no significant effect on the flow from the head pulley, onto the impact plate, and downwards from the plate after impact. However, the particle-particle damping had a significant effect, Figure 29b. At low particle damping ($\zeta_{pp} = 0.05$), there was a major dispersion in the material stream where a large number of particles deviated from the mainstream. This was due to less energy dissipated during contact between particle collisions. For a high ζ_{pp}, the impact location was higher, and the build-up height was also higher. One would think that the build-up height would be less due to higher damping between the particles, causing fewer particles to splash upwards due to less available energy. Instead, the higher build-up was caused by the longer contact time and as a result, the incoming stream pushed more material upwards. As expected, the free-falling material after impact generated a much larger outflow width for $\zeta_{pp} = 0.05$. The results are summarised in Table 11. It is clear that there was a discrepancy between the material characteristics for a change in ζ_{pp}; therefore, in-depth calibration of the contact damping is necessary when the material flow from a conveyor belt is to be accurately simulated.

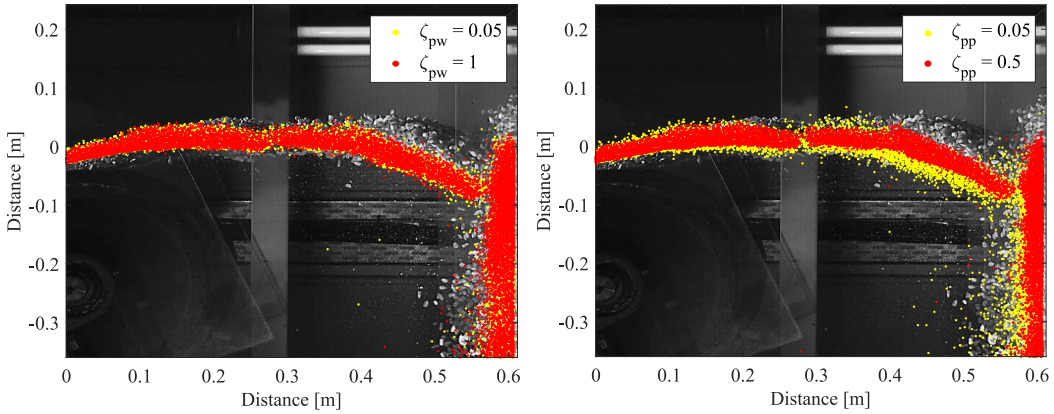

(a) ζ_{pw}. (b) ζ_{pp}.

Figure 29: Material flow for high and low values of (a) ζ_{pw} and (b) ζ_{pp} onto a vertical plate ($V_b = 3$ m/s and $\dot{m} = 12$ kg/s).

Table 11: Predicted material flow characteristics for $\zeta_{pp} = 0.05$ and $\zeta_{pp} = 0.5$ on a vertical plate ($V_b = 3$ m/s and $\dot{m} = 12$ kg/s).

μ_{pp}	Impact		Outflow	Build-up height,	Width of outflow
	Velocity, V_p [m/s]	Angle, α_p [°]	Velocity, V_a [m/s]	H [mm]	stream, W [mm]
0.05	2.65	17.72	2.33	58	57
0.5	2.75	15.51	2.37	91	33

8.2.3.2 Contact Stiffness

From the findings in Section 6.2.4, k_{pp} and k_{pw} were selected as 1 kN/m and 2 kN/m, respectively. The effect of contact stiffness on the reaction forces was investigated by repeating the simulations with $V_b = 3$ m/s and $\dot{m} = 8$ kg/s while scaling both stiffness' up by factors of 10 and 100, respectively. The average normal and shear forces predicted are presented in Table 12. It is clear that the reaction forces were insensitive to the contact stiffness. Hence, the selected k_{pp} and k_{pw} parameter values were subsequently used.

Table 12: Effect of k_{pw} and k_{pp} on the predicted average normal and shear forces on a vertical plate ($V_b = 3$ m/s and $\dot{m} = 8$ kg/s).

	k_{pw} [kN/m]			k_{pp} [kN/m]		
	2	**20**	**200**	**1**	**10**	**100**
Normal force [N]	22.71	22.66	22.47	22.71	22.62	22.77
Shear force [N]	3.25	3.20	3.14	3.25	3.24	3.28

8.2.3.3 Particle Friction

More particle friction parameter combinations were investigated for the 3-clump particle from the two feasible regions shown in Figure 14b (Section 6.2.3), as well

as a combination having a slightly higher μ_{pp} and $\mu_{r\,pp} \neq 0$, as shown in Table 13. The results showed that the reaction forces on the vertical impact plate were insensitive to the particle friction and as a result, no friction combination accurately predicted the shear force. However, the after-impact velocity V_a was accurately predicted only for $\mu_{pp} = 0.17$ and $\mu_{r\,pp} = 0$. This friction combination fell in the feasible region obtained by Coetzee (2020).

Table 13: Predicted reaction forces, impact velocity and outflow velocity for various combinations of μ_{pp} and $\mu_{r\,pp}$ on a vertical plate ($V_b = 3$ m/s and $\dot{m} = 8$ kg/s).

		Reaction forces and material characteristics			
μ_{pp} [-]	**$\mu_{r\,pp}$ [-]**	**R_n [N]**	**Compared to* measurements**	**R_s [N]**	**Compared to* measurements**
0.05	0.80	22.16	-5.86 %	3.14	26.61 %
0.15	0	22.71	-3.53 %	3.25	31.05 %
0.17	0	22.77	-3.27 %	3.20	29.03 %
0.25	0.125	23.02	-2.21 %	3.24	30.65 %
		V_p [m/s]	**Compared to* measurements**	**V_a [m/s]**	**Compared to* measurements**
0.05	0.80	2.70	-2.53 %	2.32	12.62 %
0.15	0	2.72	-1.81 %	2.31	12.14 %
0.17	0	2.74	-1.08 %	1.92	-6.80 %
0.25	0.125	2.79	0.72 %	2.36	14.56 %

*The percentage error was calculated by comparing the DEM results to the results of the experimental tests.

8.2.4 Particle Scale (3-Clump Model)

The scaling procedure of the DEM particles is presented in Appendix B and the effect of the scaling factor on the computation time in Appendix D. The analysis was conducted for the pattern and clump acceleration models where the velocity of the conveyor was 3 m/s and the mass flow rates varied between 4 kg/s and 12 kg/s. The measured normal force for scaling factors up to 10 is shown in Figure 30. Reasonable predictions ($|\text{error}| \leq 6.49$ %) of the average reaction force were obtained for scaling factors up to 8 for both simulation methods. Large deviations started to occur at a scale of 10.

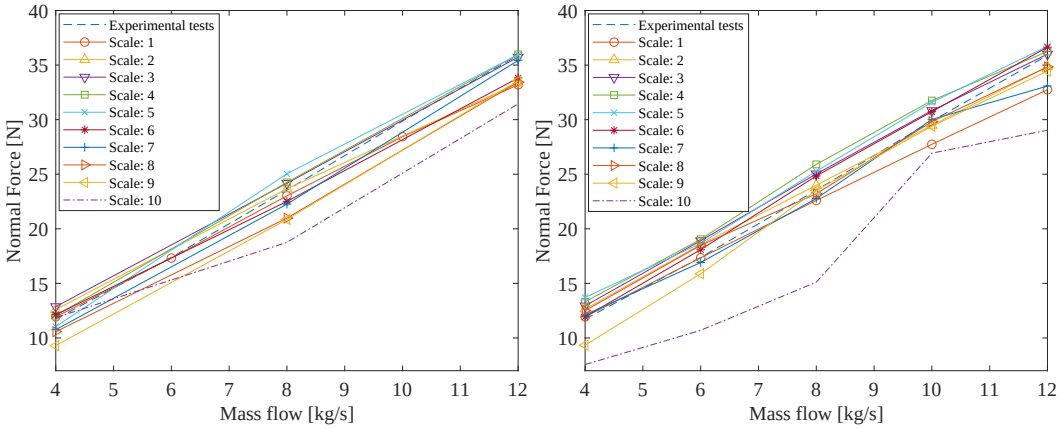

(a) Pattern model.

(b) Clump acceleration model.

Figure 30: Predicted normal force measurements on a vertical plate for scaled particles using the (a) pattern and (b) clump acceleration model ($V_b = 3$ m/s).

Although scaling factors up to 8 accurately predicted the reaction force, only scaling factors up to 7 could accurately predict the frequency content, Figure 23b. Due to a reduction in the number of particles with larger scale factors, the model could no longer predict the frequency content due to the chevron pattern. The discharge velocity and trajectory of the scaled particles (up to a factor of 10) were also investigated for a belt speed of 3 m/s and a mass flow rate of 8 kg/s. Spatial averaging was performed on the discharge velocity, Figure 31 (note that only the results up to a scale factor of 7 is shown). For all scale factors, there was only a slight velocity offset compared to a scale factor of 1. Furthermore, scaling did not affect the trajectory and impact position. It was established in Section 8.2.1 (Figure 25) that the reaction force is proportional to the particle momentum; however, based on the results in Figure 31 and the constant mass flow rate generated in the system, the particle momentum did not change. This seems to be counter-intuitive, since only scaling factors up to 8 could accurately predict the reaction forces. Possible reasons for the limiting scaling factor could be a research area for the future. It is concluded that the particle size can be increased by a factor of 7 for impact plate analyses where the impact velocity, position and average reaction force is of interest.

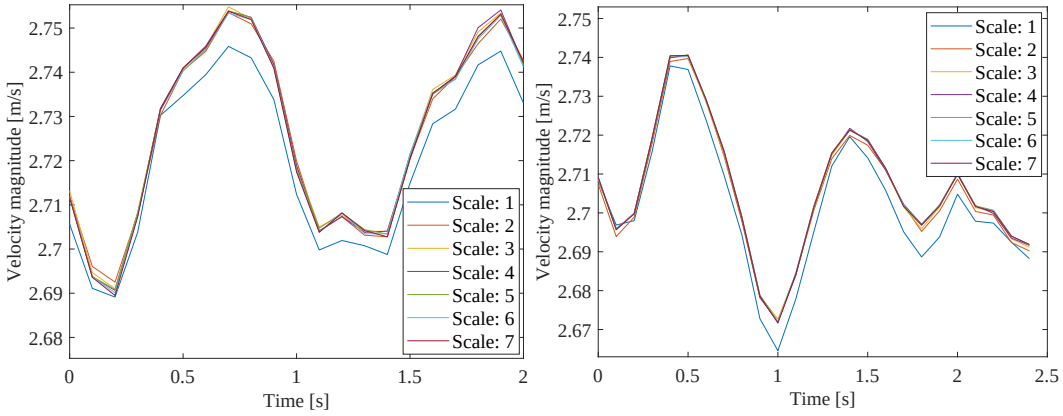

(a) Pattern model.

(b) Clump acceleration model.

Figure 31: Material discharge velocity for scaled particles using spatial averaging ($V_b = 3$ m/s and $\dot{m} = 8$ kg/s).

8.2.5 Effect of Particle Shape

8.2.5.1 Clumps

Up to this point, only the 3-clump particles were used. However, the DEM parameter values presented in Table 4 were also used for the 5- and 10-clump models in order to identify the influence of a more accurate particle shape model on the vertical impact plate results. The particle friction μ_{pp} was set to 0.15 and the particle rolling friction $\mu_{\text{r pp}}$ to 0, and the pattern and clump acceleration methods were considered for this investigation. The DEM results are summarised in Table 27 in Appendix H.1. It was established that the particle shape had no significant effect on the reaction force, impact velocity, angle or after-impact velocity. Interestingly, it was found that the true force peaks, as a result of the chevron pattern, were accurately predicted by the 5- and 10-clump particles. The error relative to the peak forces of the force measurement (Figure 25a) were 35.78 %, 7.94 % and -8.99 % for the 3-, 5-, and 10-clump particles, respectively. As a result, when the force peaks, and not only the average values, are of interest, more accurate particle shapes should be considered. This might become important when the DEM model is used to predict material wear.

8.2.5.2 Balls

As discussed in Section 6.2.3, the particle sliding friction μ_{pp} and rolling friction $\mu_{\text{r pp}}$ for the ball particle model were initially estimated as 0.20 and 0.125, respectively. A sensitivity study was performed to obtain the particle-wall rolling friction $\mu_{\text{r pw}}$ for the conveying of the material where the normal impact force was used as the calibration measure (Appendix H.2). It was found that for a $\mu_{\text{r pw}}$ value greater than 0.10, it had no significant effect on the reaction forces, and as a result, the magnitude of the reaction forces depended solely on the inter-particle friction. Therefore, additional combinations of μ_{pp} and $\mu_{\text{r pp}}$ (with $\mu_{\text{r pw}} = 0.10$)

were investigated. The results showed that the calibrated friction parameters by Coetzee (2020) could not provide the necessary accuracy in predicting the reaction forces (12.31 % ≤ |error| ≤ 17.81 %). The particle rolling friction $\mu_{\mathrm{r\,pp}}$ values were then further increased. It was found that the calibrated μ_{pp} of 0.25 was the only particle sliding friction combination which accurately predicted the material impact force (-7.77 % error), velocity (-0.72 % error) and angle (-0.66 % error) after $\mu_{\mathrm{r\,pp}}$ was increased to 0.50. Larger μ_{pp} values were also investigated while the particle rolling friction was set to a low value of 0.125. The particle sliding friction combinations for 0.40 and 0.70 also displayed accurate results for predicting the impact force, velocity and angle, obtaining a maximum error of -9.15 %. No combination of parameters μ_{pp} and $\mu_{\mathrm{r\,pp}}$ could predict the after-impact velocity V_a, predicting a significantly higher velocity (20.41 % ≤ error ≤ 23.98 %). It was therefore concluded that due to the ball particle's shape, having only a single contact with the impact plate, the friction had a negligible influence on the outflow velocity of the particles. It was also found that the material profile at discharge was 5 mm higher for the ball particles than for the 3-clump particles. This was due to the increase in porosity when using ball particles. From the material trajectory plot, the effects of the increase in porosity and reduced interlocking of the particles were evident, resulting in a large number of particles deviating away from the mainstream.

8.3 Angled Impact Plate Results and Discussion

The impact plate was investigated for the case where it had a positive tilt angle β, 30° and 45°, and placed at a distance of 510 mm from the head pulley, Figure 32. From an academic perspective, the friction of the impact plate was further increased by glueing P40 sandpaper to its face (see Figure 67 in Appendix I).

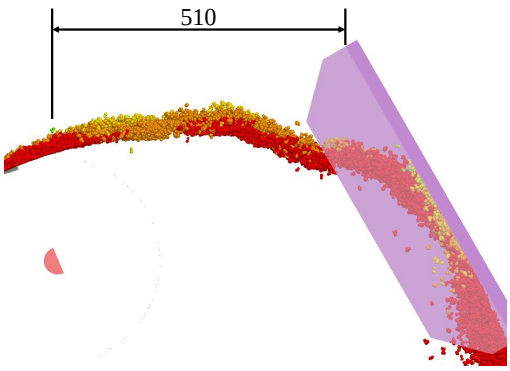

(a) DEM ($\beta = 30°$), dimensions in mm.

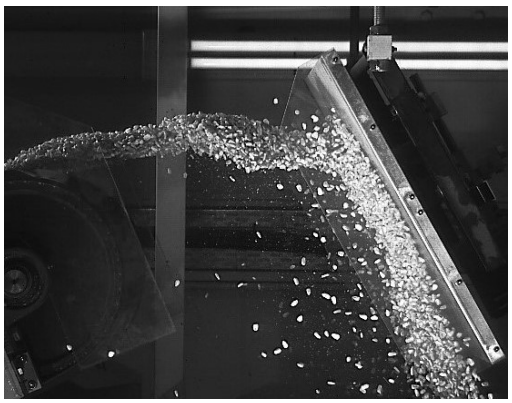

(b) High-speed image ($\beta = 30°$).

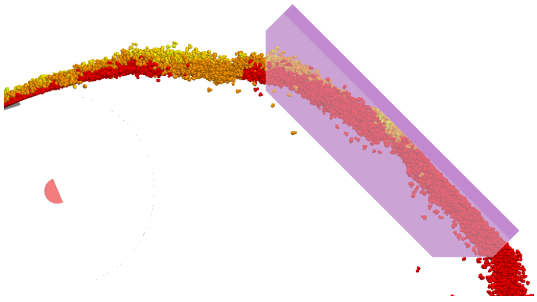

(c) DEM ($\beta = 45°$).

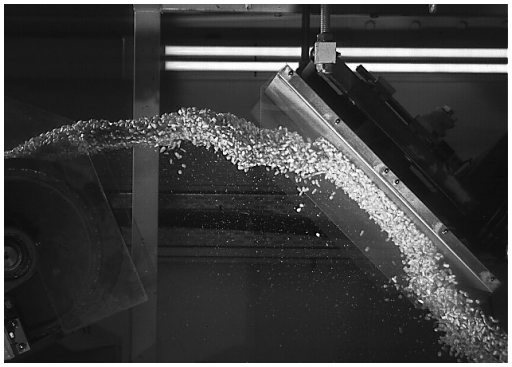

(d) High-speed image ($\beta = 45°$).

Figure 32: Material flow onto an angled aluminium impact plate from (a,c) DEM and (b,d) high-speed footage for $\beta = 30°$ and $\beta = 45°$ ($V_b = 3$ m/s and $\dot{m} = 12$ kg/s).

8.3.1 Impact Forces and Surface Friction (3-Clump Model)

The clump acceleration method was used throughout since there was no significant difference with the pattern simulation model (see Table 14), and this reduced computation time.

Table 14: DEM reaction force comparison between the clump acceleration and pattern model for a tilted plate ($V_b = 3$ m/s and $\dot{m} = 8$ kg/s).

Tilt angle, β [°]	**Pattern**			**Clump acceleration**		
	$\mathbf{R_n}$	$\mathbf{R_s}$	$\mathbf{R_s/R_n}$	$\mathbf{R_n}$	$\mathbf{R_s}$	$\mathbf{R_s/R_n}$
30	12.50	2.87	0.23	12.94	3.01	0.23
45	7.05	1.70	0.24	7.23	1.76	0.24

A summary of the average forces measured on the aluminium and P40 sandpaper plate for tilt angles of 30° and 45° is shown in Table 15. The standard friction tests discussed in Section 6.1.3, did not provide consistent results for the particle-wall coefficient of friction. Therefore, a sensitivity study was conducted where the

normal and shear forces were obtained while systematically varying the sliding friction parameter μ_{pw}. The "effective" friction between the material and plate was also calculated by dividing the measured shear force by the normal force, R_s/R_n. The experiments and DEM models both showed an increase in the "effective" friction with an increase in the tilt angle. Moreover, a larger increase was observed for the P40 sandpaper surface. Furthermore, the measured "effective" friction for both surfaces and tilt angles was within the ranges predicted by DEM; however, the magnitude of the DEM force components was slightly lower.

Table 15: Average measured and predicted impact forces on the aluminium and P40 sandpaper angled impact plate for $\beta = 30°$ and $\beta = 45°$ ($V_b = 3$ m/s, $\dot{m} = 8$ kg/s and $\mu_{pp} = 0.15$).

β [°]		Experimental tests		DEM results Particle - wall sliding friction, μ_{pw} [-]								
		Aluminium	**P40 sandpaper**	**0.2**	**0.25**	**0.3**	**0.4**	**0.5**	**0.6**	**0.7**	**0.8**	**0.9**
30	**Normal force, R_n [N]**	15.54	15.9	12.91	12.94	12.98	13.12	13.31	13.61	13.79	14.01	14.15
	Shear force, R_s [N]	3.50	4.6	2.44	3.01	3.55	4.54	5.35	5.99	6.47	6.79	7.03
	R_s/R_n [-]	0.23	0.29	0.19	0.23	0.27	0.35	0.40	0.44	0.47	0.48	0.50
45	**Normal force, R_n [N]**	8.36	9.31	7.15	7.23	7.27	7.49	7.77	8.07	8.35	8.49	8.74
	Shear force, R_s [N]	2.12	5.36	1.4	1.76	2.12	2.86	3.56	4.18	4.68	5.01	5.26
	R_s/R_n [-]	0.25	0.58	0.20	0.24	0.29	0.38	0.46	0.52	0.56	0.59	0.60

In order to summarise the friction measurements two graphs were constructed as shown in Figure 33. The light and dark blue (aluminium and P40 sandpaper, respectively) shaded regions represent the maximum and minimum friction coefficients measured in the standardised tests (Section 6.1.3). For a tilt angle of 30°, the measured "effective" friction was within the range of friction coefficients measured for aluminium, but not for the sandpaper, Figure 33a. However, for a tilt angle of 45°, the measured "effective" friction was well within the measured ranges for both surfaces, Figure 33b. The reason for this might be that for an angle of 45°, the particles stay longer in contact with the plate, and as the particles slide, more of the friction is mobilised (contacts are sliding and not in the elastic range). Thus, the "effective" friction is a measure of how many contacts are sliding, and for larger tilt angles this measure approaches the particle-wall coefficient of friction as almost all contacts are sliding.

The results further showed that for both tilt angles, the DEM results corresponded well to the measurements for aluminium if $\mu_{pw} = 0.25$. This value was also well within the range measured in the standard tests. For the sandpaper, the experiment showed that most of the contacts for a tilt angle of 45° were mobilised; hence, this was used to determine from the DEM model that $\mu_{pw} = 0.80$.

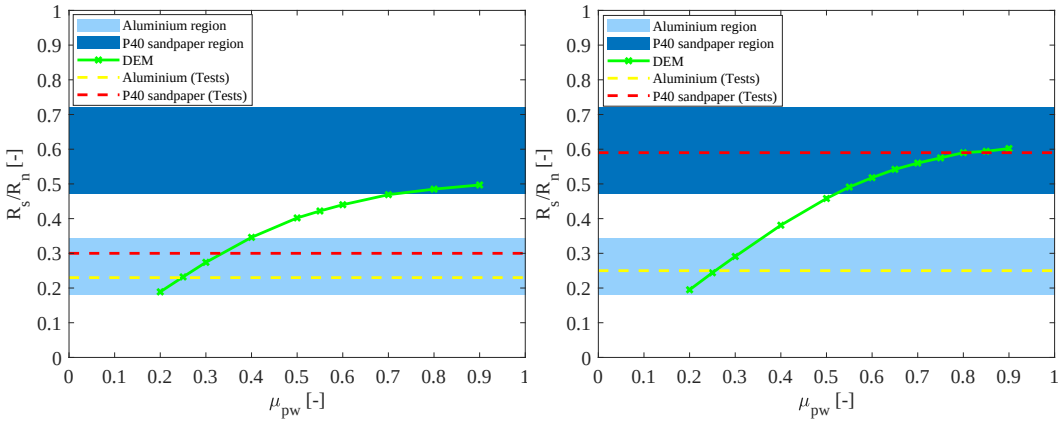

(a) 30°. (b) 45°.

Figure 33: Relationship between R_s and R_n for variation of μ_{pw} ($V_b = 3$ m/s, $\dot{m} = 8$ kg/s and $\zeta_{\text{pw}} = 0.14$).

The material flow comparison between DEM and the high-speed footages are discussed in Appendix I. It was visually found that the flow from DEM compared very well to the actual flow. Furthermore, the results showed that DEM accurately predicted the outflow velocity on both surfaces and tilt angles with an |error| ≤ 1.44 % and ≤ 8.33 % on the aluminium and P40 sandpaper surface, respectively.

8.3.2 Sensitivity to DEM Parameters (3-Clump Model)

8.3.2.1 Particle Friction

It was concluded in the sections above that although the "effective" friction was accurately predicted, the magnitude of the normal and shear force was underestimated. Therefore, additional particle friction combinations were investigated, and only the simulations for a tilt angle of 45° was considered. The simulation results for the various combinations of μ_{pp} and $\mu_{\text{r pp}}$ are summarised in Table 16. The results showed that there was an increase in the reaction forces for an increase in particle friction. Although the R_n and R_s force components increased, the "effective" friction, R_s/R_n, only decreased slightly for $\mu_{\text{pp}} \geq 0.15$, and yet still correlated very well to the experimental results. Furthermore, the two combinations which accurately predicted the reaction forces on both surfaces were for μ_{pp} equal to 0.20 and 0.25 with $\mu_{\text{r pp}} = 0$. For these parameter combinations, the error in "effective" friction was ≤ 3.45 %. It was also found that the particle friction had a negligible effect on the after-impact velocity (also shown for the vertical impact plate in Section 8.2.3.3). Considering all the findings for the vertical and angled impact plate, using the 3-clump particles, the feasible region in Figure 14b for $0.05 \leq \mu_{\text{pp}} \leq 0.08$ failed to comply with the experimental measures; however, the second feasible region at $\mu_{\text{pp}} = 0.17$ yielded accurate results only for the vertical plate. Therefore, caution needs to be taken when using this feasible region to predict impact forces. It is concluded that using only the standard

calibration tests, as described in Section 6.2.3, would be insufficient for accurate impact plate modelling, and needs further calibration and validation.

Table 16: Predicted reaction forces and after-impact velocity on an angled impact plate ($\beta = 45°$) for change in μ_{pp} and $\mu_{r\,pp}$ ($V_b = 3$ m/s and $\dot{m} = 8$ kg/s).

			Reaction forces and after-impact velocity			
μ_{pw}	μ_{pp}	$\mu_{r\,pp}$	R_n [N]	Compared to* to measurements	R_s [N]	Compared to* to measurements
0.25	0.05	0.80	6.08	-27.27 %	1.49	-29.72 %
	0.15	0	7.23	-13.52 %	1.76	-16.98 %
	0.15	0.125	7.79	-6.82 %	1.90	-10.38 %
	0.17	0	7.26	-13.16 %	1.75	-17.45 %
	0.20	0	7.96	-4.78 %	1.94	-8.49 %
	0.25	0	8.38	0.24 %	2.03	-4.25 %
0.80	0.05	0.80	7.33	-21.27 %	4.76	-11.19 %
	0.15	0	8.49	-8.81 %	5.01	-6.53 %
	0.15	0.125	9.08	-2.47 %	5.26	-1.87 %
	0.17	0	8.28	-11.06 %	4.54	-15.30 %
	0.20	0	9.32	0.11 %	5.32	-0.75 %
	0.25	0	9.60	3.11 %	5.39	0.56 %
			R_n/R_s [-]	Compared to* to measurements	V_a [m/s]	Compared to* to measurements
0.25	0.05	0.80	0.25	0 %	3.10	-0.32 %
	0.15	0	0.24	-4.00 %	3.10	-0.32 %
	0.15	0.125	0.24	-4.00 %	3.06	-1.61 %
	0.17	0	0.24	-4.00 %	3.07	-1.22 %
	0.20	0	0.24	-4.00 %	3.07	-1.22 %
	0.25	0	0.24	-4.00 %	3.06	-1.61 %
0.80	0.05	0.80	0.65	12.07 %	2.75	-8.33 %
	0.15	0	0.59	1.72 %	2.75	-8.33 %
	0.15	0.125	0.58	0 %	2.73	-9.00 %
	0.17	0	0.55	-5.17 %	2.81	-6.33 %
	0.20	0	0.57	-1.72 %	2.75	-8.33 %
	0.25	0	0.56	-3.45 %	2.74	-8.67 %

*The percentage error was calculated by comparing the DEM results to the results of the experimental tests.

8.3.3 Effect of Particle Shape

8.3.3.1 Clumps

The effect of accurate 5- and 10-clump particles on the angled impact plate was investigated. The calibrated μ_{pw} for aluminium and P40 sandpaper was used with the contact damping ζ_{pp} as 0.14, the particle friction μ_{pp} was 0.15 and the particle rolling friction $\mu_{r\,pp}$ was 0. The results are summarised and discussed in Appendix J.1. It was found that these shapes predicted lower impact forces compared to 3-clump particles (0.29 % ≤ error ≤ -36.65 %). The 5- and 10-clump particles, however, showed an increase in the "effective" friction on both surfaces and tilt angles due to an increase in coordination number. Using the 5-clump particles, the "effective" friction on the aluminium and P40 sandpaper surfaces were accurately determined (error of 0 % and 5.17 %, respectively); however,

for the 10-clump particles, only the friction on the aluminium plate was accurately predicted where the friction on the sandpaper surface was overestimated by 15.51 %. Furthermore, the after-impact velocity obtained by the 5- and 10-clump particle models showed no significant difference to the 3-clump model (0.32 % ≤ |error| ≤ 1.22 %).

8.3.3.2 Balls

The accuracy with which the ball particles could predict the impact forces and after-impact velocity on an angled impact plate was investigated by testing various combinations of μ_{pp} and $\mu_{r\,pp}$. The calibrated particle-wall friction μ_{pw} of the surfaces was used and the contact damping ζ_{pp} was also set to 0.14. The simulation results for $\beta = 45°$ are shown and discussed in Appendix J.2. The results for the particle friction combination of $\mu_{pp} = 0.20$ and $\mu_{r\,pp} = 0.125$, which was in the centre of the feasible region (Figure 14a) obtained by Coetzee (2020), showed inaccuracies. It was found that all the particle friction combinations successfully predicted the after-impact velocity on the angled plate (|error| ≤ 5.67 %). These findings were surprising since for the vertical plate no particle friction value could accurately predict the velocity. Furthermore, the simulation results showed that the combinations of $\mu_{pp} = 0.25$ and $\mu_{r\,pp} = 0.50$, and $\mu_{pp} = 0.40$ and $\mu_{r\,pp} = 0.125$ were most accurate in predicting the reaction forces (|error| ≤ 7.55 %) and friction (|error| ≤ 8.00 %) on the aluminium surface. However, for the P40 sandpaper, all the combinations failed to accurately predict the shear force component (-9.89 % ≤ error ≤ -39.55 %) and "effective" friction (-20.69 % ≤ error ≤ -29.31 %). A reason for this could be due to the ball particle's shape, resulting in only a single contact.

9 Transfer Hood Analysis

The purpose of a transfer hood is to change the direction of the feeding material and reduce the horizontal velocity component, without significantly decelerating the material (Doroszuk and Król, 2019). A transfer hood is usually located in a hood-spoon configuration or before an intermediate chute. According to Scott and Choules (1993), it is important to recognise the transfer hood-spoon configuration as two distinct sections having different design approaches, where the hood receives the material from the head pulley and the spoon/chute receives the material from the hood and symmetrically loads it onto the receiving belt. However, for designing an optimum transfer chute, the two sections should be assessed as an assembly. In this section, only the transfer hood is evaluated.

9.1 Transfer Hood Analytical Model

The derived analytical model consisted of a combination of the trajectory, impact plate (Section 4.2) and hood models (Section 4.3). The material velocity through

the hood was determined using equation 4–21; however, to determine the constant of integration K (equation 4–22), the initial material velocity V_0 was first determined. This was done using the impact plate model to iteratively determine the after impact velocity V_a, equation 4–7. However, before V_a was solved, the angle of the impacted surface on the hood, β, was identified. This was done by using the discharge and trajectory models. There are numerous trajectory models available such as Roberts (2001), C.E.M.A. (2005), Korzen (1989), Golka (1992, 1993), etc. to model the discharge and trajectory of the material from the head pulley. All four theories were investigated and the results are shown in Figure 34. Golka's formulae determines an upper and lower trajectory quantified by two unique parameters ($\epsilon_1 = \epsilon_2 = 0.05$), while the other models determines the trajectory of the centre of the stream. Furthermore, the C.E.M.A. (2005) guide provides a reference table for the material fall distance over a certain time interval, which was used to plot the vertical component of the trajectory path. The formulations of Korzen, Roberts and Golka are based on dynamic principles and projectile motion which includes factors such as friction, air drag, bulk density, etc. The trajectories of C.E.M.A, Korzen and Roberts showed similar impact positions for both belt speeds and the centre of the stream was between the upper and lower bounds of Golka. The trajectory stream in Figure 34 shows that the material hit the hood at approximately $\theta_0 = 6°$ ($V_b = 3$ m/s) and $\theta_0 = 51°$ ($V_b = 4$ m/s). Based on the definition in Figure 2, the impact angle β was determined as 8° and 51° for belt speeds of 3 m/s and 4 m/s, respectively. Once the initial (impact) velocity V_0 and angle θ_0 were defined, the material velocity profile of the hood was determined.

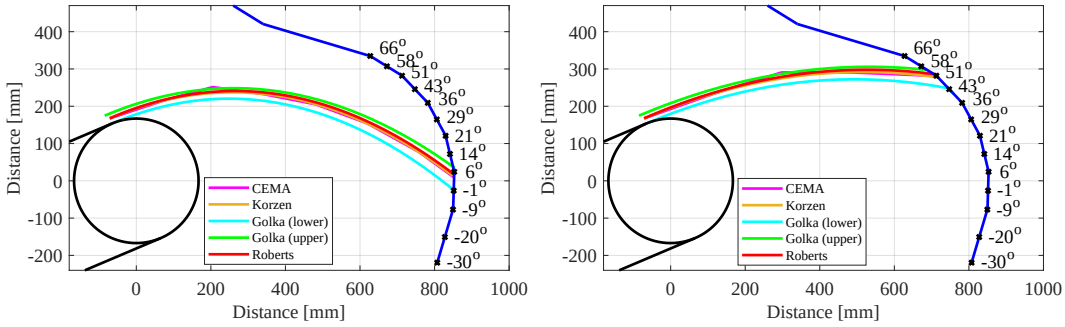

(a) $V_b = 3$ m/s. (b) $V_b = 4$ m/s.

Figure 34: Discharge trajectory of the material impacting the hood according to the analytical models.

9.2 DEM Model of the Transfer Hood

Figure 35 shows the DEM model used with the distance from the head pulley to the centre of the hood's curvature (note that the centre of the hood was 17 mm below the head pulley's centre). The hood consisted of polycarbonate panels which were bolted to two polycarbonate side panels to ensure that the mate-

rial did not leave the hood sideways. The curved part consisted of flat panels, arranged on a radius R of approximately 373 mm. The last panel at the outlet made an angle of -107° relative to the Y-axis. This ensured that the material was directed down the centre of the chute. The position, velocity and acceleration of the particles were recorded at 10 Hz and the parameter values in Table 4 were used. Only the 3-clump particle shape was considered for this analysis and the simulation time was selected as 5 s (see Appendix E).

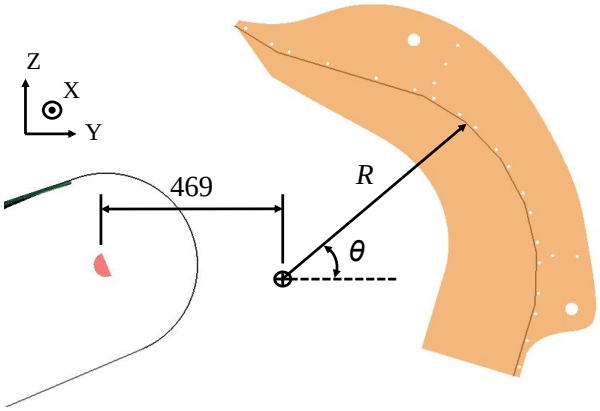

Figure 35: DEM model for transfer hood analysis, dimensions in mm.

9.3 Transfer Hood Results and Discussion

The transfer hood was analysed at belt speeds of 3 m/s and 4 m/s with mass flow rates of 4 kg/s, 8 kg/s and 12 kg/s. The impact location, material velocity, stream thickness and width through the hood as predicted by DEM were compared to measured results, Figure 36. The analytical model was limited to estimating only the impact location and material velocity. The results for the material flow through the hood was presented i.t.o. the angular position θ along the hood's perimeter, Figures 34 and 35, which was from the impact position (θ_0) to the outlet of the hood (-30°).

9.3.1 Material Flow Characteristics (3-Clump Model)

Figure 36 shows the predicted and experimental flow through the transfer hood for V_b = 4 m/s and $\dot{m}$ = 8 kg/s. It is clear that DEM estimated a significant flow separation for the higher speed condition compared to the flow at V_b = 3 m/s, presented in Figure 26a. Nonetheless, the trajectory and impact position of the material qualitatively correlated very well with the high-speed footage.

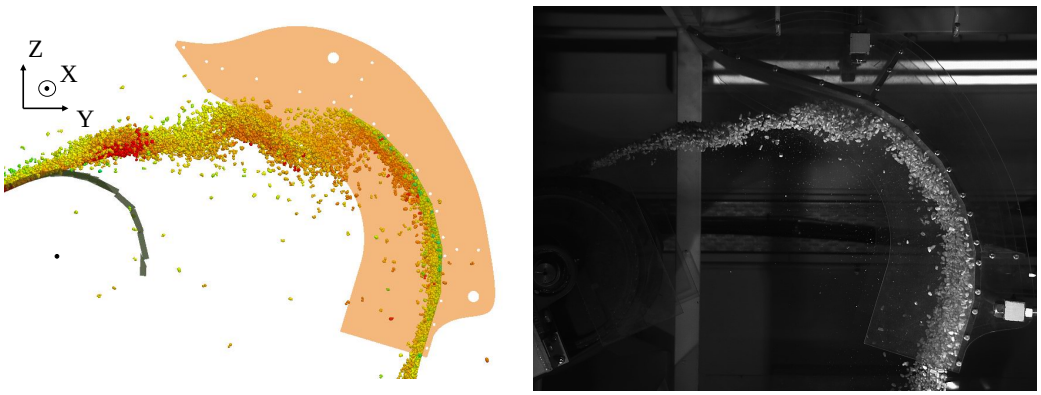

(a) DEM (3-clump particles).

(b) High-speed image.

Figure 36: Transfer hood material flow between (a) DEM and (b) high-speed footage ($V_b = 4$ m/s and $\dot{m} = 8$ kg/s).

The impact position on the transfer hood for the two investigated belt speeds are shown in Table 17. The values obtained were measured from the centre of the head pulley to the centre of the material stream at impact. The results showed that the impact position from DEM correlated very well with the PIV results; however, the analytical model predicted a slightly lower impact position.

Table 17: Impact position on the hood measured from the centre of the head pulley.

Belt speed, V_b [m/s]	**Impact position [mm]**					
	DEM		**PIV**		**Analytical**	
	Y	**Z**	**Y**	**Z**	**Y**	**Z**
3	830.9	74.7	832.2	72.0	852.7	18.6
4	660.0	307.9	663.6	305.2	712.8	281.9

Figures 37a ($V_b = 3$ m/s) and 37b ($V_b = 4$ m/s) shows the measured and predicted velocity profile through the hood, including the results for the variation in μ_{pw} for a mass flow of $\dot{m} = 12$ kg/s. The material was tracked in PIV at the centre of the stream and at the wall. The analytical velocity profile at a belt speed of 4 m/s, showed very good agreement with the PIV and DEM results. However, for the lower belt speed, the analytical model failed to accurately predict the velocity profile. This was due to the trajectory model predicting a lower impact position, consequently the impact angle β was smaller and resulted in a significant decrease in the velocity.

For $V_b = 3$ m/s, the velocity profile at the wall was very accurately predicted by DEM, Figure 37a. Note that the friction between corn and the polycarbonate was calibrated as $\mu_{\text{pw}} = 0.26$ (Section 6.1.3). It is interesting to note that DEM predicted a sudden decrease in velocity at approximately -9°. This was also identified by PIV at the wall; however, the decrease was less severe. The sudden decrease in material velocity was due to the discontinuity in the surface gradient

created by successive flat polycarbonate panels, where the particles lost kinetic energy when impacting the following panel. This is further illustrated for V_b = 4 m/s (Figure 37b) where the material was longer in contact with the hood. The panel interfaces were positioned at 51°, 36°, 21°, 6° and -9° which correlated very well with the drop in material velocity identified in PIV and DEM. However, at θ = 51°, PIV identified a significant decrease and increase in velocity until the following panel interface was reached. The reason for this was that the material left the surface of the hood after the initial impact (see Figure 36b), consequently experiencing a considerable increase in velocity due to a combination of gravity and reduced particle-wall friction. DEM, unfortunately, could not identify the significant drop in velocity. However, DEM predicted a slight decrease in velocity between the point of impact and an angular position of approximately 20°, and then increased thereafter. The same observation was made by Ilic et al. (2007) where the material velocity through the hood de-accelerated immediately after first impact over a range of 20° to 25°.

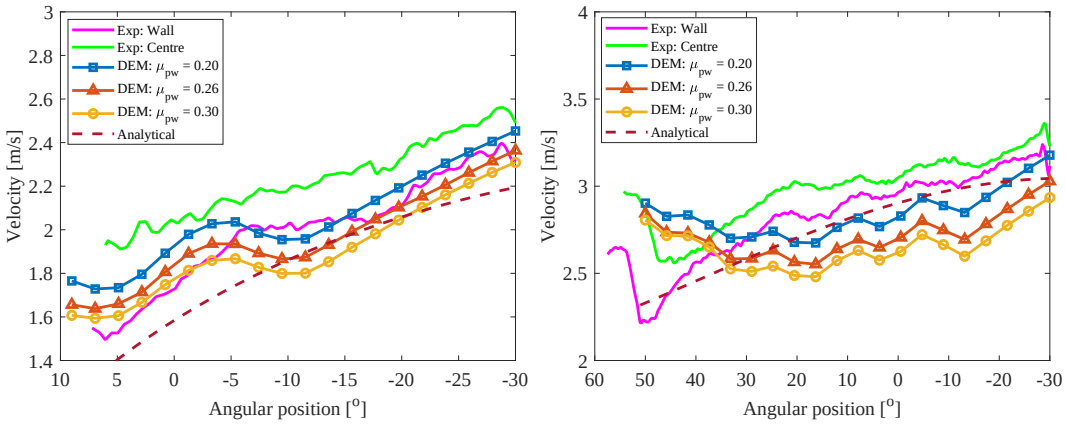

(a) V_b = 3 m/s. (b) V_b = 4 m/s.

Figure 37: Transfer hood velocity profile ($\dot{m}$ = 12 kg/s).

The velocity profile for mass flows of 4 kg/s, 8 kg/s and 12 kg/s at belt speeds of 3 m/s and 4 m/s is shown in Figures 38a and 38b, respectively. The results were all taken at the wall of the hood. For V_b = 3 m/s, DEM and PIV showed that the velocity directly after impact decreased with an increase in mass flow rate. Interestingly, DEM further predicted that the material velocity at the hood's exit was mass flow independent; however, this was not the case in the experiments where there was a general offset between the velocity profiles for the various mass flow rates. Furthermore, the DEM results at a belt speed of 4 m/s also showed good agreement with the experiments. Due to the impact position occurring on a hood panel which was more aligned with the trajectory stream (with V_b = 3 m/s, the impact position was between two panels), DEM and PIV showed that the mass flow rate had a negligible effect on the velocity directly after impact. Once again, DEM predicted that the velocity through the hood was mass flow independent; however, for this case, the same trend was shown by the measurements. The only

deviation in material velocity between the three mass flow rates was observed at the first corner (51°), which was caused by the majority of the particles hitting the following panel. As a result, a much lower velocity was observed at a mass flow rate of 4 kg/s.

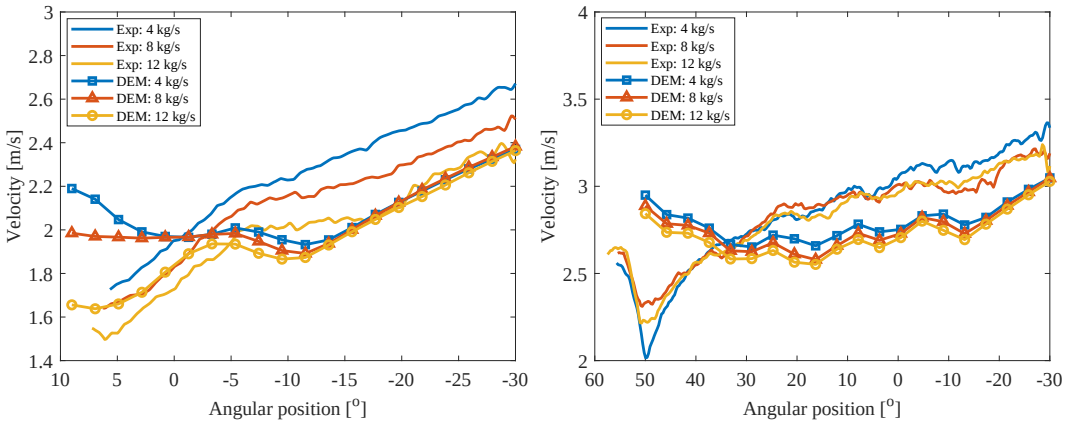

(a) $V_b = 3$ m/s. (b) $V_b = 4$ m/s.

Figure 38: Effect of the mass flow rate on the velocity profile at the wall (μ_{pw} = 0.26).

Figure 39a shows the measured stream thickness and DEM results. DEM predicted a slight decrease in the thickness as the material flowed along the hood. Furthermore, an increase in the particle-wall friction resulted in an increase in thickness, which was expected since higher friction caused the material to build-up more. The DEM results agreed well with the measurements between the angular positions of 43° and -1°. At the hood outlet, DEM predicted the smallest thickness, while in the experiments, the thickness first decreased, but then increased towards the hood exit.

The stream width was also measured on the hood using a GoPro Hero 3 camera pointed from behind the transparent hood, Figure 39c. Based on visual inspection, the stream spread out as the material flowed along the hood from the point of impact. The stream reached the full hood width at an angular position (Figure 34) between 21° and 29°. In DEM a similar analysis was performed, and the stream reached the full hood width between 20° and 25°. Furthermore, DEM showed that the particle-wall friction had no significant effect on the stream width, Figure 39b.

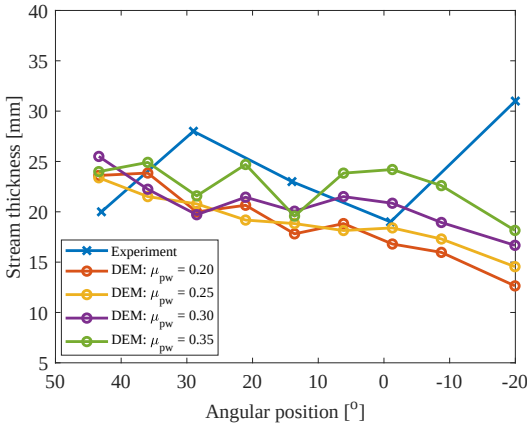

(a) Material stream thickness.

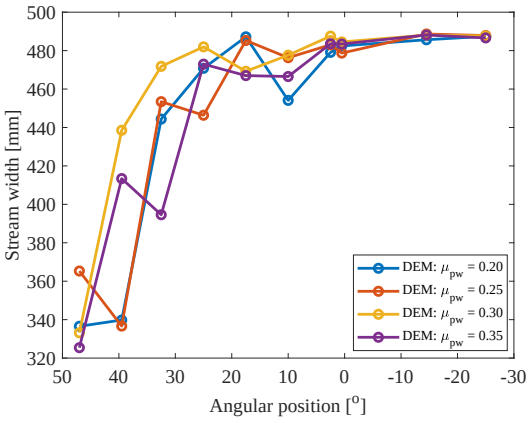

(b) Material stream width (DEM).

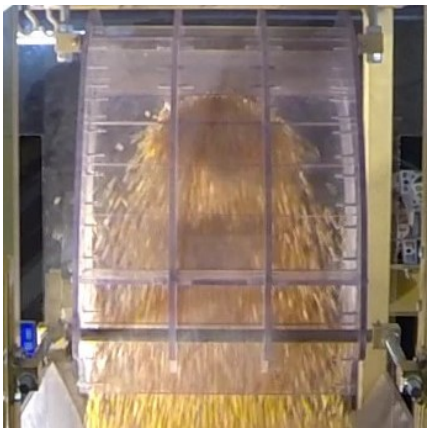

(c) GoPro image of material stream width.

Figure 39: Material stream (a) thickness and (b,c) width through the transfer hood ($V_b = 4$ m/s).

10 Rock Box Analysis

By successfully incorporating rock boxes in transfer chute designs, a major reduction in impact wear can be achieved. However, the location and arrangement of the rock box are fundamental to comply with the desired function of a transfer chute, i.e. to keep the mass flow rate constant and centrally load the material on the receiving conveyor since after the particle-particle impact, a considerable reduction in material velocity is evident (Scott and Choules, 1993). In this section, a detailed comparative study between DEM and high-speed footage is presented for the material flow in and from a rock box.

10.1 DEM Model of the Rock Box

The simulated rock box geometry and location in the transfer chute are shown in Figure 40a. The rock box consists of a small ledge, angled at 15°. A lip bar

(10 mm × 10 mm) was mounted at the end of the ledge to ensure a couple of layers of particles were entrapped. The recording of the particle position, velocity and acceleration were performed at 10 Hz. The parameter values used are presented in Table 4, and the simulations were performed for 5 s of simulation time (Appendix E).

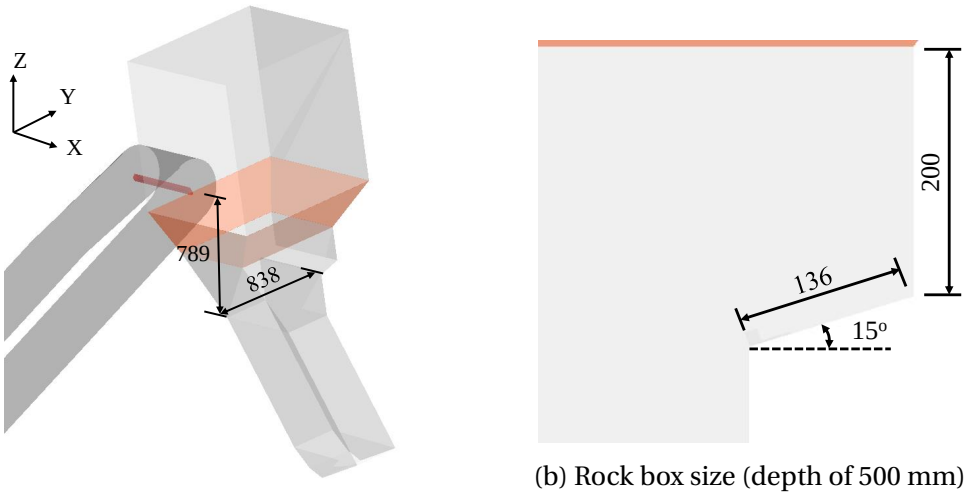

(a) Rock box geometry

(b) Rock box size (depth of 500 mm)

Figure 40: DEM model for the rock box analysis, dimensions in mm.

10.2 Rock Box Results and Discussion

Due to the position of the rock box, Figure 40a, the feeding conveyor was only set to a speed of 2 m/s, and mass flow rates were set to 4 kg/s, 8 kg/s and 12 kg/s. The material characteristics analysed included the material impact velocity V_i, angle α_i, slump/bed angle θ_{bed}, outflow velocity V_o, angle α_o and build-up H_b in the rock box, Figure 41a. The material slump angle θ_{bed} was defined as the angle which the particles made relative to the Y-axis, and was measured between the tip of the ledge and the start of the curved concave region of the bed which was approximately in the centre of the rock box. The material build-up height H_b was defined as the height which the centre of the bed reached against the back wall.

10.2.1 Material Flow Characteristics With Particle Friction and Damping Sensitivity (3-Clump Model)

Due to the chevron pattern on the conveyor belt, it was observed that the incoming stream's impact position varied and caused the material to build up against the back wall of the rock box. As a result, the material build-up height H_b also varied between successive patterns. From visual inspection (Figure 41), DEM could accurately predict these flow behaviours, at least qualitatively.

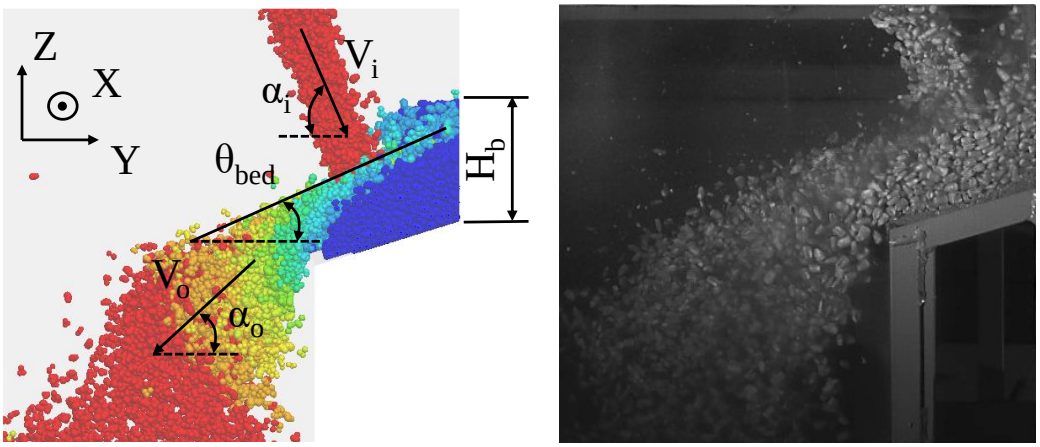

(a) DEM (3-clump particles). (b) High-speed image.

Figure 41: Rock box material flow between (a) DEM and (b) high-speed footage ($V_b = 2$ m/s and $\dot{m} = 12$ kg/s).

A summary of the measured flow characteristics is presented in Tables 18 and 19. These results showed that the mass flow rate had no significant influence on the incoming stream's velocity V_i or angle α_i. However, the mass flow rate significantly influenced the amount of material in the box at any given time, which influenced the slump angle θ_bed and material build-up height H_b, both increasing with an increase in mass flow rate. Interestingly, the material outflow velocity V_o was also influenced by the mass flow rate. This was caused by the increase in slump angle with more particles discharging with an increase in flow rate.

Table 18: Measured material impact velocity V_i, angle α_i, slump angle θ_bed and outflow velocity V_o from the rock box.

Mass flow [kg/s]	**Impact velocity, V_i [m/s]**			**Impact angle, α_i [°]**			**Slump angle, θ_bed [°]**			**Outflow velocity, V_o [m/s]**		
	Min	**Avg**	**Max**	**Min**	**Avg**	**Max**	**Min**	**Avg**	**Max**	**Min**	**Avg**	**Max**
4	3.88	4.26	5.12	62.4	64.2	66.1	17.9	23.8	29.5	1.18	1.29	1.41
8	3.94	4.26	4.96	62.5	64.6	66.0	19.0	26.9	33.1	1.27	1.35	1.45
12	3.85	4.29	5.08	62.9	63.9	65.1	21.4	31.0	35.2	1.34	1.41	1.50

Table 19: Measured material build-up height H_b from the rock box.

Mass flow [kg/s]	**Build-up, H_b [mm]**		
	Min	**Avg**	**Max**
4	26.6	51.3	87.9
8	45.1	68.7	99.9
12	55.1	75.3	101.9

For the DEM simulations, the particle sliding friction μ_pp and contact damping ζ_pp values were varied between 0.10 and 0.40. The calibrated μ_pp and ζ_pp of 0.15

and 0.14, respectively, were also simulated, Table 20. It is clear that DEM also predicted that the mass flow rate had no significant effect on the impact velocity or angle, and compared very well to the experimental results. Moreover, these measures were insensitive to the μ_{pp} and ζ_{pp} parameters. The trend in the slump angle and material outflow velocity results also correlated well to the the experimental results where it was found that the slump angle and outflow velocity increased for an increase in mass flow rate. However, the results showed that the slump angle was sensitive to the particle sliding friction, and for μ_{pp} equal to 0.40, θ_{bed} was significantly overestimated (error of 27 % to 42 %). Furthermore, the θ_{bed} angles predicted by the calibrated $\mu_{pp} = 0.15$ agreed very well with the experimental results ($|error| \leq 6.30$ %). It is interesting to note that for larger μ_{pp} values, the slump angle was less sensitive to the mass flow rate, contrary to the experimental results, indicating that these high friction values cannot accurately model the flow mechanism. The material outflow velocity was very well predicted by DEM for all simulated combinations ($|error| \leq 10.64$ %); however, it was noted that a few combinations failed to satisfy the 10 % accuracy limit at certain flow rates. These results were still, however, considered to be accurate enough since the error was just above 10 %, and if these simulations were to be executed again, the random effects associated with discrete systems, could result in errors just below 10 %.

The minimum, average and maximum build-up height H_b results are shown in Figure 42. A box-and-whisker plot was used to present the simulation results and to indicate the variation in H_b over the simulated time. From all three plots for the various mass flow rates, it is clear that the lower the mass flow rate, the more variation in H_b was found, with the minimum and maximum further apart and a larger interquartile range (IQR). For $\dot{m} = 4$ kg/s, the build-up was very well predicted by DEM and the IQR fell between the upper and lower bounds of the measured H_b. The two calibrated $\mu_{pp} = 0.15$ combinations with ζ_{pp} equal to 0.14 and 0.40 respectively, were the only combinations which captured the average measured H_b within the IQR. The simulation results for $\dot{m} = 8$ kg/s showed less accurate results where all the IQR's were above the measured average, but below the maximum. The predicted H_b for $\dot{m} = 12$ kg/s showed the least accurate results and the IQR's fell on or just above the experimental upper bound. The combination for $\mu_{pp} = 0.40$ overestimated the build-up completely and the predicted minimum was at the maximum measured H_b.

The material outflow angle α_o is the angle with which the material discharged from the rock box, Figure 41a. It was found that the discharge angle of the particles varied significantly across the outflow stream, where the particles at the top of the rock box discharged at a relatively low angle and the bottom particles at a much larger angle. Therefore, the material discharge angle was evaluated between the upper and lower bounds of the discharge stream, along a line perpendicular to the flow at the centre of the stream. The simulation and PIV results are

shown in Figure 43, where the starting position was at the upper bound. It is clear that μ_{pp} and ζ_{pp} only affected the trajectory angle of the upper part of the stream, which was expected since the material in the lower part of the rock box only free-falls once the material flowed over the lip bar. However, in the upper part of the stream, more dynamic flow and particle collisions were observed which were influenced by the particle-particle parameters. The results further showed that the particle sliding friction had a significant effect on the material flow where a larger discharge angle, i.e. more downwards trajectory, was observed for an increase in μ_{pp}. The particle damping, however, also influenced the discharge angle but to a lesser extent. Furthermore, the DEM results for low particle sliding friction values, i.e. 0.15 and 0.10, correlated very well with the PIV results, but $\mu_{pp} = 0.40$ predicted a significantly lower trajectory.

Table 20: Rock box material flow characteristics measured in DEM for various combinations of μ_{pp} and ζ_{pp}.

μ_{pp}	ζ_{pp}	Mass flow [kg/s]	Impact velocity, V_i [m/s]	Compared to* measurements	Impact angle, α_i [°]	Compared to* measurements
0.10	0.14	4	4.43	3.99 %	64.7	0.78 %
		8	4.43	3.99 %	64.8	0.31 %
		12	4.40	2.56 %	64.8	1.41 %
0.15	0.10	4	4.43	3.99 %	64.2	0.00 %
		8	4.44	4.23 %	64.8	0.31 %
		12	4.44	3.50 %	64.9	1.56 %
0.15	0.14	4	4.43	3.99 %	64.6	0.62 %
		8	4.44	4.23 %	64.9	0.46 %
		12	4.45	3.73 %	65.0	1.72 %
0.15	0.40	4	4.44	4.23 %	64.8	0.93 %
		8	4.45	4.46 %	64.9	0.46 %
		12	4.45	3.73 %	65.0	1.72 %
0.40	0.14	4	4.44	4.23 %	64.5	0.47 %
		8	4.45	4.46 %	64.7	0.15 %
		12	4.42	3.03 %	64.7	1.25 %
			Slump angle, θ_{bed} [°]	Compared to* measurements	Outflow velocity, V_o [m/s]	Compared to* measurements
0.10	0.14	4	20.1	-15.55 %	1.20	-6.98 %
		8	28.5	5.95 %	1.32	-2.22 %
		12	41.4	33.55 %	1.43	1.42 %
0.15	0.10	4	21.0	-11.76 %	1.19	-7.75 %
		8	27.7	2.97 %	1.33	-1.48 %
		12	30.3	-2.26 %	1.49	5.67 %
0.15	0.14	4	22.3	-6.30 %	1.16	-10.08 %
		8	28.0	4.09 %	1.33	-1.48 %
		12	29.5	-4.84 %	1.48	4.96 %
0.15	0.40	4	24.3	2.10 %	1.16	-10.08 %
		8	27.3	1.49 %	1.28	-5.19 %
		12	29.5	-4.84 %	1.43	1.42 %
0.40	0.14	4	33.9	42.44 %	1.26	-2.33 %
		8	38.3	42.38 %	1.44	6.67 %
		12	39.4	27.10 %	1.56	10.64 %

*The percentage error was calculated by comparing the DEM results to the PIV results.

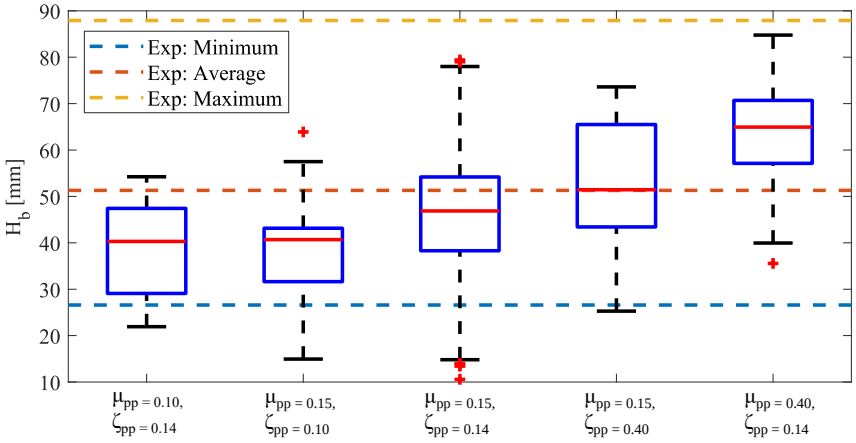

(a) $\dot{m} = 4$ kg/s.

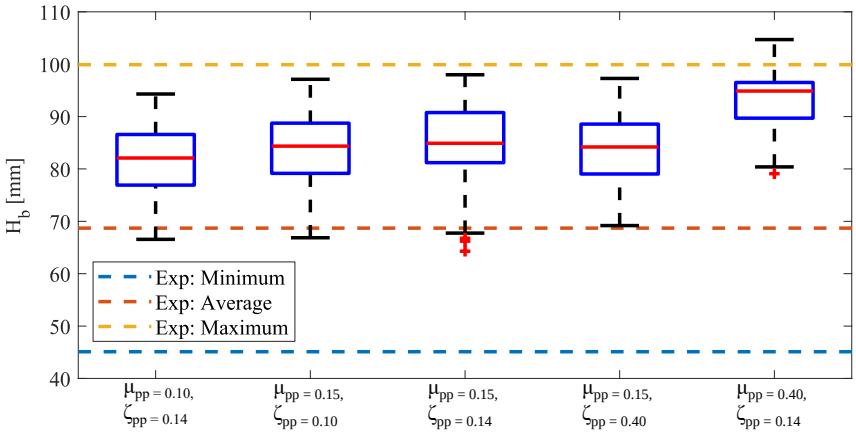

(b) $\dot{m} = 8$ kg/s.

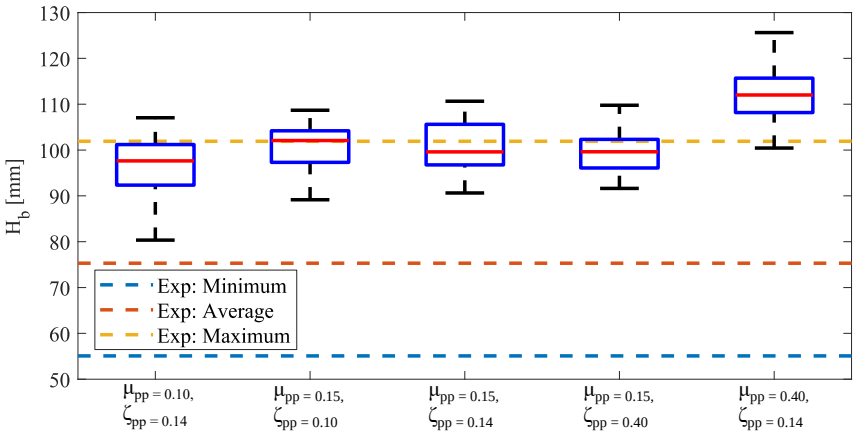

(c) $\dot{m} = 12$ kg/s.

Figure 42: Measured and predicted build-up height H_b for various combinations of μ_{pp} and ζ_{pp}.

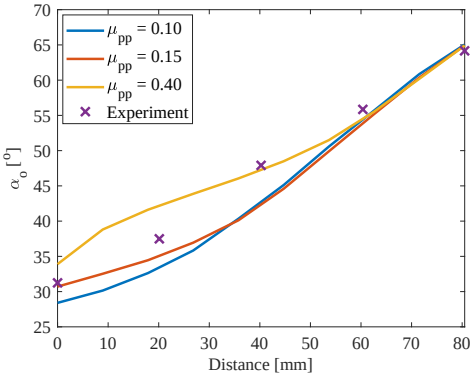

(a) Influence of μ_{pp} ($\dot{m}$ = 8 kg/s and ζ_{pp} = 0.14).

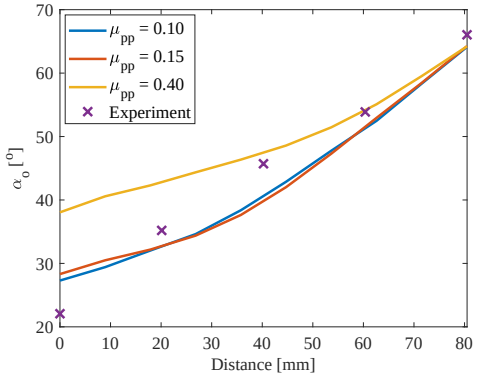

(b) Influence of μ_{pp} ($\dot{m}$ = 12 kg/s and ζ_{pp} = 0.14).

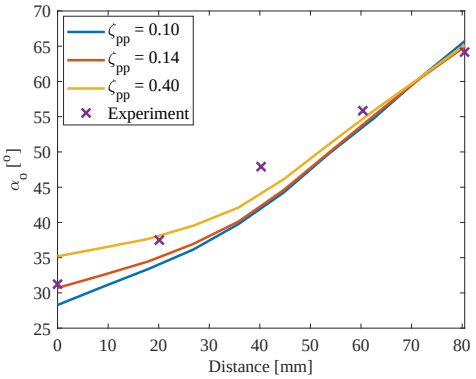

(c) Influence of ζ_{pp} ($\dot{m}$ = 8 kg/s and μ_{pp} = 0.15).

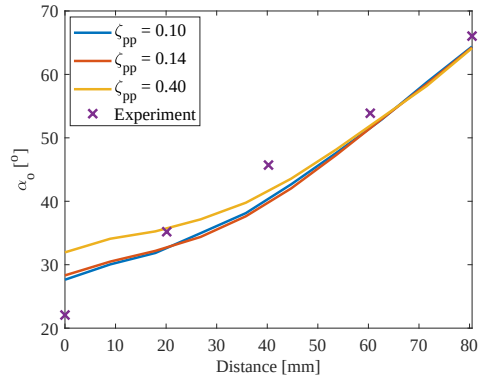

(d) Influence of ζ_{pp} ($\dot{m}$ = 12 kg/s and μ_{pp} = 0.15).

Figure 43: Measured and predicted material outflow angle α_o from the rock box.

The profile which the material made against the back wall of the rock box was evaluated in DEM and compared to measurements, Figure 44. Also, due to the varying material height in the rock box, the average material profile over the simulated time is presented. It is once again noticed that the particle sliding friction had the most significant effect on the material flow while the particle damping had little to no effect. From Figures 44a and 44b, it is clear that the combination for μ_{pp} = 0.40 predicted a significantly higher profile and failed to identify the two lower regions, left and right of the centre. Based on the high-speed footage, it was observed that these lower regions were created by the rolling and sliding of the particles, away from the centre, when the incoming stream's point of impact was closest to the back wall (due to the chevron pattern). For lower particle frictions, DEM could accurately predict this phenomenon; however, it failed to accurately predict the depth and size of the lower regions. In terms of the two mass flow rates, the results correlated well with the experimental results for the material build-up height in Figure 42 where it was found that DEM overestimated the material height for larger mass flow rates. Regardless of these findings, it is concluded that DEM accurately predicted the material height at the sides of the rock box.

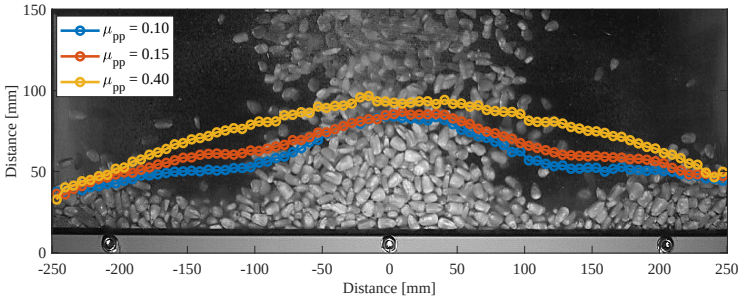

(a) Influence of μ_{pp} ($\dot{m} = 8$ kg/s and $\zeta_{pp} = 0.14$).

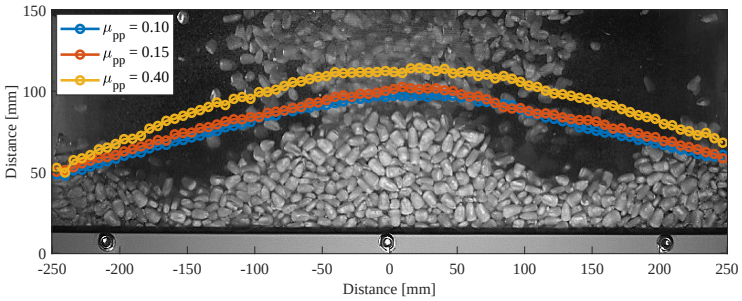

(b) Influence of μ_{pp} ($\dot{m} = 12$ kg/s and $\zeta_{pp} = 0.14$).

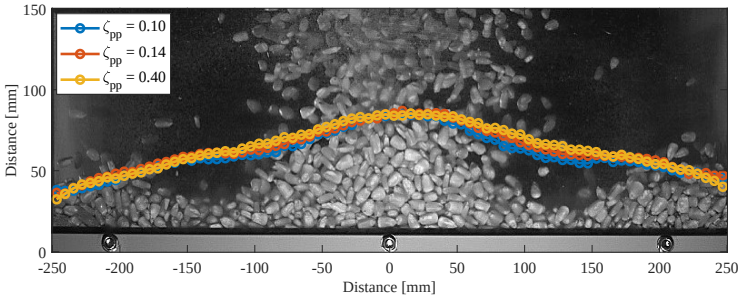

(c) Influence of ζ_{pp} ($\dot{m} = 8$ kg/s and $\mu_{pp} = 0.15$).

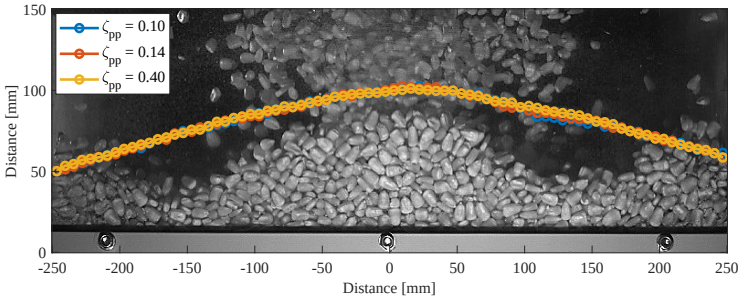

(d) Influence of ζ_{pp} ($\dot{m} = 12$ kg/s and $\mu_{pp} = 0.15$).

Figure 44: Material profile comparison between DEM and high-speed footage.

Figure 45 compares the experimental and predicted bed profile in the rock box, seen from the side (perpendicular to the flow trajectory). According to Scott and Choules (1993), the material's free surface often takes the form of multiple concave surfaces. Also, the shape and inclination of the surface depend on the particles' shape and size, material's cohesiveness and internal friction characteristics. It is clear from the high-speed footage and DEM results that the material sur-

face indeed consisted of multiple concave surfaces. Furthermore, an increase in particle sliding friction caused the start of the second concave surface to shift towards the back of the rock box. By visually evaluating Figures 45a and 45b for the influence of μ_{pp}, the material bed profile for $\mu_{pp} = 0.15$ was the most accurate. The results further showed that the particle damping did not significantly influence the bed profile.

From all the simulation results presented in this section, the particle damping parameter, ζ_{pp}, had little to no influence on the bulk material behaviour in the rock box. A similar conclusion was made by Coetzee (2019) where the contact damping had no significant effect on the dynamic angle of repose. Grima and Wypych (2011) implemented a swing-arm slump test (angle of repose) to calibrate the rolling friction coefficient. They found that the pile profile was insensitive to the damping coefficient and as a result, could not be used to calibrate ζ_{pp}.

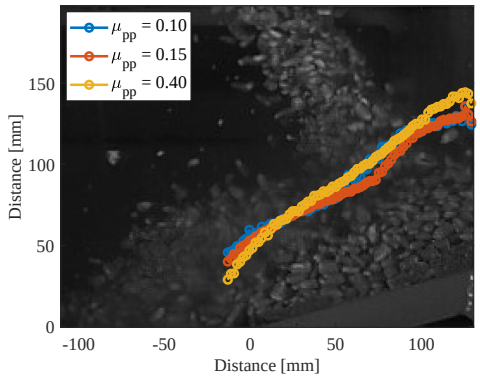

(a) Influence of μ_{pp} ($\dot{m} = 8$ kg/s and $\zeta_{pp} = 0.14$).

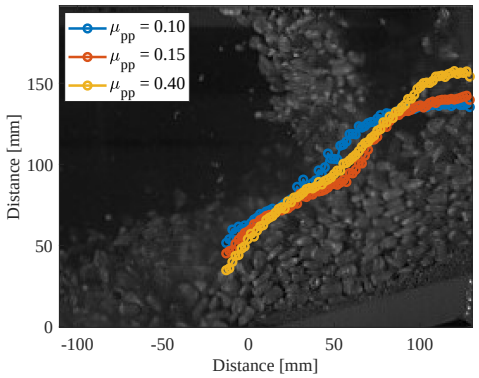

(b) Influence of μ_{pp} ($\dot{m} = 12$ kg/s and $\zeta_{pp} = 0.14$).

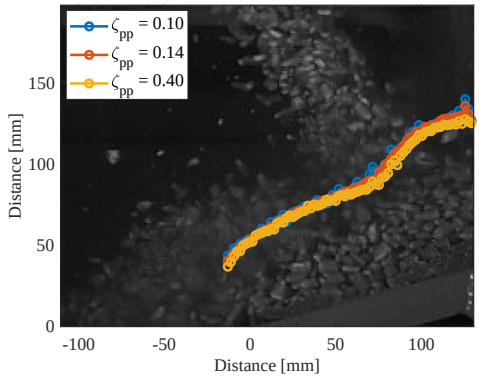

(c) Influence of ζ_{pp} ($\dot{m} = 8$ kg/s and $\mu_{pp} = 0.15$).

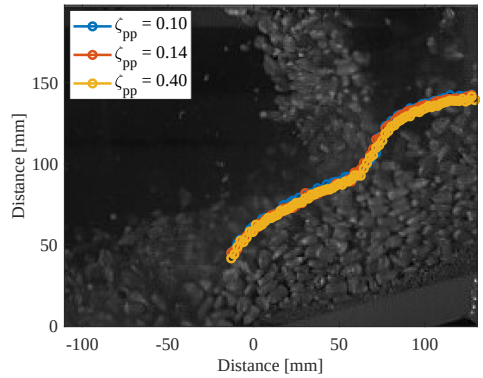

(d) Influence of ζ_{pp} ($\dot{m} = 12$ kg/s and $\mu_{pp} = 0.15$).

Figure 45: Material bed profile comparison between DEM and high-speed footage.

10.2.2 Particle Scale (3-Clump Model)

In this section, the maximum scaling factor of the 3-clump particles was investigated by comparing the material flow characteristics to the DEM results for the unscaled particles and the experimental results. The calibrated particle friction and damping combination of $\mu_{pp} = 0.15$ and $\zeta_{pp} = 0.14$ was used. Figure 46 shows the predicted material build-up height H_b by the scaled particles. It is clear that the build-up decreased with an increase in the scaling factor, and the interquartile ranges also increased (i.e. more variation). Based on these results, it is concluded that the 3-clumps can be scaled by a maximum factor of 1.8 and still accurately predict the material build-up. Larger scaling factors would produce inaccurate results. Note that, when using the average particle size of approximately 8.50 mm (7.50 mm $\leq D_{ev} \leq$ 9.60 mm), the average build-up height is the equivalent of approximately 9 particles. Using a scale factor of 1.8, the build-up height is the equivalent of approximately 5 particles, which is the limit to allow for particle build-up.

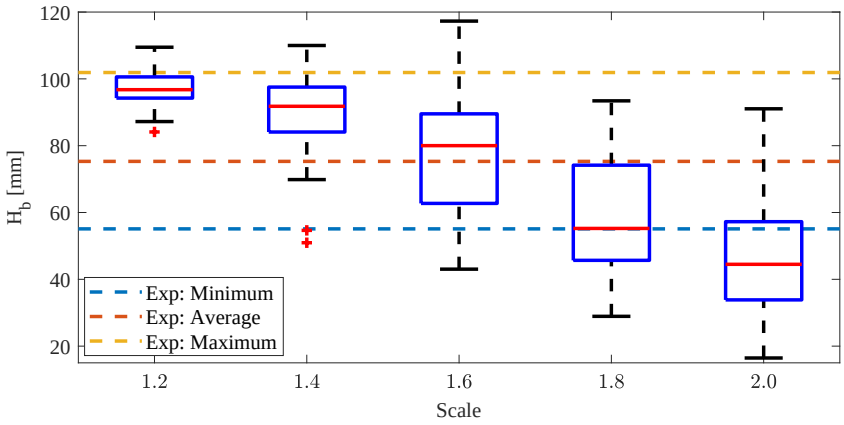

Figure 46: Predicted material build-up height H_b by scaled 3-clump particles ($\dot{m} = 12$ kg/s).

Table 21 shows the DEM results for the material impact velocity, angle, slump angle and outflow velocity obtained by the various particle scaling factors. The scaling did not significantly influence the impact velocity, angle or outflow velocity, and only a slight decrease in the material outflow velocity was predicted. However, the scaling had a significant effect on the slump angle where it was observed that θ_{bed} increased with an increase in particle size. Compared to the experimental results, scaling factors up to and including 1.6 predicted accurate slump angles (error $\leq$ 10 %).

Table 21: Rock box material flow characteristics for scaled 3-clump model ($\dot{m}$ = 12 kg/s).

Scale	Impact velocity, V_i [m/s]	Compared to* 3-clump model	Compared to** measurements	Impact angle, α_i [°]	Compared to* 3-clump model	Compared to** measurements
1.2	4.45	0 %	3.73 %	64.9	-0.15 %	1.56 %
1.4	4.46	0.22 %	3.96 %	64.9	-0.15 %	1.56 %
1.6	4.46	0.22 %	3.96 %	64.7	-0.46 %	1.25 %
1.8	4.46	0.22 %	3.96 %	64.7	-0.46 %	1.25 %
2.0	4.46	0.22 %	3.96 %	64.7	-0.46 %	1.25 %
	Slump angle, θ_{bed} [°]	**Compared to* 3-clump model**	**Compared to** measurements**	**Outflow velocity, V_o [m/s]**	**Compared to* 3-clump model**	**Compared to** measurements**
1.2	32.6	10.51 %	5.16 %	1.45	-2.03 %	2.84 %
1.4	33.5	19.64 %	8.06 %	1.42	6.77 %	0.71 %
1.6	33.8	14.58 %	9.03 %	1.41	-4.73 %	0 %
1.8	36.1	22.37 %	16.45 %	1.39	-6.08 %	-1.42 %
2.0	35.6	20.68 %	14.84 %	1.38	-6.76 %	-2.13 %

The percentage error was calculated by comparing the results of the scaled particles to the results for a *scale factor of 1 and the **experimental tests.

The DEM results for the material outflow angle, Figure 47a, showed an increase in α_o for the upper material stream with an increase in the particle scaling factor. Moreover, although the upper stream's trajectory was slightly lower, no difference in the outflow angle was found for the lower material stream. The scaling factor had no effect on the length of the first part of the multiple concave surfaces, Figure 47b, and only a decrease in the profile height against the rear wall was predicted, as seen in Figure 47c. This is in accordance with the results for the material build-up height shown in Figure 46. The material height against the sides of the rock box remained mostly unchanged for all scale factors.

Although a scale factor 1.8 produced accurate results in predicting the build-up height H_b, accurate modelling of the slump angle, limited the scale factor to 1.6. It is thus concluded, that for this rock box and the corn particles, the maximum scale factor is 1.6 to accurately model all the flow characteristics. However, further investigation should be done to determine the maximum ratio of particle size to rock box size for accurate predictions. With a scale factor of 1, the footprint size of the box (136 mm × 500 mm, Figure 40b) is equivalent to approximately 16 × 59 particles, and for a scaling factor of 1.6 it is 10 × 37 particles. These results correspond with the general assumption that wall or boundary effects can be eliminated or ignored if the ratio of the container size to particle size is larger than approximately 8 to 10 (Nakao and Fityus, 2008).

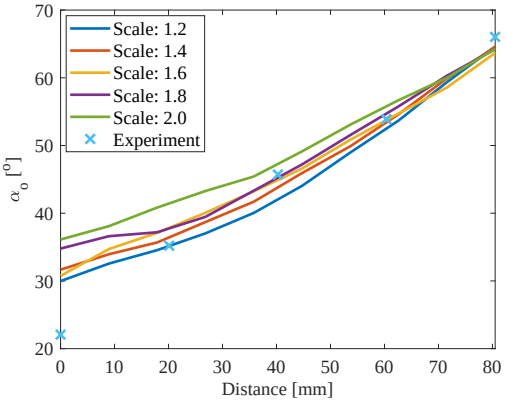

(a) Outflow angle.

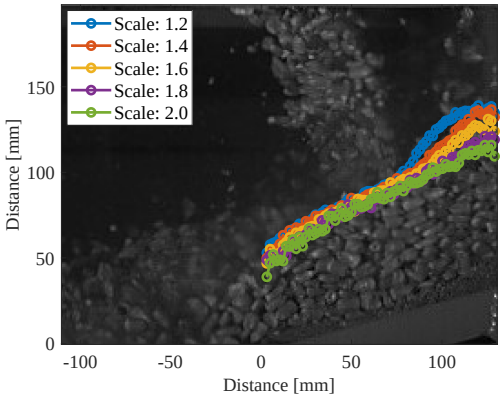

(b) Bed profile.

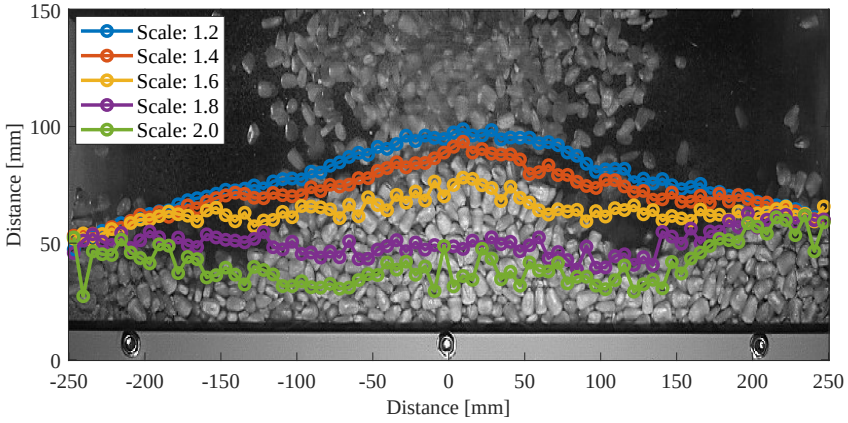

(c) Material profile.

Figure 47: Predicted (a) material outflow angle, (b) bed profile and (c) material profile against the rock box's rear wall by the scaled particles ($\dot{m}$ = 12 kg/s).

10.2.3 Effect of Particle Shape

10.2.3.1 Balls

The use of ball particles to predict the material flow in and from the rock box was investigated. The inter-particle sliding and rolling friction parameters were once again selected from the feasible region obtained by Coetzee (2020), which is shown in Figure 14a. In addition, the calibrated $\mu_{\mathrm{pp}} = 0.25$ and $\mu_{\mathrm{r\,pp}} = 0.50$ from Section 8.3.3.2 for the angled impact plate analysis was also considered. The DEM results for the material build-up height on the rear wall of the rock box is presented in Figure 48. The parameter combinations proposed by Coetzee (2020), showed acceptable results and all three combinations predicted H_{b} to be mostly in the upper region of the measured height. Comparing these results to the results obtained by the 3-clump particles, Figure 42b, no significant difference was observed. The calibrated combination from the impact plate analysis showed very good agreement with the experimental results. The minimum and maximum H_{b} compared very well, and the interquartile range also spanned the

average measured H_b.

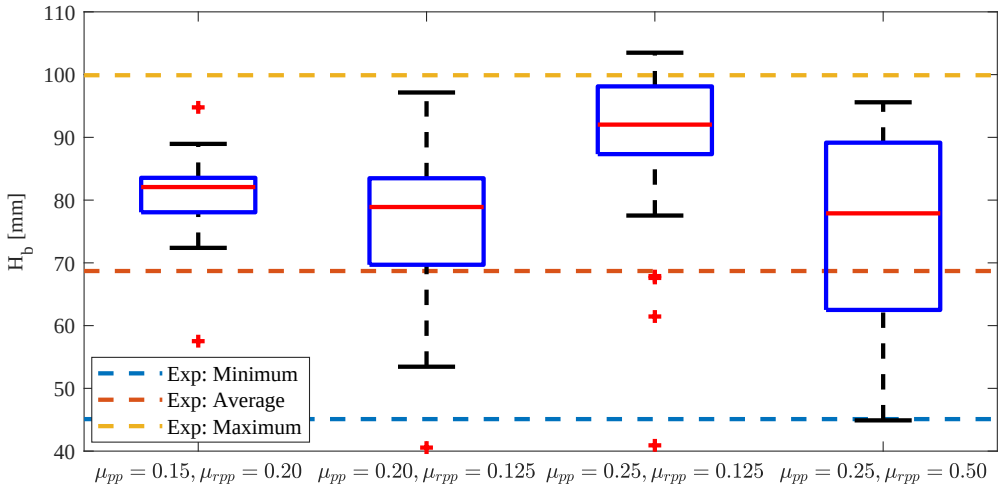

Figure 48: Predicted material build-up height H_b by ball particles ($\dot{m} = 8$ kg/s).

The material flow characteristics are summarised in Table 22. The particle shape and inter-particle parameters had no or a negligible effect on the material impact velocity V_i, angle α_i and outflow velocity V_o where the results for all three flow mechanisms agreed well to the 3-clump and experimental results. A discrepancy was, however, found for the material slump angle θ_{bed}. It is interesting to note that the slump angle decreased with an increase in particle friction for the ball particles, while an increase was observed for the 3-clump particles (see Table 20). Furthermore, it was found that the combination for $\mu_{pp} = 0.25$ and $\mu_{r\,pp} = 0.125$ was the only combination from the feasible region which accurately predicted the slump angle. The impact plate calibrated parameters, $\mu_{pp} = 0.25$ and $\mu_{r\,pp} = 0.50$, accurately predicted the slump angle and also compared very well to the angle predicted by the 3-clump particles. The predicted material outflow velocity decreased with an increase in particle friction. Nonetheless, all the combinations still accurately predicted the measured outflow velocity (error $\leq$ 10 %), while impact plate calibrated combination was the most accurate.

Table 22: Rock box material flow characteristics obtained by the ball particles for various combinations of μ_{pp} and $\mu_{r\,pp}$ ($\dot{m} = 8$ kg/s).

μ_{pp}	$\mu_{r\,pp}$	**Impact velocity, V_i [m/s]**	**Compared to* 3-clump model**	**Compared to** measurements**	**Impact angle, α_i [°]**	**Compared to* 3-clump model**	**Compared to** measurements**
0.15	0.20	4.44	0 %	4.23 %	65.0	0.15 %	0.62 %
0.20	0.125	4.44	0 %	4.23 %	65.0	0.15 %	0.62 %
0.25	0.125	4.45	0.23 %	4.46 %	64.8	-0.15 %	0.31 %
0.25	0.50	4.47	0.68 %	4.93 %	64.3	-0.92 %	-0.46 %
		Slump angle, θ_{bed} [°]	**Compared to* 3-clump model**	**Compared to** measurements**	**Outflow velocity, V_o [m/s]**	**Compared to* 3-clump model**	**Compared to** measurements**
0.15	0.20	45.1	61.07 %	67.66 %	1.45	9.02 %	7.41 %
0.20	0.125	35.4	26.43 %	31.60 %	1.43	7.52 %	5.93 %
0.25	0.125	28.6	2.14 %	6.32 %	1.42	6.77 %	5.19 %
0.25	0.50	27.1	-3.21 %	0.74 %	1.36	2.26 %	0.74 %

The percentage error was calculated by comparing the ball particles results to the results of the *3-clump particles ($\mu_{pp} = 0.15$, $\zeta_{pp} = 0.14$) and **experimental tests.

Figure 49a shows the simulation results for the material outflow angle α_o. The three feasible region parameter combinations predicted a much lower outflow angle, showing an approximately 6° offset relative to the experimental results. The angle was, however, successfully predicted by the impact plate calibrated combination. This shows that the particle rolling friction had a significant effect on the material bulk behaviour.

The material bed profile predicted by the ball particles is shown in Figure 49b, and it also predicted the impact surface to have multiple concave surfaces. The bed profile was particle sliding and rolling friction sensitive, where the start of the second concave surface shifted to the rear wall with an increase in μ_{pp} and $\mu_{r\,pp}$.

Figure 49 shows the predicted material profile against the back wall by the ball particles. Compared to the 3-clump particles, the ball particles were more successful in predicting the two lower regions, left and right of the incoming stream. However, it also failed to accurately predict the size of the lower regions.

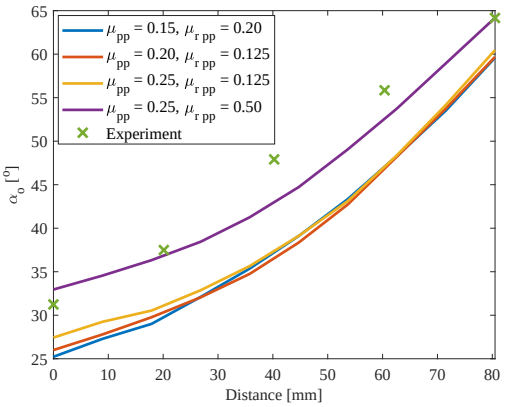

(a) Outflow angle.

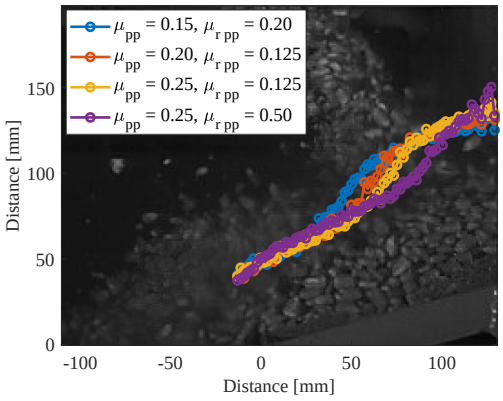

(b) Bed profile.

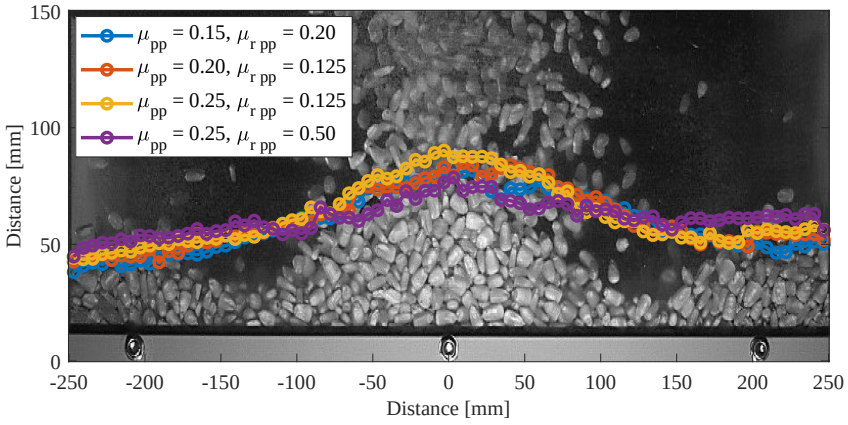

(c) Material profile.

Figure 49: Predicted (a) material outflow angle, (b) bed profile and (c) material profile against the rock box's rear wall by the ball particles ($\dot{m} = 8$ kg/s).

11 Transfer Chute Flow and Build-Up Analysis

Transfer chutes usually clog up due to poor designing and controllability of the conveyor (feeding and receiving) speeds. An effective transfer chute design minimises the differential velocity between the material loading velocity and receiving conveyor speed, while also minimising wear in the chute and on the loading conveyor belt (Benjamin, 1999). In this section, the material build-up in and from a chute is evaluated by comparing high-speed footage to the results of the DEM model.

11.1 DEM Model of the Transfer Chute

Figure 50 shows the transfer chute and feeder used to simulate a chute blockage. The chute was located between conveyor 1 and 2, having an inlet opening of 480 mm × 396 mm, outlet of 300 mm × 396 mm and a total height of 845 mm. Due to the outlet's large opening and relatively small particles, the length of the outlet was decreased to 80 mm by inserting a Perspex sheet across the width of the chute. For the material build-up phase, the mass flow rate was set to 20 kg/s and the feeding and receiving conveyor speed to 4 m/s and 0.5 m/s, respectively. Once the material reached a height of 500 mm relative to the outlet of the chute, the feeding mass was switched off and the receiving conveyor's speed was increased to 3 m/s (discharge phase). The feeding conveyor was simulated with the clump acceleration method and the receiving conveyor with the chevron patterns. The recording of the particle position, velocity and acceleration were performed at 10 Hz, and the parameter values used are shown in Table 4.

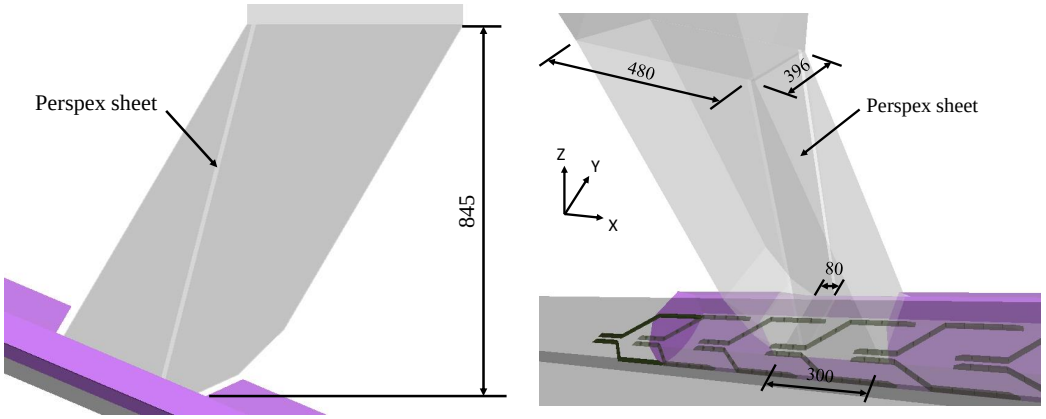

(a) Side view.

(b) 3-D view.

Figure 50: (a) Side and (b) 3-D view of the DEM model for the transfer chute analysis, dimensions in mm.

11.2 Transfer Chute Build-Up Results and Discussion

11.2.1 Build-Up and Discharge Mass Flow Rate (3-Clump Model)

The predicted and recorded material build-up is shown in Figures 51a and 51b, respectively. From visual inspection, the material's free surface was accurately predicted by DEM.

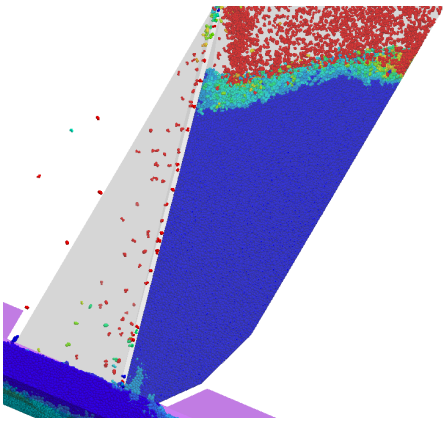

(a) DEM (3-clump particles).

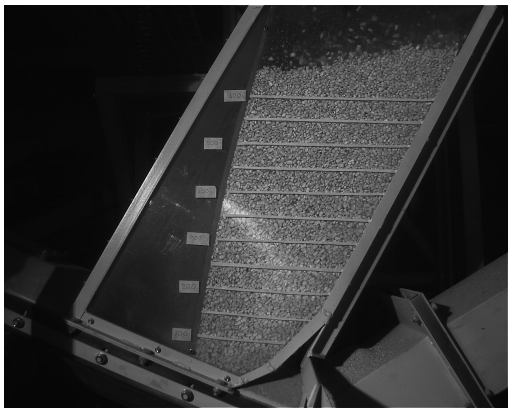

(b) High-speed image.

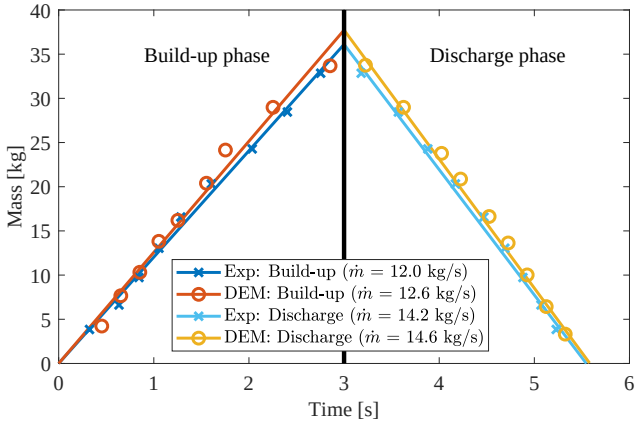

(c) Material build-up and discharge mass flow rate.

Figure 51: Transfer chute material flow between (a) DEM and (b) high-speed footage, and (c) mass flow rate results.

The tempo with which the material builds up and discharges from a transfer chute was investigated using 3-clump particles with a scale factor of 1. The material flow tempo in terms of the fill height was calculated from high-speed footage using level markings. It was assumed that the fill height was at the lowest part of the material's free surface, and converted to a mass using the material volume and the measured bulk density, 824.73 kg/m^3 (Section 6.1.4). Figure 51c shows the measured and predicted mass inside the chute during both phases. As reference, the material mass was approximately 3.9 kg at a fill height of 100 mm and 32.8 kg at 500 mm. A straight line was fitted to the measured data points of each

phase, and the mass flow rate calculated as 12.0 kg/s (R^2 = 0.995) and 14.2 kg/s (R^2 = 0.995), respectively. A similar approach was used in the DEM model, which accurately predicted the flow rate for both phases with relative errors of 5.00 % for the build-up and 2.82 % for the discharge phase. However, in the DEM model, the actual mass of the particles in the filled volume was determined and it was observed that the bulk density increased with an increase in material height. This was due to an increase in pressure, creating larger overlaps between the particles. At a fill height of 500 mm, the mass was calculated as 37.6 kg, increasing the bulk density to 944.1 kg/m^3 This is, however, not unique to the DEM model, and there was also some consolidation during the experiments, which could not be quantified. Nevertheless, users should be careful when selecting the particle stiffness to simulate chute blockages.

11.2.2 Particle Scale (3-Clump Model)

The maximum scale factor of the 3-clump particles was identified by comparing the flow rates of the scaled particles to the results of the unscaled particles and the experiments, Table 23. As expected, the DEM results showed a decrease in the flow rate with an increase in the scale factor. The maximum scaling factor was 1.6 where the mass flow rate for the build-up and discharge phase was underestimated by 9.17 % and 5.63 %, respectively. The results further showed that the material mass at a fill height of 500 mm increased with an increase in the scale factor; hence, increasing the bulk density (decreasing the porosity) due to larger overlap between the heavier particles.

The simulation for a particle scale of 1.4 was repeated, however, without the chevron pattern on the receiving belt. The results showed that the build-up started approximately 1 s later and as a result, the mass flow rate during the build-up phase was also lower, but did, however, still compare relatively well to the measurements (-10.00 % error). For the discharge phase, no significant difference in the mass flow rate was observed (1.41 % error).

Table 23: Predicted mass flow rate in and from the chute by scaled 3-clump particles.

Scale	Build-up phase			Discharge phase			True mass at	Time to
	$\dot{m}$ [kg/s]*		R^2	$\dot{m}$ [kg/s]*		R^2	500 mm [kg]	build-up [s]
1.0	12.6	5.00 %	0.982	14.6	2.82 %	0.995	37.6	6.5
1.4	12.9	7.50 %	0.992	14.2	0 %	0.999	39.9	6.5
1.4**	10.8	-10.00 %	0.956	14.4	1.41 %	0.999	39.9	7.5
1.6	10.9	-9.17 %	0.983	13.4	-5.63 %	0.998	40.4	6.5
1.7	9.3	-22.50 %	0.964	12.6	-11.27 %	0.996	41.1	6.1
1.8	9.1	-24.17 %	0.972	12.3	-13.38 %	0.998	41.4	6.1
2.2	10.6	-11.67 %	0.981	12.4	-12.68 %	0.999	42.0	5.8
2.4	9.4	-21.67 %	0.988	11.7	-17.61 %	0.999	42.3	5.4

*The percentage error of the mass flow rates was calculated by comparing it to the experimental results.
**The chevron pattern was neglected on the receiving belt.

12 Conclusion

There is an increase in the industrial demand for using DEM to improve conveyor system designs. The main cause for production delays is transfer point issues, causing spillage, blockages, dust emissions and wear. In industry, it is often the case that the careful design of transfer points is overlooked, or neglected. In this study, the accuracy with which DEM can predict the flow of a non-cohesive granular material through transfer chute components such as an impact plate, hood, rock box and chute was investigated. The DEM models were validated by comparing the results to that of analytical models and experimental measurements, including particle image velocimetry (PIV). As a result, this leads to a better understanding of how to model granular materials (dry) and to use numerical modelling to possibly optimise transfer chute designs.

Corn grains were modelled as single and multi-sphere (clumps) particles. The clump models consisted of 3, 5, and 10 sub-spheres, providing a more accurate representation of the particle's non-spherical nature. The model parameter values were obtained from various experimental tests, followed by a sensitivity study.

Two models were developed for the chevron patterned conveyor belts used in the experiments, i.e. an accurate pattern model and a clump acceleration model. In the pattern model, the chevron geometry was imported and slaved to the surface velocity of the belt, resulting in the pattern closely following the belt geometry in the transition-zone and around the head pulley. The clump acceleration model was an alternative model which neglected the chevron geometry completely to reduce computation time This approach, however, compensated for the influence of the chevron pattern, by accelerating the particles at the end of the transition-zone.

The material flow onto an impact plate was investigated for the case where the plate was vertical and angled (30° and 45°). DEM accurately predicted the impact force (|error| ≤ 8.57 %), force frequencies (-1 % error), velocity (|error| ≤ 5.31 %), angle (|error| ≤ 14.82 %), after-impact velocity (|error| ≤ 19.90%), material width (|error| ≤ 30.10 %) and build-up height (|error| ≤ 17.44 %) on the vertical plate. The particle-wall damping ratio had no significant effect on the results; however, a decrease in particle-particle damping resulted in a decrease in the impact forces and a large number of particles deviated from the mainstream. The stiffness of all contacts was scaled up by factors of 10 and 100 and the results showed that the impact forces were insensitive to this parameter. Similarly, the reaction forces, impact and after-impact velocity were not sensitive to the particle-particle friction coefficient. Furthermore, it was found that the particles could be scaled up by a factor of 9 and still accurately predict the average impact forces; however, only scaling factors up to 7 could accurately predict the force

frequency content. The more accurate particle shapes (5- and 10-clump, versus the 3-clump models) had no significant effect on the average reaction forces or other flow features. These particles did, however, predict slightly lower peak forces, which were more accurate compared to the measurements. Therefore, it is concluded that if the frequency content of the impact force is important (for predicting wear for example), more accurate particles shapes will provide more accurate results, however, if only the average impact force is of interest, all particle shapes (clumps and balls) will provide accurate results. The results for the ball particles, however, showed that the material flow was very sensitive to the particle sliding and rolling friction coefficients, and an appropriate combination of these two parameter values should be used.

For the angled impact plate, DEM accurately predicted the "effective" friction coefficient on the aluminium and sandpaper plate ($|\text{errors}| \leq 12.07$ %) when the 3-clump particles were used. Contrary to the vertical plate, the reaction forces on the angled plate were sensitive to the particle friction coefficient and the model accurately predicted both the normal and shear force components. The 5- and 10-clump particles predicted lower impact forces compared to the 3-clump particles; however, due to the increase in coordination number, the particles predicted higher "effective" friction coefficients on both surfaces. A single set of parameter values for the ball particles, $\mu_{\text{pp}} = 0.25$, $\mu_{\text{r pp}} = 0.50$, $\mu_{\text{pp}} = 0.40$ and $\mu_{\text{r pp}} = 0.125$, accurately predicted the reaction forces on the vertical and angled plates.

For the transfer hood analysis, the DEM results for the material impact position ($|\text{error}| \leq 0.29$ %), velocity profile, stream thickness ($|\text{error}| \leq 46.13$ %) and width showed good agreement with the PIV measurements. DEM accurately predicted the sudden decrease in velocity due to the discontinuity in the surface gradient of the hood and it was found that the velocity profile was mass flow independent if the trajectory stream was aligned with the hood's. The predicted material stream thickness compared very well to the measurements where a decrease in thickness was observed; however, DEM predicted that the thickness would continue to decrease while the measurements showed that the thickness increased at the hood outlet. The measurement results further showed that the material stream would reach its maximum width at and angular position of 21° – 29° while DEM predicted it to be between 20° – 25°.

The DEM results for the rock box analysis compared very well to the PIV measurements where DEM accurately predicted the material impact velocity ($|\text{error}| \leq 4.23$ %), angle ($|\text{error}| \leq 1.56$ %), slump angle ($|\text{error}| \leq 11.76$ %) and outflow velocity ($|\text{error}| \leq 7.75$ %). DEM also predicted that the slump angle and outflow velocity were mass flow-dependent while the impact velocity and angle were not, which agreed with the experimental observations. Moreover, the slump angle was very sensitive to particle friction, resulting in an increase in the angle with an increase in friction. The calibrated particle friction of 0.15, however, showed

very good agreement with the experimental results. DEM accurately predicted the material build-up height at low mass flow rates but showed less accuracy with an increase in mass flow. For 12 kg/s, the predicted height was on or just above the experimental upper bound. It was further found that the particle friction had a significant effect on the material flow out of the rock box, where the material discharged with a lower trajectory with an increase in μ_{pp}. Low particle friction values, i.e. 0.10 and 0.15, showed good agreement with the experimental results. Further, the particle damping had no significant effect on the flow. Similar results were obtained for the material profile against the back wall of the rock box, and the bed profile compared well to the experimental results. It was found that the particles could be scaled up to a factor of 1.8 and still accurately predict the material build-up height; however, based on the slump angle and outflow velocity, the maximum scaling factor was 1.6. The only flow feature which was sensitive to scaling was the slump angle. The ball particles were also simulated in the rock box, where it was found that the calibrated parameter combination (μ_{pp} = 0.25 and $\mu_{\text{r pp}}$ = 0.50) showed good agreement with the measured flow characteristics. The only flow features that were sensitive to the ball particle's sliding and rolling friction coefficients, were the slump and outflow angles, and as a result, the bed profile.

The mass flow rate with which a chute builds up and discharges was investigated, and the DEM results for the flow rates of both phases correlated very well to the experimental results ($|\text{error}| \leq 5.00$ %). However, it was found that DEM predicted the bulk density to increase significantly with an increase in the material build-up height; therefore, users should be careful in selecting the particle stiffness for this type of analyses. The particles could be scaled up by a factor of 1.6 without significantly influencing the results, and for higher scaling factors, the mass flow rate decreased for both phases ($|\text{errors}| \geq 11.27$ %). In the model, the need for the chevron pattern on the receiving belt was confirmed after repeating the simulation for a smooth belt, and the results showed that the build-up was delayed by approximately 1 s.

Based on the results presented in this study, the author would recommend to avoid simulating the particles as single spheres in a conveyor system since no accurate material flow predictions were obtained without significantly increasing the inter-particle and rolling friction. Moreover, it is extremely tedious to calibrate the rolling friction parameter in order to simulate the interlocking effect between the particles. Therefore, as a general guideline, the clumps should at least consist of three spheres. A great emphasis was also set on the DEM model's sensitivity to certain material input parameters. The results showed that the simulations were extremely sensitive to the particle-particle and particle-wall friction coefficients, and therefore, DEM modellers should be cautious when calibrating the friction coefficients. Furthermore, if a transfer chute is analysed, the DEM modeller should also be careful in the process of introducing the particles

in the system since it was found that the patterned conveyor belts could not be simulated without considering the effect by the chevron patterns. Decreasing the computation time is a very important aspect of DEM simulations where this can either be achieved by decreasing the contact stiffness or scaling the particles up. Based on these results, the DEM model was insensitive to the contact stiffness; therefore, a low contact stiffness value can be selected, and also for particle scaling factors up to 7 can accurately simulate the material trajectory from the head pulley and thereafter the impact force. However, modellers should be careful in selecting too large scaling factor for predicting the material flow through a transfer chute since the scaling factor can be dependent on the chute-to-particle size ratio

This study only focused on the modelling of cohesionless granular materials; however, many industrial processes involve the handling of materials consisting of some form of cohesion. When there is moisture present, the bulk behaviour of the material changes significantly. Therefore, a recommendation for further work would be to replicate this study, however, with cohesive materials."

13 References

Benjamin, C.W. 1999. Rapid Design Approach to the Zero-Spillage Transfer Chute, Australian Bulk Handling Review, 4(2):52-58.

Benjamin, C.W., Donecker, P., Huque, S. and Rozentals, J. 2010. The Transfer Chute Design Manual - for conveyor belt system, Conveyor Transfer Design Pty Ltd.

Catman Easy. (Version 4.1). 2018. [Computer software]. Catman Easy. HBM, Darmstadt, Germany.

C.E.M.A. 2005. Belt Conveyors for Bulk Materials, 6th Ed, Conveyor Equipment Manufacturers Association, pp. 599.

Chaves, A.P., Ferreira, F.M., De Lima, J.R., Chieregati, A.C. and Pitard, F.F. 2011. Teoria e Prática do Tratamento de Minérios – Vol 5: Manuseio de Sólidos Granulados, Editora Signus.

Coetzee, C.J. and Els, D.N.J. 2009. Calibration of Discrete Element Parameters and the Modelling of Silo Discharge and Bucket Filling, Computers and Electronics in Agriculture, 65(2):198–212, https://doi.org:10.1016/j.compag.2008.10.002.

Coetzee, C.J. 2017. Review: Calibration of the discrete element method, Powder Technology, 310:104-142, https://dx.doi.org/10.1016/j.powtec.2017.01.015.

Coetzee, C.J. 2019. Particle Upscaling: Calibration and Validation of the Discrete Element Method, Powder Technology, 344:487–503, https://doi.org/10.1016/j.powtec.2018.12.022.

Coetzee, C.J. 2020. Calibration of the discrete element method: Strategies for spherical and non-spherical particles, Powder Technology, 364:851-878, https://doi.org/10.1016/j.powtec.2020.01.076.

Cogency. [Computer software]. ASG3D Software, https://cogency.co.za.

DIN – ISO 3435, Stetigförderer. 1979. Klassifizierung und Symbolisierung von Schüttgütern, Deutsches Institut für Normung, Beuth Verlag.

Di Renzo, A. and Di Maio, F.P. 2004. Comparison of contact force models for the simulation of collisions in DEM-based granular flow codes, Chemical engineering science, 59(3):525-541, https://doi.org/10.1016/j.ces.2003.09.037.

Di Renzo, A. and Di Maio, F.P. 2005. An improved integral non-linear model for

the contact of particles in distinct element simulations, Chemical Engineering Science, 60(5):1303-1312, https://doi.org/10.1016/j.ces.2004.10.004.

Donohue, T.J., Williams, N., Reid, S.C., Chen, B. and Plinke, J. 2019. Roy Hill: A Case Study on the path to 100% Reliability, TUNRA Bulk Solids, The University of Newcastle, Callaghan, NSW, 2308, Australia.

Doroszuk, B. and Król, R. 2019. Analysis of Conveyor Belt Wear Caused By Material Acceleration In Transfer Stations, Mining Science, 26:189-201, https://doi.org/10.37190/msc192615.

Feynman, R.P., Leighton, R.B. and Sands, M. 1963. The Feynman Lectures on Physics, Volume 1. Reading, Massachusetts: Addison-Wesley.

Golka, K. 1992. Discharge Trajectories of Bulk Solids. 4th International Conference on Bulk Materials Storage, Handling and Transportation, Wollongong, NSW, Australia, 6th-8th July, pp. 497-503.

Golka, K. 1993. Prediction of the Discharge Trajectories of Bulk Materials. Bulk Solids Handling, 13(4):763-766.

González-Montellano, C., Fuentes, J.M., Ayuga-Téllez, E. and Ayuga, F. 2012. Determination of the mechanical properties of maize grains and olives required for use in DEM simulations, Journal of Food Engineering, 111(4):553–562, https://doi.org/10.1016/j.jfoodeng.2012.03.017.

Grima, A.P. 2011. Quantifying and modelling mechanisms of flow in cohesionless and cohesive granular materials. Doctor of Philosophy thesis, School of Mechanical, Materials & Mechatronic Engineering, University of Wollongong, 2011. http://ro.uow.edu.au/thesis/3425.

Grima, A.P. and Wypych, P.W. 2011. Development and validation of calibration methods for discrete element modelling, Granular Matter, 13(2):127-132. http://dx.doi.org/10.1007/s10035-010-0197-4.

Grima, A.P. and Wypych, P.W. 2010a. Discrete Element Simulation Validation: Impact Plate Transfer Station, BulkSolids Europe 2010, Wuerzburg, Germany: Vogel Business Media.

Grima, A.P. and Wypych, P.W. 2010b. Investigation into calibration of discrete element model parameters for scale-up and validation of particle–structure interactions under impact conditions, Centre for Bulk Solids and Particulate Technologies, Faculty of Engineering, University of Wollongong, North fields Avenue, Wollongong 2522, New South Wales, Australia.

Gröger, T. and Katterfeld, A. 2006. On the numerical calibration of discrete element models for the simulation of bulk solids, Computer Aided Chemical Engineering, 21:533–538, https://doi.org/10.1016/S1570-7946(06)80100-8.

Halpin, B. 1993. RG Tanna coal terminal expansion project case study- The application and benefits of controlled flow transfer chutes, Tasman Warjay Technology, Gladstone, Queensland, Australia.

Hastie, D.B. 2010. Belt conveyor transfers: Quantifying and modelling mechanisms of particle flow, Doctor of Philosophy thesis, School of Mechanical, Materials and Mechatronic Engineering, Faculty of Engineering, University of Wollongong.

Hastie, D.B. 2013. Experimental measurement of the coefficient of restitution of irregular shaped particles impacting on horizontal surfaces, Chemical Engineering Science, 101:828-836, https://doi.org/10.1016/j.ces.2013.07.010.

Ilic, D., McBride, W. and Katterfeld, A. 2007. Validation of continuum methods utilising discrete element simulations as applied to a slewing stacker transfer chute, 9th International Conference on Bulk Materials Storage, Handling and Transportation, ICBMH 2007, Newcastle, Australia.

Ilic, D. and Donohue, T.J. 2015. On the design and analysis of transfer chute systems, TUNRA Bulk Solids, University of Newcastle, Australia.

Ilic, D. 2019. Development of design criteria for reducing wear in iron ore transfer chutes, Wear, pp. 484-435, https://doi.org/10.1016/j.wear.2019.202986.

Ilic, D., Roberts, A., Wheeler, C. and Katterfeld, A. 2019. Modelling bulk solid flow interactions in transfer chutes: Shearing flow, Powder Technology, 354:30–44, https://doi.org/10.1016/j.powtec.2019.05.058.

Inventor. 2019. [Computer software]. Autodesk, San Rafael, California.

Itasca. 2019. PFC 6.0 Documentation. Itasca Consulting Group, Inc., U.S. Minneapolis.

Ji, Z., Zhang, J. and Sheng, P. 2016. An advanced 3D modeling method for concrete-like particle reinforced composites with high volume fraction of randomly distributed particles. Composites Science and Technology, 134:26-35, http://dx.doi-.org/10.1016/j.compscitech.2016.08.0090266-3538.

Kacianauskas, R. and Markauskas, D. 2011. Investigation of rice grain flow by

multi-sphere particle model with rolling resistance, Granular Matter, 13(2):143-148, http://dx.doi.org/10.1007/s10035-010-0196-5.

Korzen, Z. 1988. The Dynamics of Bulk Solids Flow on Impact Plates of Belt Conveyor Systems, Bulk Solids Handling, 8(6):689-697.

Korzen, Z. 1989. Mechanics of Belt Conveyor Discharge Process as Affected by Air Drag, Bulk Solids Handling, 9(3):289-297.

Lu, G., Third, J. and Müller, C. 2015. Discrete element models for non-spherical particle systems: from theoretical developments to applications, Chemical Engineering Science, 127:425–465, https://doi.org/10.1016/j.ces.2014.11.050.

Matlab. (Version 9.5.0.1049112). 2018. [Computer software]. MATLAB (R2018b). The Mathworks, Inc., Natick, Massachusetts.

Mascarenhas, F.P and Mesquita, A.L.A. 2013. Simulation of transfer chute operation using the discrete element method. Federal University of Para, Faculty of Mechanical Engineering, Augusto Corrêa St, Brazil.

Mousaviraad, M., Tekeste, M. and Rosentrater, K.A. 2016. Calibration and Validation of a Discrete Element Model of Corn Using Grain Flow Simulation in a Commercial Screw Grain Auger, Agricultural and Biosystems Engineering, IOWA State University.

Nakao, T. and Fityus, S. 2008. Direct Shear Testing of a Marginal Material Using a Large Shear Box, Geotechnical Testing Journal, 31(5):393-403, https://doi.org/10.1520/GTJ101237.

Olympus High Speed Video Camera rent or hire. [n.d.]. [Online]. Available at: https://www.techrentals.co.nz/product/573/olympus-i-speed3-high-speed-video-camera. [2020, 1 Feb].

Oosthuizen, F.J.J. 2018. Conveyor Impact Plates, Mechanical Project 478, Department of Mechanical and Mechatronic Engineering, Stellenbosch University.

Operations Overview | Roy Hill. 2020. [Online]. Available at: https://www.royhill.com.au/overview/pr
overview/. [2020, 20 Oct].

PFC3D. (Version 6.00.14). 2019. [Computer Software]. ITASCA Consulting Group, Inc., Minneapolis, Minnesota.

Portal, R.J.F., Dias, J.M.P. and de Sousa, L.A.G. 2010. Contact Detection Between Convex Superquadric Surfaces, IDMEC - Institute of Mechanical Engineering, In-

stituto Superior Técnico - Technical University of Lisbon.

Pust, O. 2006. PIV: Direct Cross-Correlation compared with FFT-based Cross-Correlation, Department of Fluid Mechanics, Faculty of Mechanical Engineering, University of the Federal Armed Forces Hamburg, D–22039 Hamburg, Germany.

Roberts, A.W. 2001. Chute Design Considerations for Feeding and Transfer. [Online]. Available at: http://www.saimh.co.za/beltcon/Beltcon11/Beltcon1103.html. [2019, 14 May].

Roberts, A.W. 2003. Chute Performance and Design for Rapid Flow Conditions, Centre for Bulk Solids and Particulate Technologies, The Univeristy of Newcastle, NSW., 2308, Australia

Roberts, A.W., Wiche, S.J., Ilic, D.D. and Plint, S.R. 2004. Flow Dynamics and Wear Considerations in Transfer Chute Design, ICBMH., Institution of Engineers, pp. 330-334.

Roessler, T. and Katterfeld, A. 2017. Scaling of the angle of repose test and its influence on the calibration of DEM parameters using upscaled particles, University of Magdeburg, Chair of Conveying Technology, Universitätsplatz 2, 39106 Magdeburg, Germany.

Saint-Cyr, B., Azema, E., Delenne, J.Y., Radjai, F. and Sornay, P. 2011. Effect of particle shape non-convexity on the rheology of granular media: 3D contact dynamics simulations, II Int. Conf. Part. based Methods - Fundam. Appl. pp. 1 - 8.

Scott, O.J. and Choules, P.R. 1993. The use of impact plates in conveyor transfers, Department of Mechanical Engineering, University of Newcastle, Callaghan, Australia.

Sigma 28-300mm f/3.5-6.3 DG Macro Review. [n.d.]. [Online]. Available at: https://www.imaging-resource.com/lenses/sigma/28-300mm-f3.5-6.3-dg-macro/review/. [2020, Jan 20].

Thielicke, W., and Stamhuis, E. J. 2014. PIVlab – Towards User-friendly, Affordable and Accurate Digital Particle Image Velocimetry in MATLAB, Journal of Open Research Software, 2. Ubiquity Press, Ltd. Retrieved from https://doi.org/10.5334%2Fjors.bl.

Tomasi, C. 2013. Vector Representation Of Rotations, Department of Computer Science, Duke University.

Tracker. (Version 5.1.5). 2020. [Computer software]. Tracker: Video Analysis

and Modeling Tool, https://physlets.org/tracker/.

Wang, L., Li, R., Wu, B., Wu, Z. and Ding, Z. 2018. Determination of the coefficient of rolling friction of an irregularly shaped maize particle group using physical experiment and simulations, Particuology, 38:185-195, https://doi.org/10.1016/j.partic.2017.06.003.

Wensrich, C.M. and Katterfeld, A. 2012. Rolling friction as technique for modelling particle shape in DEM, Powder Technology, 217:409-417, http://dx.doi.org/10.1016/j.powtec.2011.10.057.

Xie, L., Zhong, W., Zhang, H., Yu, A., Qian, Y. and Situ, Y. 2016. Wear process during granular flow transportation in conveyor transfer, Powder Technology, 218:65–75, https://doi.org/10.1016/j.powtec.2015.10.043.

Zhou, Z., Zou, R., Pinson, D. and Yu, A. 2013. Discrete Modelling of the Packing of Ellipsoidal Particles, AIP Conference Proceedings 1542, pp. 357-360, https://doi.org/10.1063/1.4811941.

Appendices

A Equipment Setup and Calibration For Testing

A.1 Conveyor Mass Flow Rate Calibration

The mass flow rate of conveyor 1 was measured based on when the belt was fully loaded. Four load cells (HBM HLCB1C3 550 kg) were placed underneath the frame holding up the conveyor, i.e. two at the outlet of the large hopper and two at the head pulley. The load cells were connected to a Dini Argeo DGT weight transmitter which send the measured load to the PLC for further processing. The weight transmitter was also used for the calibration and zeroing of the load cells. The calibration of the load cells were done by Massamatic (www.massamatic.com). They systematically changed the load on the belt by placing various calibrated chains along the length of the conveyor belt. The change in electrical value (mV/V) due to the added load were then entered in the weight transmitter. For a fully loaded belt, the mass flow rate $\dot{m}$ was determined using the following equation,

$$\dot{m} = \frac{m\ V_b}{L} \tag{A–44}$$

where m was the measured material mass, V_b the belt velocity and L the distance between the load cells. Equation A–44 was used in the PLC program.

The mass flow rate of the third conveyor was determined using a Dini Argeo CPWE "Enterprise" microcontroller where the calculation was similar to the calculation for the first conveyor in equation A–44. However, it did not consider the total mass on the belt but rather the mass at a section on the belt. The structure used was a belt scale weigh frame (BS143 series) which consisted of a load cell and a speed sensor. This method proved to be more accurate since the true belt speed was used rather than the set speed. The calibration of the load cell was also done by Massamatic where the same procedure was followed as described for conveyor 1. However, the calibration parameters were entered on the microcontroller. An example of the mass flow measurement for $\dot{m} = 5$ kg/s of conveyor 1 is shown in Figure 52. All the experimental tests were conducted in the steady-state region.

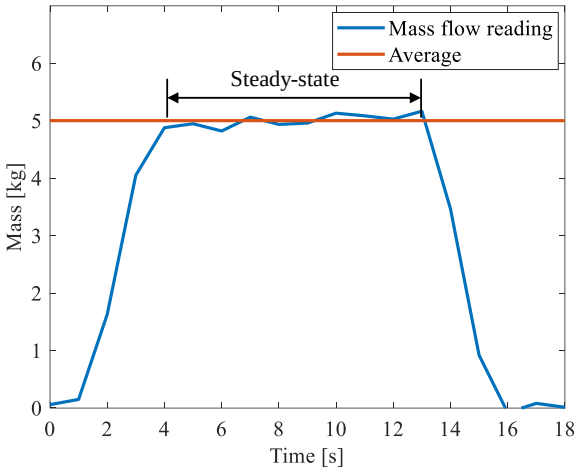

Figure 52: Mass flow rate recording of Conveyor 1.

A.2 Conveyor Belt Speed Calibration

It is essential that there is no significant difference between the conveyor's set and actual speed. The angular velocity of the three conveyor's head pulleys was measured for a range of belt speeds by using a tachometer. The results from the tachometer showed that there was a small difference between the actual and set belt speed. Calibration was therefore done by multiplying the error to the motors speed control value. This value was entered in the PLC which was used to regulate the supplied voltage to the motor, consequently controlling the rotation speed of the motor. The measurement process was repeated and the results of conveyor 1 are shown in Table 24. It is clear that conveyor 1 was successfully calibrated since there was a significantly small error between the actual and set speed.

Table 24: Conveyor 1 calibration results.

Set speed [m/s]	**Measured angular velocity [rpm]**	**Actual speed [m/s]**	**Error [%]**
5.0	286.3	4.95	-1.06
4.5	257.5	4.45	-1.13
4.0	228.0	3.94	-1.51
3.5	198.9	3.44	-1.81
3.0	173.3	2.99	-0.19
2.5	141.2	2.44	-2.41
2.0	115.6	2.00	-0.13
1.5	88.1	1.52	1.48
1.0	60.8	1.05	5.05

A.3 High-Speed Camera Setup

The cameras used for PIV were Olympus i-Speed 3. These cameras were specially designed for high-speed video analyses. The maximum resolution obtainable was 1280 × 1024 (pixels) for up to 2000 fps (frame per second) with the maximum frame rate of 150 000 fps at lower resolutions. The sensor of the camera had quite large pixels, up to 21 microns, providing good light-sensitivity with an ISO rating of 4800 for monochrome and 1600 for colour. The maximum exposure time (shutter) could be set as low as 1 μs (microsecond) for eliminating blur and ensuring detail during the motion analysis. The camera came with a trigger cable, an 8.4-inch daylight readable LCD controller/display unit (CDU), spare battery, power supply and i-Speed Suite software for the user's computer. The CDU was used to setup the camera while the trigger cable started the recording of the high-speed footage (Olympus High Speed Video Camera, [n.d.]). An additional Sigma 28 - 300 mm f/3.5-6.3 DG Macro lens was used to zoom and focus on certain areas of interest. It had a high zoom ratio, up to 10:7:1, and contained a multilayer lens coating to reduce ghost and flare, and maintain an optimum colour balance through the zoom range (Sigma 28-300mm, [n.d.]). The connection of the various components to the camera is shown in Figure 53.

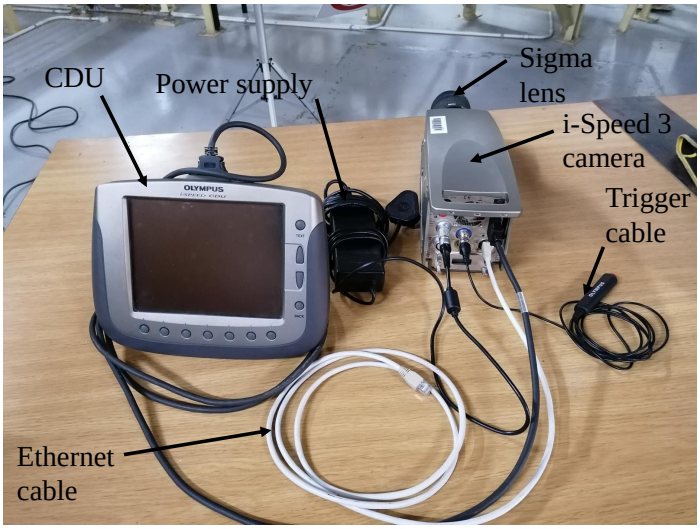

Figure 53: Olympus i-Speed 3 connection.

Two cameras were placed around the facility, with one focussing on the trajectory of the material from conveyor 1 through the transfer chute and the second camera on the material flow through the transfer chute loading onto conveyor 2, Figure 54.

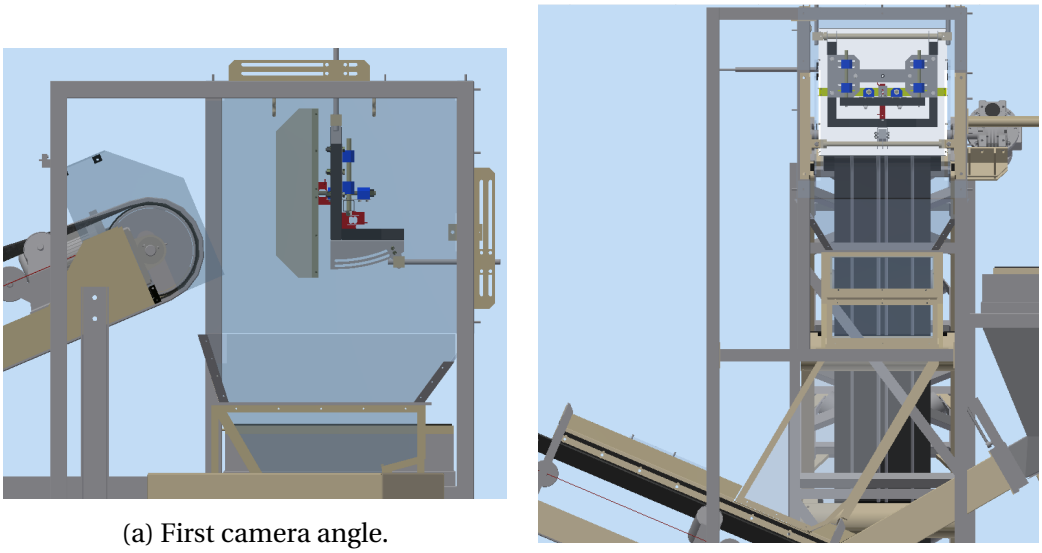

(a) First camera angle.

(b) Second camera angle.

Figure 54: Camera angles to capture the material flow through the first transfer chute (CAD model).

A problem with using the high-speed camera was the in-focus capturing of the particles when the material was being conveyed at high-speeds. The rule of thumb for choosing the right frame rate for PIV is that the particle which is being tracked should overlap himself with a third of his length in the next frame. This was obtained at 500 fps. Although the frame rate was perfect, the corn particles tend to be out of focus and was a bit stretched in every frame. This was due to the shutter (exposure time) being too large. The shutter time was therefore decreased to 20 μs, but the problem with this was that the time in which the lens opens and closes was less, causing less light to enter the camera lens. As a result, the video displayed too dark for this shutter time, barely seeing anything besides pitch black. The only solution was to focus more light on the area of interest, effectively allowing more light to reflect into the camera lens. During the recording of slow-motion videos, ordinary lightbulbs tend to flicker caused by Eskom's generators which are synchronised at 50 Hz. Therefore, three Osram halogen 1000 W 230-240 V G9.5 (27 500 lm) lightbulbs were used due to its high heat dissipation causing the lightbulbs to never turn off.

A.4 Impact Plate Calibration

The calibration setup of the normal (S2M 500 N HBM) and shear (S2M 200 N HBM) load cell is shown in Figures 55a and 55b, respectively. The calibration was done by systematically varying the load on the surface of the impact plate while measuring the electrical value (mV/V) from the data acquisition system. A good approximation for the calibration range was between the estimated measuring loads. According to the impact plate analytical model using the model parame-

ters in Table 5, the maximum force to be expected was 50 N. Therefore, the load cells were calibrated between no-load and 5 kg. The results were tabulated and plotted for both load cells, denoted in Figures 55c and 55d. To verify the accuracy of the load cells, two 2 kg (39.24 N) dead weights were placed on the impact plate at various locations while recording the load. The results in Figure 56 shows that the load cells were successfully calibrated.

(a) Normal load cell setup.

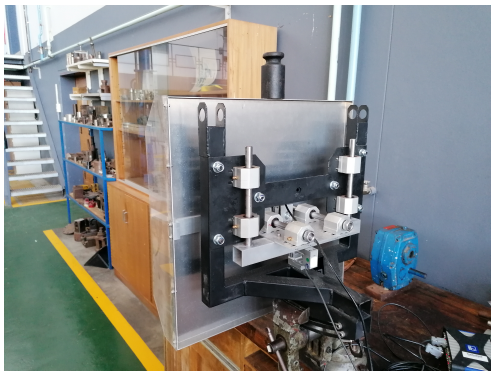

(b) Shear load cell setup.

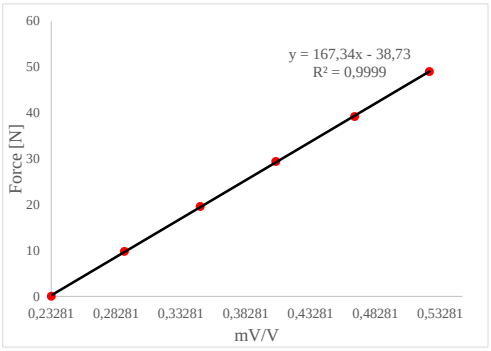

(c) Normal load cell calibration results.

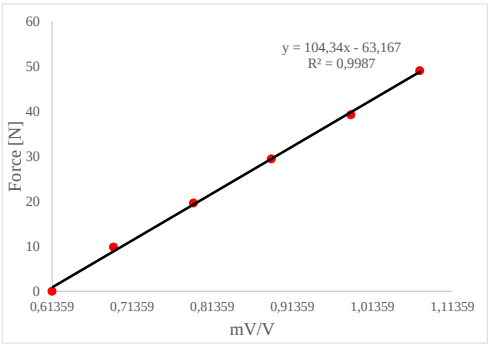

(d) Shear load cell calibration results.

Figure 55: Load cell calibration (a,b) setup and (c,d) results.

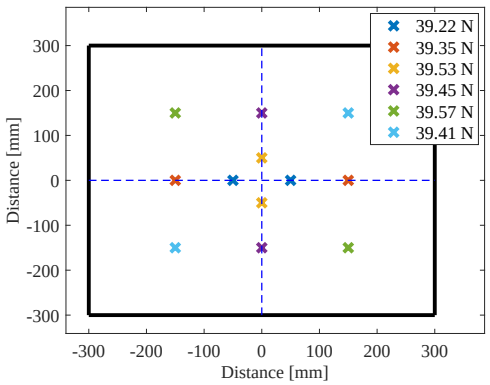

(a) Normal load cell.

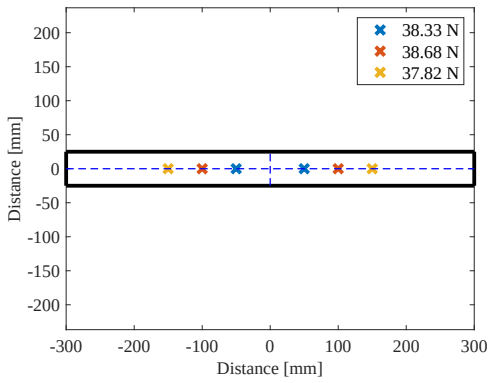

(b) Shear load cell.

Figure 56: (a) Normal and (b) shear load cell validation.

A.5 Rotating Surface Test Calibration

The load cell (S2M 50 N HBM) for the rotating surface tests was calibrated using the same experimental setup as shown in Figure 11b; however, it was vertically aligned. The calibration was implemented by hanging calibration weights at the end of the shaft with the hook. The calibration load was systematically varied between no-load, 0.2 kg, 0.5 kg, 1 kg and 2 kg while the electrical value (mV/V) were measured and tabulated. The calibration results are shown in Figure 57 which indicate that the load cell was successfully calibrated.

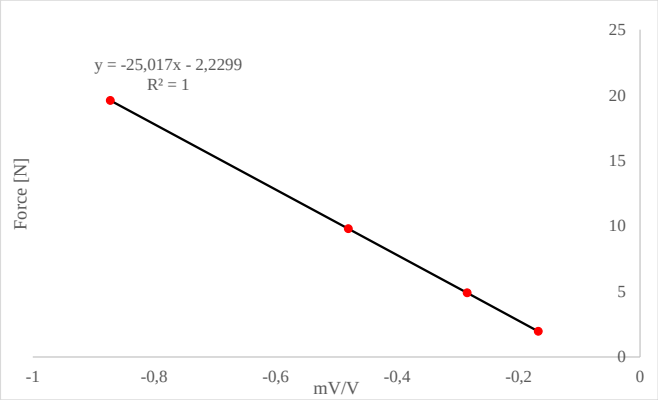

Figure 57: Load cell calibration results for rotating surface test.

B Particle Generation

To generate a specified mass flow rate, the particles were randomly generated and packed in a rectangular box above the conveyor belt, Figure 58. The number of particles generated depended on the equivalent volume diameter D_{ev}, particle scale, particle density ρ_{p} and specified mass flow rate $\dot{m}$. Using the equivalent volume diameter and the particle scale, the average particle radius r_{avg} was determined as,

$$r_{\mathrm{avg}} = \text{Particle scale} \times \frac{D_{ev}}{2} \tag{B–45}$$

Since the equivalent volume diameter was determined by assuming the particles were spherical, the volume of the particles, $\mathrm{V}_{\mathrm{particle}}$, was equal to the volume of a sphere with the radius being the average particle radius determined in equation B–45,

$$\mathrm{V}_{\mathrm{particle}} = \frac{4}{3}\,\pi\, r_{\mathrm{avg}}^3 \tag{B–46}$$

The mass per particle was then determined by,

$$m_{\mathrm{particle}} = \rho_{\mathrm{p}}\, \mathrm{V}_{\mathrm{particle}} \tag{B–47}$$

where the particle density ρ_{p} was the calibrated particle density in Section 6.2.2. The number of particles to generate per second was then determined by dividing the particle mass with the mass flow rate,

$$\text{Total clumps (per second)} = \frac{\dot{m}}{m_{\mathrm{particle}}} \tag{B–48}$$

The particle scale can now be varied in the simulations, generating larger particles with a larger mass per particle; hence, the desired mass flow rate stayed the same since only the total clumps changed. It was verified in Section 6.2.2, that the particle scale did not affect the particle density ρ_{p} since there was no overlapping between the particles.

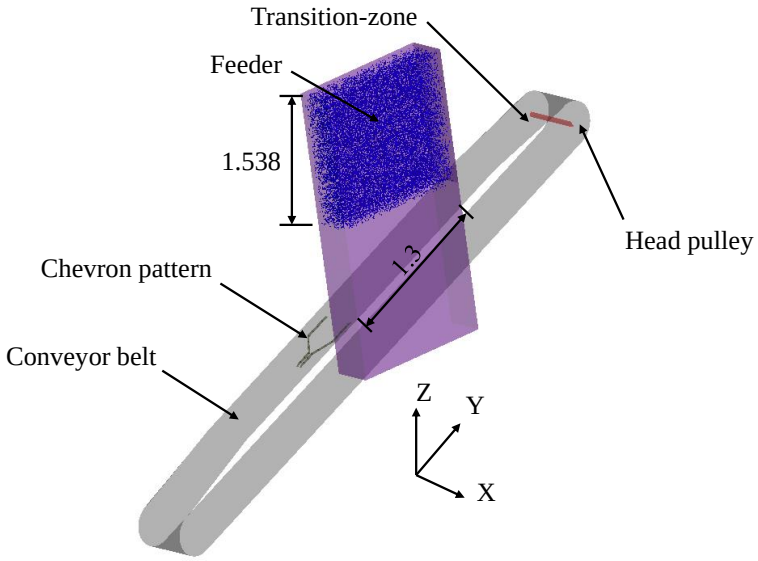

Figure 58: Generated particles in a box.

Considering the right amount of particles were generated to obtain a specified mass flow rate, the period for the release of the particles from the feeder should also be accurately determined. Using the measurements for the particles drop height and the length of the particles on the belt in the box, Figure 58, and assuming a safety factor of 0.8 to ensure that there were no gaps between successive generated boxes of particles, the timestep for the release of the particles was derived (equation B–49). The second term, $\sqrt{\frac{1.538}{0.5\times 9.81}}$, of equation B–49 was derived using the linear equations of motion.

$$T_{\text{p, gen}} = 0.8\left(\frac{1.3}{V_b} + \sqrt{\frac{1.538}{0.5 \times 9.81}}\right) \tag{B–49}$$

C Discharged Mass Flow Rate

The mass flow rate was the most important parameter to be accurately modelled; otherwise, useful comparisons could not be made between the DEM and experimental results. A common mistake which DEM users make, is to specify the rate at which particles are introduced into the system (a particle factory at a certain location along the feeding belt), and not checking if the mass flow at the head pulley discharge is the same as the specified flow rate. DEM input parameters such as particle shape and size, particle sliding and rolling friction, and particle and particle-wall damping, affect the bulk behaviour of the particles on a moving conveyor belt, and especially for high inclined belts, the material can roll back, resulting in a lower rate of discharge at the head pulley. Furthermore, if the simulation is run for only a number of seconds or even minutes, the build-up on the conveyor might not be visible.

The total number of particles discharged from the head pulley, for the various particle shapes, are shown in Figures 59a and 59b for the pattern and clump acceleration model, respectively. The results showed that the number of particles discharged oscillated over time, and consequently so did the mass flow rate. Larger oscillations were observed for the pattern model. This was, however, expected since the chevron pattern caused larger piles of material between successive pattern sets. Nevertheless, the average mass flow rate was of importance, Table 25. The results show that both models were very accurate in achieving the specified mass flow rate (|error| $\leq$ 3.75 %).

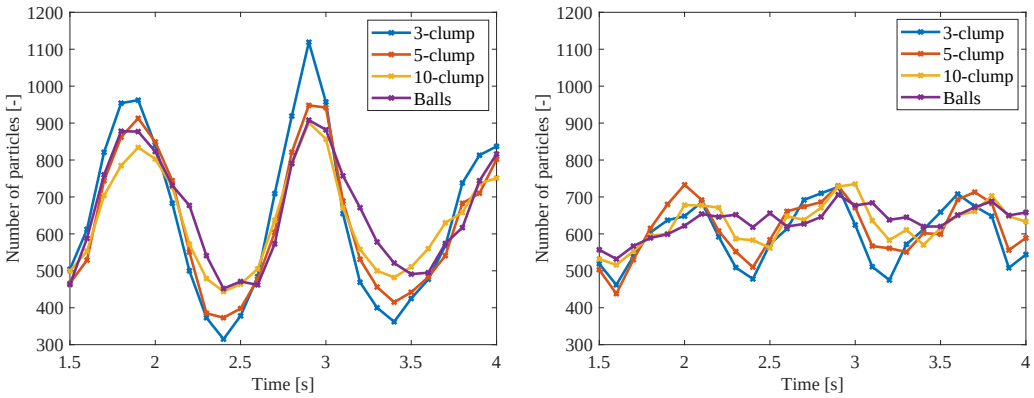

(a) Pattern simulation model. (b) Clump acceleration simulation model.

Figure 59: Total particles discharged for the various investigated particle shapes using the (a) pattern and (b) clump acceleration model (V_b = 3 m/s and $\dot{m}$ = 8 kg/s).

Table 25: Average mass flow rate $\dot{m}$ and discharge velocity V_d by the pattern and clump acceleration models ($V_b = 3$ m/s and $\dot{m} = 8$ kg/s).

Particle shape	**Pattern model**			**Clump acceleration model**		
	V_d [m/s]	**$\dot{m}$ [kg/s]***		**V_d [m/s]**	**$\dot{m}$ [kg/s]***	
3-clump	2.83	8.03	0.38 %	2.89	7.77	-2.88 %
5-clump	2.85	7.85	-1.88 %	2.87	7.78	-2.75 %
10-clump	2.82	7.91	-1.13 %	2.79	7.73	-3.38 %
Balls	2.74	7.88	-1.50 %	2.75	7.70	-3.75 %

*The percentage error of the mass flow rates was calculated by comparing it to the specified mass flow rate.

D Computation Time

In PFC3D (2019), the critical timestep was automatically calculated and updated using equation 6–41. The user has the ability to specify a safety factor, however, the default value of 0.8 was used throughout. From Figure 60a for the normalised simulation time of the simulated particle shapes, it is clear that the number of spheres which the particles contain had a significant effect on the computation time and increases exponentially. The results shows that the ball particles simulated approximately 14 times faster than the 10-clump particles.

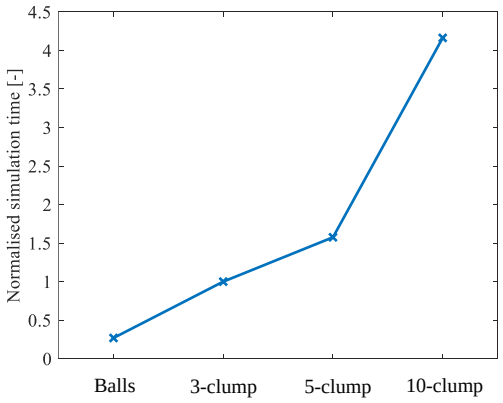

(a) Effect of the particle shapes.

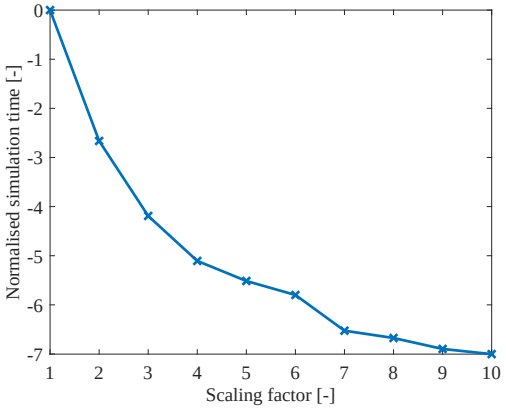

(b) Effect of particle scaling (Semi-log).

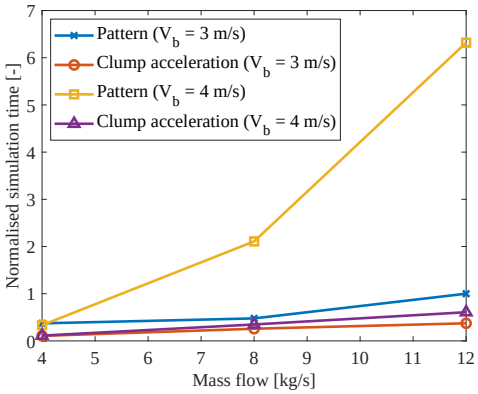

(c) Effect of the pattern and clump acceleration models.

Figure 60: Effect of the (a) particle shapes, (b) scaling factors and (c) simulation methods on the simulation time.

Figure 60b shows the normalised simulation time for scale factors up to 10 on a logarithmic scale for the y-axis. The results shows a significant decrease in the computation time from a scale factor of 1 to 3. Thereafter, the scale factor had no significant effect on the computation time.

The normalised simulation time of the pattern and clump acceleration models for belt speeds of 3 m/s and 4 m/s, and mass flow rates of 4 kg/s to 12 kg/s is

shown in Figure 60c. It is clear that the belt speed and mass flow rate had a significant effect on the computation time. The results also showed that by including the chevron patterns, increased the computation time significantly, especially for $V_b = 4$ m/s with $\dot{m} = 12$ kg/s.

E Simulation Time

The impact plate analysis was used to determine the required time until steady-state was reached and the minimum duration of the simulations. It is clear from the predicted normal force measurement, Figure 22b,that the force reached its steady-state at approximately 0.5 s and oscillated thereafter. It also took approximately 1 s for the particles to reach the impact plate. Therefore, the simulations were investigated at simulation times larger than 1.5 s. To obtain a required simulation time, three simulations were completed for 20 s while the normal force was measured. An average was determined between the time-intervals of 1.5 s to 4 s and 1.5 s to 20 s. The results in Table 26 shows that the maximum error obtained was 2.02 %; therefore, it was assumed that a simulation time of 4 s was sufficient to model the impact plate. However, for the transfer hood and rock box analyses (Sections 9 and 10, respectively), the simulation time was increased to 5 s since the impact location was further from the head pulley.

Table 26: Simulation time validation results.

Simulations	**Normal force at time-intervals [N]**		**Error**
	1.5 s to 4 s	**1.5 s to 20 s**	
1	25.25	24.75	2.02 %
2	7.48	7.40	1.08 %
3	5.00	5.08	-1.57 %

F Korzen Analytical Model Correction

According to Figure 2, using the given coordinate system, the material impact angle α_p should be positive measured relative to the positive X-axis. This was not evident when equation 4–1 was used since the division of cosine raised to the power of 2 was larger than tan of the angle. In the case when the impact plate was vertical ($\beta = 0°$), a negative α_p had no influence on the value of the outflow velocity V_a in equation 4–7. As a result, the right reaction forces were still obtained since the cosine and sine of the impact angle were raised to the power of 2 (see equations 4–12 and 4–13), consequently providing a positive value. The problem came when the impact plate was tilted ($\beta \neq 0°$). For a positive and negative tilted plate, the angle between V_p and normal to the plate should be $(\alpha_p + \beta)$ and $(\alpha_p - \beta)$, respectively. If the determined impact angle was negative, these angles would not hold and consequently be larger or smaller than it should be in the calculations. At certain angles and discharge velocities, the Korzen model diverged for the iterative process of determining V_a and was therefore incapable of determining the reaction forces.

A similar approach to Korzen (1988, 1989) was used to rectify the mistake. The new coordinate system is shown in Figure 61 where Y is positive from top to bottom and X from right to left. From the linear equations of motion with an initial velocity $\overrightarrow{V_d}$ two equations were derived to determine the impact velocity in the Y-direction, V_{py},

$$+\downarrow: \quad V_{py} = -|\overrightarrow{V_d}| \sin\alpha_d + g\ t \tag{F–50}$$

$$\overset{+}{\leftarrow}: \quad S \pm S_0 = |\overrightarrow{V_d}| \cos\alpha_d\ t \tag{F–51}$$

After substituting equation F–51 into F–50 and eliminating t, the Y-component of the impact velocity was obtained as,

$$+\downarrow: \quad V_{py} = -|\overrightarrow{V_d}| \sin\alpha_d + \frac{g\ (S \pm S_0)}{|\overrightarrow{V_d}| \cos\alpha_d} \tag{F–52}$$

The X-component for the impact velocity, V_{px}, was also derived by using the linear equations of motion,

$$\overset{+}{\leftarrow}: \quad V_{px} = |\overrightarrow{V_d}| \cos\alpha_d \tag{F–53}$$

The resultant vector between $\overrightarrow{V_{px}}$ and $\overrightarrow{V_{py}}$ yields the magnitude of the impact velocity $\overrightarrow{V_p}$, and the angle between $\overrightarrow{V_p}$ and the X-axis was the impact angle α_p (see Figure 61).

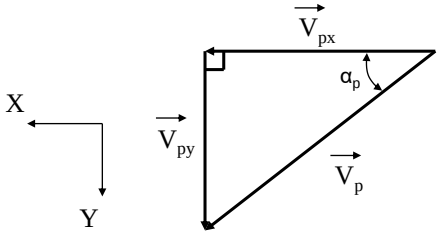

Figure 61: Impact plate velocity triangle.

Using Pythagoras' theorem, $|\overrightarrow{V_p}|$ was determined by,

$$\begin{aligned} |\overrightarrow{V_p}| &= \sqrt{|\overrightarrow{V_{px}}|^2 + |\overrightarrow{V_{py}}|^2} \\ &= \sqrt{|\overrightarrow{V_d}|^2 - 2\,\tan\alpha_d\; g\;(S \pm S_0) + \frac{g^2\;(S \pm S_0)^2}{|\overrightarrow{V_d}|^2\;\cos^2\alpha_d}} \end{aligned} \tag{F–54}$$

with the impact angle α_p,

$$\begin{aligned} \alpha_p &= \arctan\;\frac{V_{py}}{V_{px}} \\ &= \arctan\left(\frac{g\;(S \pm S_0)}{|\overrightarrow{V_d}|^2\;\cos^2\alpha_d} - \tan\alpha_d\right) \end{aligned} \tag{F–55}$$

It was found that only the equation to determine the impact angle was incorrect from Korzen's (1988, 1989) method, but this was due to the mistaken orientation of the coordinate system.

G PIV Analysis Procedure

The software used for particle image velocimetry was PIVLab (Thielicke and Stamhuis, 2014). Two cross-correlation algorithms were considered, namely Fast-Fourier-Transform (FFT) and direct cross-correlation (DCC). The advantage of using the FFT was the fast computing time where the drawbacks were the concern of the flexibility and accuracy of the velocity vectors. The DDC algorithm is well defined for finite regions and would therefore have no issues regarding the interrogation of finite sub-samples for successive frames, whereas the FFT algorithm is well defined for infinite regions. Hence, the finite region should be translated to an infinite domain (Pust, 2016). According to Pust, if the accuracy is of importance, exceeding computational time, the DDC algorithm should be considered. But if the particle image interrogation method for the FFT algorithm provides sufficient quality, the use of the FFT is also acceptable.

The two cross-correlation algorithms were investigated by using the material outflow velocity from the impact plate as the comparable measure. The tracking of the pixels for the FFT algorithm underwent four interrogation area (px) passes which systematically decreased from 64×64 in the first step, then 32×32, 16×16 and lastly 8×8. While the DCC algorithm only had one 8×8 interrogation pass. The outflow velocity was obtained by implementing a time-averaging approach where the velocity magnitude was determined over 1000 frames which is equivalent to 2 s. The velocity magnitude was measured using PIVLab's *poly-line* measuring tool where the velocity was extracted by drawing a horizontal line through the material stream. The results showed that the DDC algorithm displayed a more uniform distribution of the data around the average velocity (Figure 62), although there was no significant difference found between the average velocity obtained by the two methods, i.e. 1.98 m/s from the FFT algorithm and 2.00 m/s from the DDC algorithm. It was decided that anyone of the two cross-correlation algorithms was acceptable since there were a lot of external factors that also played a part in the accuracy of the velocity vectors. The external factors only influenced the software's ability to track the exact centre-to-centre distance the corn grains travelled for successive frames since the timestep stayed constant. External factors included: (1) camera perspective, (2) shadows on the corn grains, (3) corn grains moving towards or away from the camera, (4) rotation of the corn grains, (5) corn grains passing each other and (6) corn grains further away from the calibrated structure caused a smaller velocity vector.

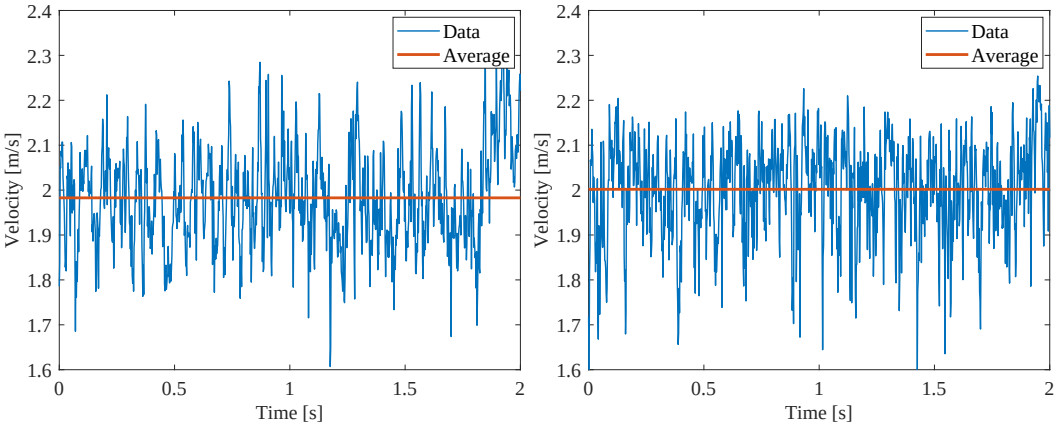

(a) FFT algorithm.

(b) DCC algorithm.

Figure 62: Material outflow velocity comparison between the (a) FFT and (b) DCC cross-correlation algorithms.

H Vertical Impact Plate: Particle Shape

H.1 Clumps

The results in Table 27 showed that the 5- and 10-clump particles accurately predicted the total force R (|error| ≤ 9.89 %) and impact velocity V_p (|error| ≤ 5.31 %) for both belt speeds and simulation models. The 5-clump particles also accurately predicted the impact angle α_p using both models (|error| ≤ 5.34 %); however, the 10-clump particles only failed to accurately predict the angle with the clump acceleration model (error = 14.87 %). For V_b = 4 m/s, the 5- and 10 clump particles overestimated the angle with 5.03° and 5.43°, respectively. Furthermore, the more accurate particles had no significant effect on the outflow velocity V_a compared to the 3-clump particles and as a result, overestimated the velocity for a belt speed of 3 m/s (11.65 % ≤ error ≤ 14.08 %) and accurately predicted it for a belt speed of 4 m/s (|error| ≤ 0.90 %).

Table 27: Predicted impact force R, velocity V_p, angle α_p and outflow velocity V_a on a vertical plate using the 5- and 10-clump particles (V_b = 3 m/s and $\dot{m}$ = 8 kg/s).

Clump model	Simulation method	Belt speed [m/s]	Reaction force and material flow characterictics					
			R [N]	Compared to* 3-clump model	Compared to** measurements	V_p [m/s]	Compared to* 3-clump model	Compared to** measurements
5	Pattern	3	22.48	-2.01 %	-5.03 %	2.74	0.74 %	-1.08 %
		4	27.80	0 %	-1.24 %	3.41	0.59 %	-4.75 %
	Clump acc.	3	21.98	-4.18 %	-7.14 %	2.70	-0.74 %	-2.53 %
10	Pattern	3	22.20	-3.23 %	-6.21 %	2.71	-0.37 %	-2.17 %
		4	27.67	-0.47 %	-1.71 %	3.39	0 %	-5.31 %
	Clump acc.	3	21.33	-7.02 %	-9.89 %	2.64	-2.94 %	-4.69 %
			α_p [°]	Compared to* 3-clump model	Compared to** measurements	V_a [m/s]	Compared to* 3-clump model	Compared to** measurements
5	Pattern	3	16.32	-3.09 %	5.09 %	2.35	1.73 %	14.08 %
		4	1.33	-15.29 %	135.95 %	2.20	4.76 %	-0.90 %
	Clump acc.	3	16.36	2.25 %	5.34 %	2.34	1.30 %	13.59 %
10	Pattern	3	16.85	0.06 %	8.50 %	2.34	1.30 %	13.59 %
		4	1.73	10.19 %	146.76 %	2.21	5.24 %	-0.45 %
	Clump acc.	3	17.84	11.50 %	14.87 %	2.30	-0.43 %	11.65 %

The percentage error was calculated by comparing the results of the 5- and 10-clump particles to the results of the *3-clump particles and **experimental tests.

The average peak force from the normal force measurement for the 3-, 5- and 10-clump particles was 69.90 N, 55.57 N and 46.85 N, respectively (Figure 63). It is clear that the magnitude of the peaks decreased with an increase in the accuracy of the particle. From the experimental force measurement (Figure 22a in Section 8.2.1), the average peak force was recorded as 51.48 N; hence, the 5- or 10-clump particles would be sufficient to accurately predict the peak forces since the relative error was 7.94 % and -8.99 %, respectively.

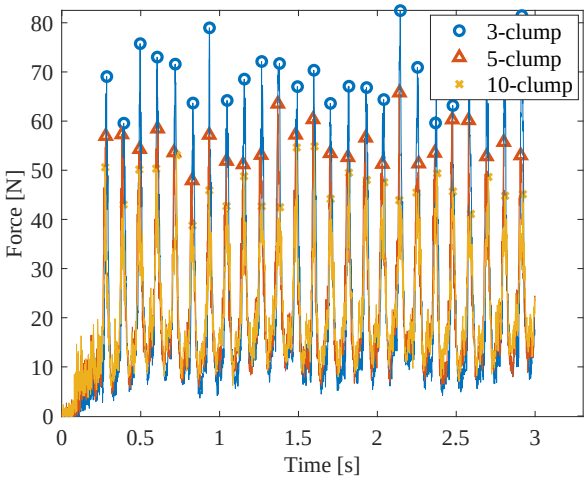

Figure 63: Peak forces of the normal force measurement for the 3-, 5- and 10-clump particles on a vertical plate ($V_b = 3$ m/s and $\dot{m} = 8$ kg/s).

H.2 Balls

Due to the ball particle's spherical shape, a particle-wall rolling friction coefficient $\mu_{\text{r pw}}$ was included and calibrated, Figure 64. From the results, it is clear that there was an increase in the average normal force with an increase in $\mu_{\text{r pw}}$; however, for $\mu_{\text{r pw}}$ values larger than 0.10, the effect of the parameter was negligible. As a result, it is concluded that the reaction force depends solely on the inter-particle friction, and the $\mu_{\text{r pw}}$ parameter was selected as 0.10 for the conveying of corn grains simulated as ball particles.

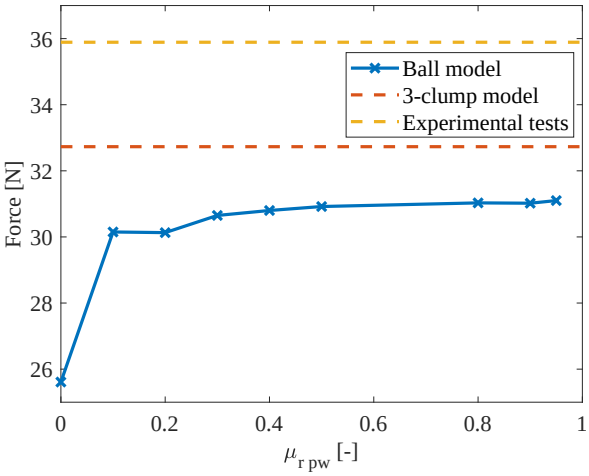

Figure 64: Predicted average normal force on a vertical impact plate for a variation in $\mu_{\text{r pw}}$ with $\mu_{\text{pp}} = 0.20$ and $\mu_{\text{r pp}} = 0.125$ ($V_b = 3$ m/s and $\dot{m} = 12$ kg/s).

Further investigation was attempted by using various combinations of μ_{pp} and $\mu_{\text{r pp}}$ to obtain a combination set that would accurately predict the reaction force

and material flow characteristics on a vertical plate. The results presented in Table 28 for a belt speed of 3 m/s and mass flow rate of 12 kg/s showed that no combination in the feasible region obtained by Coetzee (2020) (Figure 14a in Section 6.2.3) could accurately predict all four measures. From the results for combinations, $\mu_{pp} = 0.20$ and $\mu_{r\,pp} = 0.125$, and $\mu_{pp} = 0.20$ and $\mu_{r\,pp} = 0.80$, it is clear that the particle rolling friction $\mu_{r\,pp}$ had an effect on the simulation results. As a result, the $\mu_{r\,pp}$ value was increased to 0.50 for the calibrated particle friction μ_{pp} of 0.25. It was found that this combination accurately predicted the impact force (-7.77 % error), velocity (-0.72 % error) and angle (-0.66 % error). Larger particle friction values (μ_{pp} of 0.40 and 0.70) were also investigated while the particle rolling friction was set to 0.125. Similar results were obtained by the higher μ_{pp} values, where only the impact force, velocity and angle were accurately predicted. The ball particles overestimated the after-impact velocity V_a with errors larger than 20.41 %. As a result, no value of μ_{pp} or $\mu_{r\,pp}$ could accurately predict the measured velocity. This was due to the ball particles having only a single contact with the impact plate during the collision, hence, friction had a negligible effect.

Table 28: Predicted impact force R, velocity V_p, angle α_p and outflow velocity V_a on a vertical plate for various combinations of μ_{pp} and $\mu_{r\,pp}$ with $\mu_{r\,pw} = 0.10$ ($V_b = 3$ m/s and $\dot{m} = 12$ kg/s).

μ_{pp}	$\mu_{r\,pp}$	Reaction force and material flow characteristics					
		R [N]	**Compared to* 3-clump model**	**Compared to** measurements**	**V_p [m/s]**	**Compared to* 3-clump model**	**Compared to** measurements**
0.15	0.18	29.72	-10.10 %	-17.81 %	2.60	-3.70 %	-6.37 %
0.20	0.125	30.42	-7.99 %	-15.87 %	2.64	-2.22 %	-4.93 %
0.20	0.80	32.11	-2.87 %	-11.20 %	2.71	0.37 %	-2.41 %
0.25	0.125	31.71	-4.08 %	-12.31 %	2.66	-1.48 %	-4.32 %
0.25	0.50	33.35	0.88 %	-7.77 %	2.76	2.22 %	-0.72 %
0.40	0.125	32.85	-0.64 %	-9.15 %	2.73	1.11 %	-1.69 %
0.70	0.125	33.67	1.85 %	-6.89 %	2.76	2.22 %	-0.61 %
		α_p [°]	**Compared to* 3-clump model**	**Compared to** measurements**	**V_a [m/s]**	**Compared to* 3-clump model**	**Compared to** measurements**
0.15	0.18	18.62	6.83 %	22.66 %	2.36	0.43 %	20.41 %
0.20	0.125	17.90	2.70 %	17.92 %	2.38	1.28 %	21.43 %
0.20	0.80	16.16	-7.29 %	6.46 %	2.41	2.55 %	22.96 %
0.25	0.125	16.88	-3.16 %	11.20 %	2.39	1.70 %	21.94 %
0.25	0.50	15.08	-13.48 %	-0.66 %	2.43	3.40 %	23.98 %
0.40	0.125	15.98	-8.32 %	5.27 %	2.43	3.40 %	23.98 %
0.70	0.125	15.40	-11.65 %	1.45 %	2.42	2.98 %	23.47 %

The percentage error was calculated by comparing the ball particle results to the results of the *3-clump particles and **experimental tests.

Figure 65 shows the average material profile of the ball and 3-clump particles at discharge (head pulley). It is clear from the results for the ball particles that the material profile was insensitive to the inter-particle friction and the material height was approximately 5 mm higher compared to the 3-clump particles. This was due to the larger porosity between the ball particles. This effect with the less interlocking between the particles are clear in the trajectory plot, Figure 66, where there were large deviations from the mainstream.

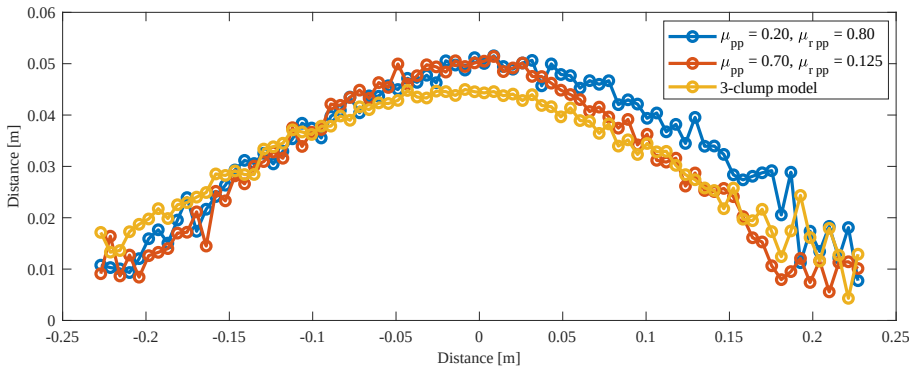

Figure 65: Average material profile at the head pulley using the ball and 3-clump particles ($V_b = 3$ m/s and $\dot{m} = 12$ kg/s).

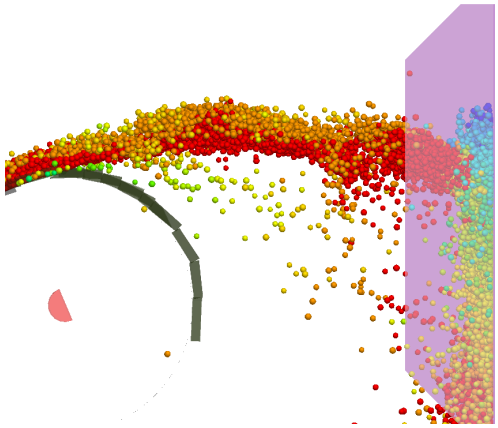

Figure 66: Material trajectory of the ball particles impacting an impact plate with $\mu_{\text{pp}} = 0.25$ and $\mu_{\text{r pp}} = 0.50$ ($V_b = 3$ m/s and $\dot{m} = 12$ kg/s).

I Material Flow onto an Angled Impact Plate

The recorded and predicted material flow hitting an aluminium and P40 sandpaper plate are presented in Figures 32 and 67, respectively. There was a significant difference for the material flow on the two surfaces, where the material stayed longer in contact with the aluminium plate compared to the sandpaper surface. This was due to higher friction coefficient, causing a significant decrease in velocity. Furthermore, the predicted material flow compared very well to the recorded flow, predicting the longer contact time on the aluminium plate and the significant decrease in velocity on the sandpaper surface, indicated by the colour change for the velocity of the particles.

Figure 68 shows the measured and predicted after-impact velocity V_a. The DEM results showed a decrease in velocity with an increase in particle-wall friction μ_{pw}. It was found that DEM accurately predicted the outflow velocity, slightly underestimating the velocity with 1.44 % and 8.33 % on the aluminium and sandpaper surface, respectively.

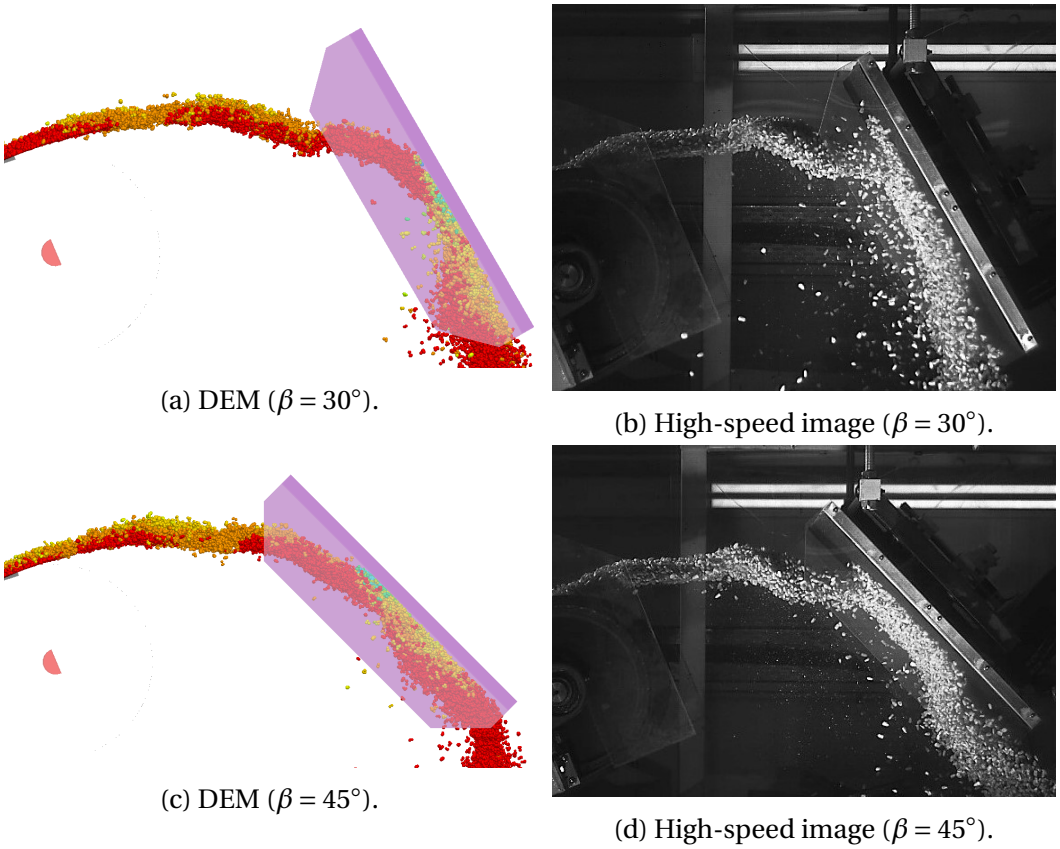

(a) DEM ($\beta = 30°$).

(b) High-speed image ($\beta = 30°$).

(c) DEM ($\beta = 45°$).

(d) High-speed image ($\beta = 45°$).

Figure 67: Material flow onto an angled impact plate with a sandpaper surface from (a,c) DEM and (b,d) high-speed footage for $\beta = 30°$ and $\beta = 45°$ ($V_b = 3$ m/s and $\dot{m} = 12$ kg/s).

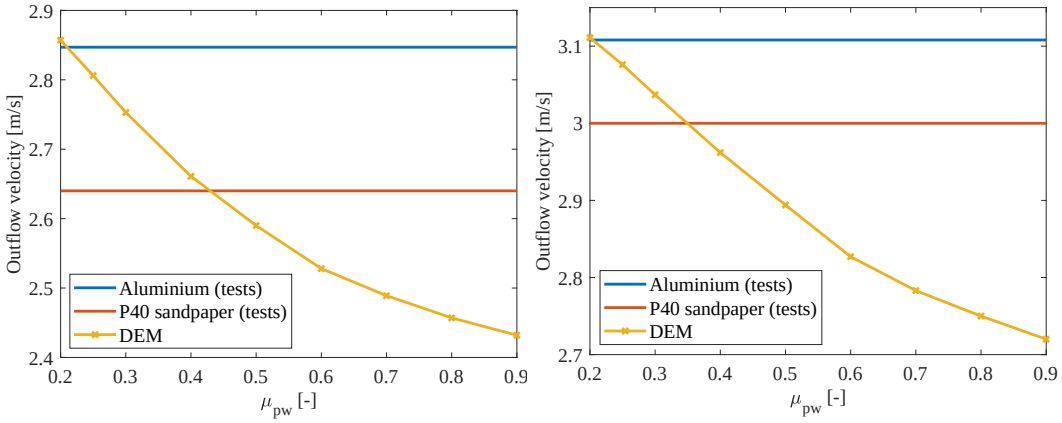

(a) 30°. (b) 45°.

Figure 68: After-impact velocity V_a from PIV and DEM for a variation in μ_{pw} (V_b = 3 m/s and $\dot{m}$ = 8 kg/s).

J Angled Impact Plate: Particle Shape

J.1 Clumps

The results for the 5- and 10-clump particles showed a significant decrease in the impact forces with an increase in the accuracy of the particle shape, Table 29 and as a result, the 5- and 10-clump particles failed to accurately predict the measured R_n and R_s forces. An increase in "effective" friction on the plate was observed using the 5- and 10-clump particles, where the friction with the 5-clump particles was accurately predicted on the 45° impact plate for both surface materials; however, for $\beta = 30°$, only the friction on the aluminium surface was accurately predicted. The 10-clump particles were only accurate in predicting the friction on the aluminium plate for $\beta = 45°$. These results showed that the "effective" friction was very sensitive to the coordination number and the tilt angle. Interestingly, the 5- and 10-clump particles accurately predicted the measured after-impact velocity V_a (0.64 % ≤ |error| ≤ 9.47 %) and showed no significant difference to the results by the 3-clump particles (0.32 % ≤ |error| ≤ 1.22 %). It was, however, found in Section 8.2.5.1 that the more accurate particles failed to predict the after-impact velocity on a vertical impact plate for $V_b = 3$ m/s.

Table 29: Predicted reaction forces and after-impact velocity on an angled impact plate using the 5- and 10-clump particles ($V_b = 3$ m/s and $\dot{m} = 8$ kg/s).

Clump model	Tilt angle, β [°]	μ_{pw} [-]	Reaction forces and after-impact velocity					
			R_n [N]	Compared to* 3-clump model	Compared to** measurements	R_s [N]	Compared to* 3-clump model	Compared to** measurements
5	30	0.25	12.31	-4.87 %	-20.79 %	2.90	-3.65 %	-17.14 %
		0.80	13.21	-5.71 %	-16.92 %	6.81	0.29 %	48.04 %
	45	0.25	6.61	-8.58 %	-20.93 %	1.62	-7.95 %	-23.58 %
		0.80	7.94	-6.48 %	-14.72 %	4.83	-3.59 %	-9.89 %
10	30	0.25	11.03	-14.76 %	-29.02 %	2.64	-12.29 %	-24.57 %
		0.80	11.91	-14.99 %	-25.09 %	6.68	-1.62 %	45.22 %
	45	0.25	4.58	-36.65 %	-45.22 %	1.13	-35.80 %	-46.70 %
		0.80	5.81	-31.57 %	-37.59 %	3.86	-22.95 %	-27.99 %
			R_s/R_n [-]	Compared to* 3-clump model	Compared to** measurements	V_a [m/s]	Compared to* 3-clump model	Compared to** measurements
5	30	0.25	0.24	4.35 %	4.35 %	2.82	0.36 %	-1.05 %
		0.80	0.52	8.33 %	79.31 %	2.43	-1.22 %	-7.95 %
	45	0.25	0.25	4.17 %	0 %	3.09	0.32 %	-0.64 %
		0.80	0.61	3.39 %	5.17 %	2.76	0.36 %	-8.00 %
10	30	0.25	0.26	13.04 %	13.04 %	2.81	0.36 %	-1.40 %
		0.80	0.56	16.67 %	93.10 %	2.39	-1.22 %	-9.47 %
	45	0.25	0.25	4.17 %	0 %	3.13	0.32 %	0.64 %
		0.80	0.67	13.56 %	15.52 %	2.81	0.36 %	-6.33 %

The percentage error was calculated by comparing the results of the 5- and 10-clump particles to the results of the *3-clump particles and **experimental tests.

J.2 Balls

The simulation results showed that the reaction forces increased with an increase in μ_{pp} and $\mu_{r\,pp}$, Table 30. The calibrated combination by Coetzee (2020), $\mu_{pp} = 0.20$ and $\mu_{r\,pp} = 0.125$, showed inaccuracies where only the "effective" friction on the aluminium surface and the after-impact velocity were accurately predicted.

The combinations for $\mu_{pp} = 0.25$ and $\mu_{r\,pp} = 0.50$, and $\mu_{pp} = 0.40$ and $\mu_{r\,pp} = 0.125$ were the only combinations which accurately predicted the normal and shear forces (|error| ≤ 7.55 %); however, only the shear component on the sandpaper surface was completely underestimated. As a result, the "effective" friction was also underestimated with -20.69 % for $\mu_{pp} = 0.25$ and -29.31 % for $\mu_{pp} = 0.40$. Interestingly, all the investigated combinations accurately predicted the friction on the aluminium surface (|error| ≤ 8.00 %); however, failed significantly for the sandpaper surface (-20.69 % ≤ error ≤ -29.31 %). This could be due to the single contact between the particles and the plate and as a result, a negligible increase in the frictional force with an increase in the friction coefficient will be present. The results further showed that the outflow velocity V_a was accurately predicted on both surfaces for all combinations (|error| ≤ 5.67 %). This was surprising since the ball particles failed to predict the after-impact velocity on a vertical plate in Section 8.2.5.2.

Table 30: Predicted reaction forces and after-impact velocity on an angled plate using the ball particles with various combinations of μ_{pp} and $\mu_{r\,pp}$ ($V_b = 3$ m/s and $\dot{m} = 8$ kg/s).

			Reaction forces and after-impact velocity					
μ_{pw}	μ_{pp}	$\mu_{r\,pp}$	**R_n [N]**	**Compared to* 3-clump model**	**Compared to** measurements**	**R_s [N]**	**Compared to* 3-clump model**	**Compared to** measurements**
0.25	0.20	0.125	6.56	-9.27 %	-21.53 %	1.60	-9.09 %	-24.53 %
	0.25	0.50	8.99	24.34 %	7.54 %	2.18	23.86%	2.83 %
	0.30	0.50	9.70	34.16 %	16.03 %	2.34	32.95 %	10.38 %
	0.40	0.125	8.41	16.32 %	0.60 %	1.96	11.36 %	-7.55 %
	0.40	0.50	10.28	42.19 %	22.97 %	2.45	39.20 %	15.57 %
0.80	0.20	0.125	7.05	-16.96 %	-24.27 %	3.24	-35.33 %	-39.55 %
	0.25	0.50	9.91	16.73 %	6.44 %	4.58	-8.58 %	-14.55 %
	0.30	0.50	10.56	24.38 %	13.43 %	4.72	-5.79 %	-11.94 %
	0.40	0.125	9.11	7.30 %	-2.15 %	3.77	-24.75 %	-29.66 %
	0.40	0.50	11.15	31.33 %	19.76 %	4.83	-3.59 %	-9.89 %
			R_n/R_s [-]	**Compared to* 3-clump model**	**Compared to** measurements**	**V_a [m/s]**	**Compared to* 3-clump model**	**Compared to** measurements**
0.25	0.20	0.125	0.24	-4.00 %	-4.00 %	3.09	0.46 %	-0.58 %
	0.25	0.50	0.24	-4.00 %	-4.00 %	3.07	-0.32 %	-1.22 %
	0.30	0.50	0.24	-4.00 %	-4.00 %	3.05	-0.85 %	-1.87 %
	0.40	0.125	0.23	-8.00 %	-8.00 %	3.07	-0.20 %	-1.22 %
	0.40	0.50	0.24	-4.00 %	-4.00 %	3.06	-0.52 %	-1.54 %
0.80	0.20	0.125	0.46	-22.03 %	-20.69 %	2.93	6.55 %	-2.33 %
	0.25	0.50	0.46	-22.03 %	-20.69 %	2.85	3.64 %	-5.00 %
	0.30	0.50	0.45	-23.73 %	-22.41 %	2.85	3.64 %	-5.00 %
	0.40	0.125	0.41	-30.51 %	-29.31 %	2.89	5.09 %	-3.67 %
	0.40	0.50	0.43	-27.11 %	-25.86 %	2.83	2.91 %	-5.67 %

The percentage error was calculated by comparing the ball particle results to the results of the *3-clump particles and **experimental tests.